

Master's thesis

Modelling of Electrical Circuits in Submerged Arc Furnaces

Ida Monsen

Computational Science
60 ECTS study points

Department of Physics
Faculty of Mathematics and Natural Sciences

Spring 2025



Ida Monsen

Modelling of Electrical Circuits in Submerged Arc Furnaces

Supervisors:
Vetle Kjær Risinggård
Morten Hjorth-Jensen

Abstract

Most submerged arc smelting furnaces for ferroalloys consist of three grid connections and three transformers, sending high currents into three electrodes standing in a metal bath. Optimal electrical conditions are integral both for energy efficiency and product quality, but due to high temperatures and magnetic fields direct observation of the system is practically impossible. Modelling of various kinds is therefore a frequently used tool to further our understanding of and carry out simulations on the system.

In this thesis we develop linear equivalent circuit models of such a three-phase system that includes both the grid connection, the primary side of the transformers, and the furnace itself, the secondary side. In addition to modelling electrical conditions inside the furnace itself, this allows us to study how changes on the primary side impact the secondary side and vice versa. We implement a numerical solver for circuit equations using the framework of graph theory.

Using different symmetry assumptions we first solve separate circuit models of the primary and secondary sides analytically. We prove that unbalanced electrodes or capacitors do not lead to circulating currents, but unbalanced transformers do. This is verified numerically with a circuit model of the entire system.

We also define a circuit model for low-voltage compensation, where the capacitors for power factor correction are placed on the secondary side. Using low-voltage compensation we can get a higher power factor in the transformers as compared to with high-voltage compensation, thus getting the same active power delivered to the electrodes with a lower current through the secondary side of the transformers. Estimates of currents, voltages and power factor in different parts of the furnace and supply are presented.

To run time simulations with our circuit model, we integrate it with a previously developed furnace metamodel. We then simulate a control algorithm and its effect on the primary side, and find that the metamodel has an interaction effect between the electrode resistances. Correcting the electrode voltage measurement by use of symmetrical components is a suggested route forward.

Our circuit model of the full system is compared to measurements from a ferromanganese furnace in production. We find the model to agree well with measurements, being able to reproduce both the trends and absolute values of measurements fairly accurately. After scaling all values to between 0 and 1, the r.m.s. error of the circuit model compared to measurement data is of the order 10^{-3} to 10^{-4} . This shows that a simplified linear circuit model is able to capture most of the electrical behaviour of the furnace and supply system.

Samandrag

Acknowledgements

Acknowledgements

Contents

1	Introduction	1
1.1	Smelting furnaces	1
1.1.1	Manganese.	1
1.1.2	Submerged arc furnaces.	2
1.1.3	Furnace models	3
1.2	Thesis outline	3
2	Circuit theory	5
2.1	Transformers	8
2.2	Three-phase systems	9
2.2.1	Symmetrical components	9
2.3	Power factor correction	11
2.3.1	High-voltage compensation.	11
3	Graph theory	13
3.1	Definitions	13
3.2	Results for digraphs.	15
3.3	Finding a basis of $\ker(\mathcal{A})$	15
3.4	Solving circuit problems with graph theory	16
3.4.1	General case	16
3.4.2	Harmonic problems.	18
4	Furnace power supply	21
4.1	Circuit models	21
4.1.1	Secondary side	21
4.1.2	Primary side	22
4.1.3	Full equivalent circuit	22
4.1.4	Low-voltage compensation.	22
4.2	Defining circulating currents.	24
4.2.1	Secondary side	24
4.2.2	Primary side	25
4.3	A furnace metamodel	25
4.4	Electrical furnace control	26
4.5	Measurement strategies	27
4.5.1	Rogowski coils	27
4.5.2	The Böckman method.	27

5	Analytical solutions	29
5.1	Secondary side	29
5.1.1	Balanced circuit	30
5.1.2	Unbalanced electrodes	31
5.1.3	Unbalanced transformers	31
5.2	Primary side	32
5.2.1	Balanced circuit	33
5.2.2	Unbalanced capacitors	35
5.2.3	Unbalanced transformers	35
5.2.4	Power factor and capacitance	35
6	Implementation	39
6.1	Validation	40
7	Full system	43
7.1	Estimating transformer parameters	43
7.2	Comparison with separate models	45
7.3	Discussion	48
8	Low-voltage compensation	51
8.1	Discussion	54
9	Metamodel simulations	57
9.1	Interaction effect	57
9.2	Discussion	59
9.2.1	Interaction effect	60
10	Measurement comparison	63
10.1	Data preprocessing	63
10.1.1	Phase and amplitude estimation	63
10.1.2	Scaling	64
10.1.3	Choosing which measurements to use	64
10.2	Data exploration	64
10.3	Comparison	66
10.4	Discussion	70
10.4.1	Measurements	70
10.4.2	Comparison with circuit model	71
11	Conclusion	73
11.1	Summary	73
11.2	Future work	74
A	Circuit diagram symbols	75
B	Analytical current solutions	77
C	Fast Fourier transform	79

List of Figures

1.1	Drawing of a submerged arc smelting furnace, courtesy of Hannesson [4].	2
2.1	Circuit diagram of ideal an transformer..	9
2.2	Circuit diagram of a non-ideal transformer.	9
2.3	Circuit diagram of a non-ideal transformer approximation suitable for medium-sized and large transformers.	9
2.4	The two types of three-phase circuit connections.	10
4.1	Circuit diagrams of (a) the secondary side equivalent circuit and (b) the primary side equivalent circuit.	22
4.2	Circuit diagram of the full system, with the primary and secondary sides connected through transformers.	23
4.3	Circuit diagram of the full system with low-voltage compensation.	24
4.4	Schematic drawing of a Rogowski coil setup, from Wikimedia Commons [39]. The left part of the figure shows the Rogowski coil itself wrapped around the conducting line. The circuit to the right is the so-called integrator circuit.	27
4.5	Schematic drawing of the Böckman method, courtesy of Böckman [41].	28
5.1	Directed graphs of (a) the secondary side circuit and (b) the primary side circuit.	30
6.1	Primary side circulating currents for the case where one transformer has different resistance and reactance from the others.	42
6.2	Secondary side circulating currents for the case where one voltage source has different resistance from the others.	42
7.1	Directed graph of the full system.	44
7.2	Time series of voltage drops covering one period, calculated both with the circuit model <i>HVC</i> and with the circuit model <i>Primary</i> . The values are from top to bottom grid supply, capacitors, conductors, primary side transformers, secondary side transformers, and electrodes.	46
7.3	Circulating currents in primary and secondary side deltas when one transformer has different impedance from the others, calculated in different ways.	47
7.4	The power factor seen from the grid as a function of capacitance, calculated both with the circuit model <i>HVC</i> and the circuit model <i>Primary</i>	48
8.1	Directed graph of the full system circuit with low-voltage compensation.	52
8.2	Behaviour of some power factors, powers, currents and voltages in different parts of the system as a function of capacitance, for both low-voltage compensation and high-voltage compensation.	53

List of Figures

8.3	LVC to HVC ratio of optimal capacitance, capacitor current and capacitor voltage as a function of transformer windings ratio. The axes are logarithmic.	55
9.1	Clamp positions and electrode resistances from a ferromanganese metamodel simulation of operation with resistance control. The resistance dead-zone is $0.75 \text{ m}\Omega \pm 0.05 \text{ m}\Omega$ and the clamp positions are limited to between 0 and 1. <i>hide dead-zone values?</i>	58
9.2	An example of the interaction effect on resistance. We move two electrodes in sync and keep the third electrode stationary. If there was no interaction the resistance of the stationary electrode would be constant.	59
9.3	The zero sequence component v_0 of the electrode voltages from the interaction example plotted in the complex plane. The dot in the origin corresponds to the balanced case where $v_0 = 0$, and v_0 moves further away from the origin as the two moving electrodes get further away from the stationary electrode. The phase angles of the three electrode voltages are marked with red lines.	60
10.1	Time series of two periods of high-resolution measurement data for current in electrode 1, voltage over electrode 1, and voltage over transformer A.	65
10.2	Phase differences between the three electrode currents. The phases are extracted from high-resolution measurement data.	65
10.3	Imbalance in high-resolution measurement data, calculated from symmetrical components.	66
10.4	The symmetrical components of high-resolution electrode voltage measurements. The y axis is linear and starts at 0.	67
10.5	The zero sequence component v_0 of electrode voltage from 20 minutes of high-resolution measurement data plotted in the complex plane. The phase angles of the three electrode voltages are marked with red lines. The radial axis is linear.	67
10.6	Comparison of r.m.s. values from process data and r.m.s. values calculated from high-resolution measurement data. Currents and voltages are scaled to lie between 0 and 1, and the y axis of the power factor plots is linear.	68
10.7	Comparison of r.m.s. values from the full equivalent circuit model <i>HVC</i> and r.m.s. values from high-resolution measurement data. Currents and voltages are scaled to lie between 0 and 1, and the y axis of the power factor plots is linear.	69

List of Tables

6.1	The parameter values used for numerical solutions to the primary side circuit.	41
6.2	The parameter values used for numerical solutions to the secondary side circuit.	41
7.1	The parameter values used for numerical solutions to the full system.	45
8.1	Optimal capacitance and other circuit values at this optimal capacitance, for both high-voltage and low-voltage compensation. All transformer values are given for the secondary side.	52
8.2	Slope and intercept of a first-order linear regression done on logarithmic data of transformer winding ratio versus ratio of LVC values to HVC values for several quantities..	54
9.1	The slope of the lines in Fig. 9.2, where we move two electrodes in sync and observe the change in resistance for all three electrodes.	59
10.1	R.m.s. error of values calculated with the full circuit model compared to high-resolution measurement data. All currents and voltages have been scaled to lie between 0 and 1 before calculating the error.	70

List of Tables

Chapter 1

Introduction

1.1 Smelting furnaces

Smelting is a process used to extract desired metals from some raw material. Something about blast furnaces and smelting furnaces very generally.

This study will use methods that are applicable to ferroalloy submerged arc furnaces in general. However, the specific values we will use come from a ferromanganese furnace. As we therefore implicitly consider a ferromanganese furnace, the following will be an introduction to such furnaces. We will also focus on the electrical part of the process. For a more detailed look at the metallurgy of furnaces, see for example [1]–[3]. Changing electrical parameters have an effect on the time scale of seconds, whereas changing metallurgical parameters have an effect on the time scale of many hours. This justifies looking at electrical and metallurgical conditions separately [1].

1.1.1 Manganese

Manganese (Mn) is a metal and the 25th element of the periodic table, commonly used in steel alloys. It is mostly added in the form of alloys such as ferromanganese or silicomanganese [1]. We will sometimes write FeMn for ferromanganese and SiMn for silicomanganese, but note that these are not chemical formulae. As of 1992, 90 – 95 % of the manganese produced was used in steel [1] and in 2010 the world production of ferromanganese was $5.7 \cdot 10^9$ kg [3].

The natural source of manganese is deposits with a high concentration of minerals containing manganese, often various oxides. The goal of the smelting process is, simply put, to remove the oxygen by a reduction reaction and be left with manganese metal [1]. As manganese deposits typically contain iron oxides as well, and iron oxide reduces more easily than manganese oxides, the final product will be an alloy of manganese and iron, ferromanganese. Other elements may be contained in smaller amounts [1].

The desired chemical reactions are endothermic, meaning that they require energy input, usually in the form of heat. This is achieved by sending electric currents through the electrodes and coke bed, causing heat dissipation due to the elements' resistance [1].

Most ferroalloys, including manganese alloys, are today produced in three-phase electric smelting furnaces, with three electrodes and a circular design, that operates between 20 and 45 MW [1], [3]. The production typically consumes electricity of about 3000 to 3500 kWh per tonne ferromanganese [3].

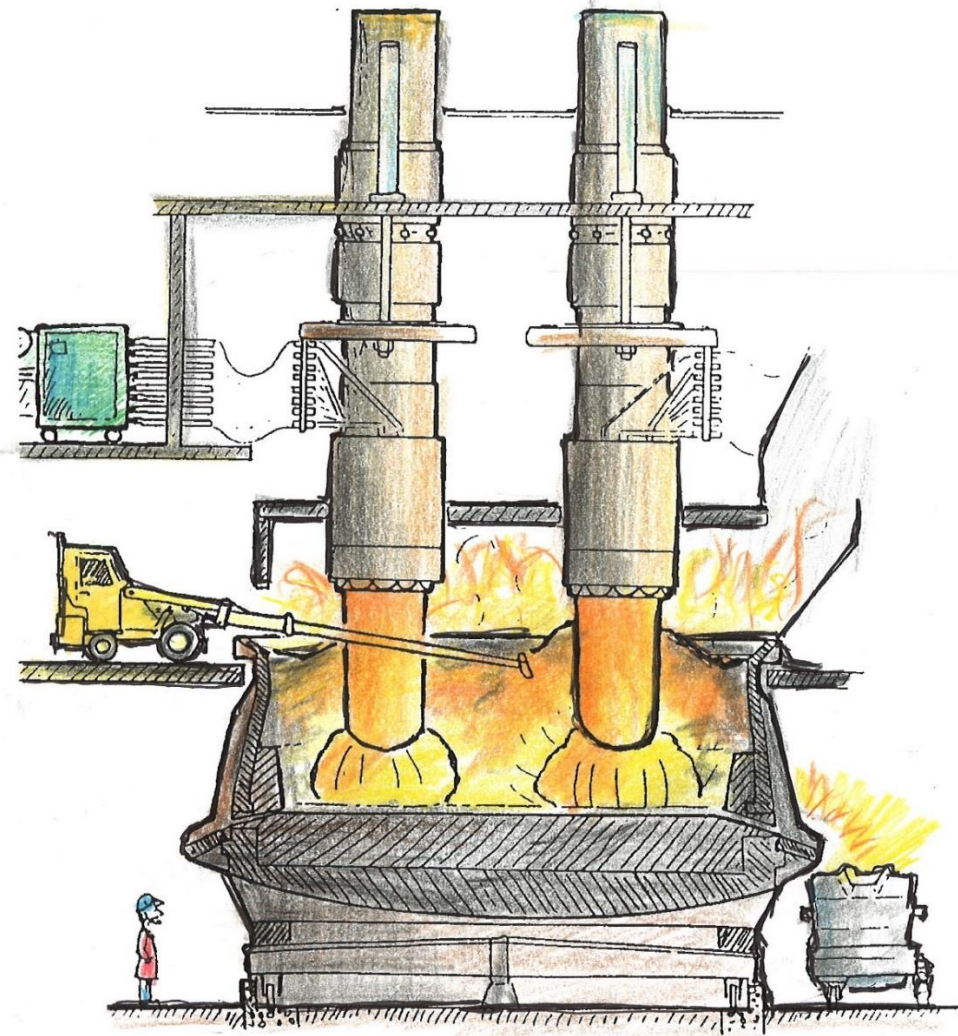


Figure 1.1: Drawing of a submerged arc smelting furnace, courtesy of Hannesson [4].

1.1.2 Submerged arc furnaces

An electric arc smelting furnace consists of a steel shell, carbon electrodes fastened to clamps so that their position can be adjusted, feed chutes for adding raw material and tap holes to extract the metal and slag. When high currents are sent into the electrodes, it creates electric arcs from the electrode tips to the furnace contents. The heat dissipation in the arcs and due to resistance in the materials create a high enough temperature for the reactions to take place [3]. The three electrodes are fastened in holders with a slip system, so that more of the electrode can be fed into the furnace as the tip is consumed in reactions [1], [3].

In a submerged arc furnace the electrodes are immersed in the furnace contents such that there are no visible arcs. A typical smelting furnace is circular, with three electrodes arranged in an equilateral triangle and receiving three-phase AC current from three single-phase transformers or one three-phase transformer, but other configurations are possible [3]. Figure 1.1 shown a drawing of a submerged arc smelting furnace, drawn by Hannesson [4]. The drawing depicts a ferrosilicon furnace, not a ferromanganese one, but the general construction is the same.

The resistance in the furnace depends on factors like temperature, material composition, and furnace geometry such as electrode position and electrode diameter. These factors will vary under operation, and therefore so will the resistance. Electrode position is the only factor that can be easily controlled, and is therefore used to adjust the resistance in operation control [1]. Proper furnace control gives the benefit of both better product quality and more efficient electricity usage. Optimising electrical conditions is in general important, and there are many considerations to take into account [5].

The electrical supply system consists of grid connections and capacitors on the primary side, transformers, and bus bars and flexible conductors on the secondary side, connecting the transformers to the electrodes [6].

1.1.3 Furnace models

Much work has already been done on modelling electrical conditions of submerged arc furnaces, with various approaches. We can divide the models roughly into four types: (1) empirical models, (2) analytical models based on models of charge conductivity, (3) physics-based mathematical models describing some or all of electrical, magnetic and thermal conditions, chemical reactions, and heat and mass flow, and lastly (4) equivalent circuit models [2].

Physics-based models are common, with many different variations, see for example [7]–[18]. Some of these models are two-dimensional, some are three-dimensional, they might consider only one electrode or all three electrodes at once, use alternating current or simplify to direct current. Physics-based models are often good at studying details like current paths or heat distribution in specific parts of the furnace, but they are computationally costly.

Equivalent circuit models of submerged arc furnaces have been studied by for example [2], [6], [19], but circuit models are more commonly used for open arc furnaces [2]. Circuit models are computationally lightweight compared to physics-based models, but require that we assume current paths as part of the model design and strictly limit the analyses to electrical conditions.

In this thesis we will develop and study equivalent circuit models, but unlike the other circuit models we will include the primary side supply system as well. Thus, the goal of this thesis is not to study the details of what happens inside the furnace, but rather to develop and study a model that can give an overview over the electrical conditions and behaviours of the entire system, both the power supply and the furnace itself. We want a model that is as simple as possible, yet retains the most important aspects of the supply and furnace system.

1.2 Thesis outline

As described above, efforts have been made to analyse equivalent circuits of submerged-arc furnaces before, but they have focused on models of the secondary side only. With the help of numerics this thesis will develop and study a model of the secondary and primary sides together. This gives us the option to study not only what goes on electrically inside the furnace, but how that effects electrical conditions on the primary side. We will assume that the circuit is linear and that there are no higher harmonics present, although the arc is non-linear and therefore generate higher harmonics [20]. We also limit ourselves to stationary models, although furnaces in truth are dynamic systems.

Thus, a significant part of the thesis will be evaluating how well our simplified system is able to represent the true system.

Chapter 2 presents the circuit theory needed to understand the rest of this thesis, and here we go through all relevant circuit components and electrical concepts. We particularly look at transformers, three-phase systems, and power factor correction. Chapter 3 starts with a rigorous presentation of relevant graph theory, and goes on to detail how we use graph theory to solve circuit problems. We start with a general solution strategy and then explain how the problem simplifies when we restrict ourselves to harmonic problems. In Chapter 4 we look more closely at the furnace and power supply system. We develop circuit models for the furnace, the supply system and the whole system combined and present a previously developed furnace metamodel that we will later make use of in simulations. The chapter ends with a presentation of electrical control strategies for submerged arc furnaces and how to make measurements of a furnace during operation.

Chapter 5 presents analytical solutions for the primary and secondary side circuit models, as they are small enough that we do not need numerics. We study analytically the effect of introducing unbalanced elements into the circuits, and for the primary side the connection between capacitance and the grid power factor. In Chapter 6 we implement a numerical solver based on the graph solution method and verify it by comparing the analytical and numerical solutions of the primary and secondary side circuits. Chapter 7 goes on to solve the circuit model of the whole system and compare it with the solution of the two separate circuit models.

In Chapter 8 we study a circuit model of a furnace with low-voltage compensation, in contrast to the standard high-voltage compensation. We compare and contrast the two ways of doing power factor correction, studying the effects in different parts of the furnace and supply system. Chapter 9 uses the metamodel to implement and run simulations of a ferromanganese furnace operating with a resistance controller. We present an example showing that there is an interaction effect in the control simulation. In Chapter 10 we look at measurement data, taken from a ferromanganese furnace in operation. We process and inspect the data itself, before comparing the measurement data to our circuit model. And finally, we conclude in Chapter 11.

Chapter 2

Circuit theory

- Maxwell's equations?

We start by summarising the fundamental circuit theory needed in this thesis. Kirchhoff's laws describe conditions on the currents and voltages in circuits due to conservation of charge and energy. Kirchhoff's current law states that

$$\sum_i I_i = 0 \quad (2.1)$$

for the currents I_i going into any circuit junction and Kirchhoff's voltage law states that

$$\sum_i V_i = 0 \quad (2.2)$$

for the potential differences V_i over any closed loop in a circuit [21, p. 10].

We divide power supply into direct current (DC) and alternating current (AC), where AC is the most common in both domestic and industrial applications. An AC signal typically varies as a sine wave, such that the instantaneous current i can be written as

$$i = I_p \sin(\omega t + \phi),$$

where I_p is the peak current or amplitude of the signal, ω is the angular frequency, t is the time in seconds and ϕ is a phase shift. It is often useful to use complex notation, with the complex current written as

$$I = I_p e^{j(\omega t + \phi - \pi/2)},$$

where j is the imaginary unit. This complex notation is sometimes called a phasor. The real current is the real part of the above expression,

$$i = \operatorname{Re} \left(I_p e^{j(\omega t + \phi - \pi/2)} \right).$$

We will assume all signals to be AC sinusoidal signals unless otherwise specified and use the notation I , I_p and i for complex current, peak current and instantaneous current, respectively. The same convention will be used for other sinusoidal signals, such as voltage.

The relevant circuit components are resistors, inductors and capacitors, with characteristic relationships between the instantaneous current i through and voltage v over the component. A resistor represent a non-perfect conducting material. For a resistor

$$v = Ri, \quad (2.3)$$

where R is the resistance measured in ohm (Ω). In a resistor the current and voltage are in phase with each other.

An inductor represents an element where changing current induces a voltage counteracting the change. This happens for example in a coiled-up wire. For an inductor

$$v = L \frac{di}{dt}, \quad (2.4)$$

where L is the inductance measured in henry (H). In an inductor with a sinusoidal current, the voltage is ahead of the current by $\pi/2$ radians, and an inductive element will in general have a voltage leading the current.

And finally, a capacitor is an element that can store and release electric charge. Two parallel conducting plates with an insulating layer between them acts as a capacitor. For a capacitor,

$$v = \frac{1}{C} \int idt, \quad (2.5)$$

where C is the capacitance measured in farad (F). In a conductor with a sinusoidal current, the voltage is behind the current by $\pi/2$ radians, and the voltage will in general lag the current in a capacitive element.

We will also use magnetically coupled components, that is components with mutual inductance. The relationship between instantaneous current i_1 in component 1 and voltage v_2 in component 2 is given by

$$v_2 = M \frac{di_1}{dt}, \quad (2.6)$$

and the vice versa. M is called mutual inductance and is, as for self-inductance L , measured in henry (H) [21]. The mutual inductance of two perfectly magnetically coupled elements is given by

$$M = \sqrt{L_1 L_2}, \quad (2.7)$$

where L_1 is the inductance in one element and L_2 the inductance of the other [22].

For a resistor, the resistance R equals the peak to peak ratio of current to voltage since the signals are in phase with each other. The same peak to peak ratio is called reactance X for inductors and capacitors [21]. When the signals are sinusoidal, we find that the reactance of an inductor is

$$X_L = \omega L \quad (2.8)$$

and that the reactance of a capacitor is

$$X_C = \frac{1}{\omega C}. \quad (2.9)$$

Notably, the reactance is dependent on angular frequency ω as well as the inductance or capacitance.

The impedance Z of a component describes the instantaneous relationship between the voltage and current of that component,

$$Z = \frac{V}{I}, \quad (2.10)$$

where V and I are the complex voltage and current, respectively. Impedance is also a complex quantity, with magnitude equal to the resistance or reactance of a component

and angle corresponding to the phase shift between the current and voltage. In a resistor the current and voltage have the same phase, while in a capacitor the current leads the voltage by 90° and in an inductor the current lags the voltage by 90° . The impedances of a resistor, capacitor and inductor are thus given by

$$Z_R = R, \quad (2.11)$$

$$Z_C = -j \frac{1}{\omega C}, \quad (2.12)$$

$$Z_L = j\omega L, \quad (2.13)$$

respectively, where j is the imaginary unit [21]. An overview over the circuit symbols used in this thesis can be found in Appendix A.

The instantaneous power dissipation p in a component is equal to the product of instantaneous current i and instantaneous voltage v ,

$$p = vi. \quad (2.14)$$

Assuming the voltage and current to be sinusoidal with amplitudes V_p and I_p , and that the phase shift between them is ϕ radians, the average power dissipation is

$$P = \frac{1}{2}V_p I_p \cos \phi. \quad (2.15)$$

We call P active power and measure it in watt (W). Alternatively, we can express the power in terms of root mean square (r.m.s.) values. For a sinusoidal current $i = I_p \sin(\omega t + \phi)$, the root mean square current is

$$I_{\text{rms}} = \left(\frac{\omega}{2\pi} \int_0^{2\pi/\omega} I_p^2 \sin^2(\omega t + \phi) dt \right)^{\frac{1}{2}} = \frac{I_p}{\sqrt{2}},$$

and in the same way

$$V_{\text{rms}} = \frac{V_p}{\sqrt{2}}.$$

Thus, the average power dissipation can also be expressed as

$$P = VI \cos \phi, \quad (2.16)$$

where V and I are r.m.s. values. Reactive components store and return power to the circuit during each period of the signal, and this power is called reactive power Q . It is given by

$$Q = \frac{1}{2}V_p I_p \sin \phi = VI \sin \phi \quad (2.17)$$

for sinusoidal signals and is measured in volt ampere reactive (var) to distinguish it from active power. Note that the reactive power is positive for inductive elements, since the voltage leads the current and therefore ϕ is greater than zero, and negative for capacitive elements since the voltage lags the current. Lastly we have apparent power S , defined simply as

$$S = \frac{1}{2}V_p I_p = VI \quad (2.18)$$

and with units volt ampere (VA). Note that all three power units are technically the same, the different units are merely used to distinguish the different forms of power. The relationship between active, reactive and apparent power is

$$S = \sqrt{P^2 + Q^2}.$$

Total power is a complex quantity with

$$\text{total power} = P + iQ \quad (2.19)$$

For a component with impedance $Z = R + jX$, we can find the active power as

$$P = \frac{1}{2}V_p I_p \cos \phi = \frac{1}{2}I_p^2 |Z| \cos \phi = \frac{1}{2}I_p^2 R \quad (2.20)$$

and the reactive power as

$$Q = \frac{1}{2}V_p I_p \sin \phi = \frac{1}{2}I_p^2 |Z| \sin \phi = \frac{1}{2}I_p^2 X. \quad (2.21)$$

The ratio of active to apparent power is called power factor,

$$\text{power factor} = \frac{P}{S} = \cos \phi, \quad (2.22)$$

where ϕ as before is the phase angle between voltage and current.

2.1 Transformers

Transformers are used to change the magnitude of an AC current and voltage, increasing one and decreasing the other, in the ideal case by the same factor. They work by using mutual inductance between different coils wound around the same core with a different number of windings. An ideal transformer is shown in Fig. 2.1. The two inductive elements represent the two coiled wires, and the fact that they are magnetically coupled through the common core is represented by the parallel lines. We call the side where we apply a voltage for the primary side, and the side where a voltage is induced for the secondary side. If there are N_1 windings on the primary side and N_2 windings on the secondary side, the relationship between the primary side voltage V_1 and the secondary side voltage V_2 is

$$\frac{V_1}{V_2} = \frac{N_1}{N_2}. \quad (2.23)$$

If the secondary side is on load, such that a current I_2 is induced, the relationships between the currents will similarly be

$$\frac{I_1}{I_2} = \frac{N_2}{N_1}. \quad (2.24)$$

We see that if the voltage is increased by a given factor, the current is reduced by the same factor.

In a real transformer there are several other effects that we need to take into account, and Eqs. (2.23) and (2.24) do not hold. These effects are magnetizing current and core loss, winding resistance, and magnetic leakage flux [22]. Magnetizing current and core loss can be represented as an inductor and a resistor, respectively, connected in parallel on one side of the ideal transformer. Winding resistance and magnetic leakage flux can

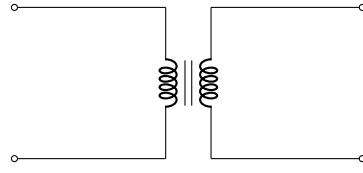


Figure 2.1: Circuit diagram of an ideal transformer.

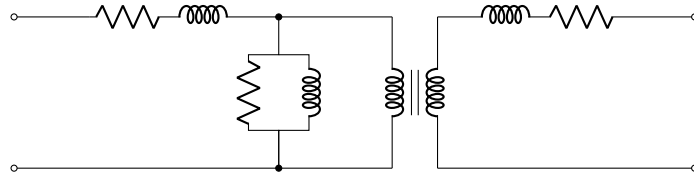


Figure 2.2: Circuit diagram of a non-ideal transformer.

be represented as a resistor and an inductor connected in series on both sides. Figure 2.2 shows an equivalent circuit of such a transformer, redrawn after Hurley [22].

The values of the components making the transformer non-ideal will depend on the specific transformer, and the importance of each will also vary. Neglecting magnetizing current and core loss is usually a good approximation if the transformer is medium-sized or large [23]. We can make an equivalent circuit of this approximation where the winding resistances and magnetic leakage fluxes of both sides are represented by a single resistor and inductor located on either the primary or secondary side. Such a circuit is depicted in Fig. 2.3.

2.2 Three-phase systems

In industrial applications, power is usually distributed through a three-phase system. As the name suggests, this means using three sources at once, each with a different phase. Three-phase circuits can be connected in either Y (wye) or Δ (delta) connections, as shown in Figs. 2.4a and 2.4b, respectively [24]. The Y connection can also be called a star connection. If the phases of the three supplies differ by $2\pi/3$ and the loads are equal, we call the system balanced. These conditions can never be met exactly, so all real systems are unbalanced to some degree. Using a three-phase system can deliver the same amount of power as three separate single-phase systems, but with only half the number of conducting lines [24].

2.2.1 Symmetrical components

Symmetrical components are sometimes used to simplify calculations on three-phase systems. It is a decomposition of the three possibly unbalanced phasors into three sets

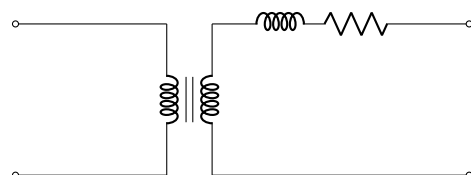


Figure 2.3: Circuit diagram of a non-ideal transformer approximation suitable for medium-sized and large transformers.

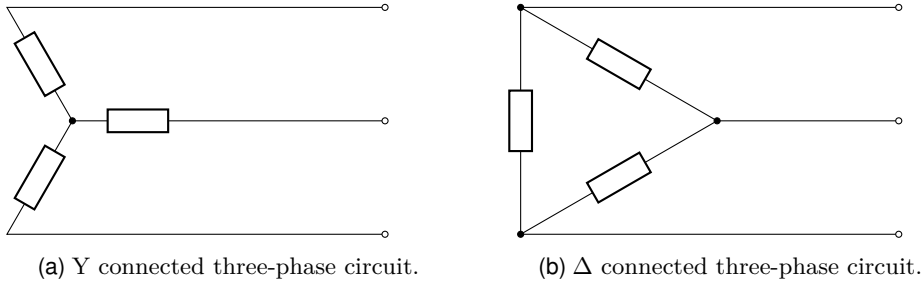


Figure 2.4: The two types of three-phase circuit connections.

of three phasors, where two of the sets are balanced and the third set have a common phase [25].

Let the three voltage phasors in a three-phase system be represented by the complex numbers V_a , V_b and V_c and let $\alpha = e^{i2\pi/3}$. The voltage phasors can then be decomposed as

$$\begin{bmatrix} V_a \\ V_b \\ V_c \end{bmatrix} = \begin{bmatrix} V_0 \\ V_0 \\ V_0 \end{bmatrix} + \begin{bmatrix} V_1 \\ V_1\alpha^2 \\ V_1\alpha \end{bmatrix} + \begin{bmatrix} V_2 \\ V_2\alpha \\ V_2\alpha^2 \end{bmatrix}, \quad (2.25)$$

where V_0 is the common phasor (zero sequence), V_1 , $V_1\alpha^2$, $V_1\alpha$ is the set with positive rotation (positive sequence) and V_2 , $V_2\alpha$, $V_2\alpha^2$ is the set with negative rotation (negative sequence) [25]. Equation (2.25) can be written more compactly as

$$V_{abc} = AV_{012}, \quad (2.26)$$

where

$$A = \begin{bmatrix} 1 & 1 & 1 \\ 1 & \alpha^2 & \alpha \\ 1 & \alpha & \alpha^2 \end{bmatrix}, \quad V_{abc} = \begin{bmatrix} V_a \\ V_b \\ V_c \end{bmatrix}, \quad V_{012} = \begin{bmatrix} V_0 \\ V_1 \\ V_2 \end{bmatrix}.$$

We find the vector V_{012} as

$$V_{012} = A^{-1}V_{abc}, \quad (2.27)$$

where

$$A^{-1} = \frac{1}{3} \begin{bmatrix} 1 & 1 & 1 \\ 1 & \alpha & \alpha^2 \\ 1 & \alpha^2 & \alpha \end{bmatrix} \quad (2.28)$$

is well defined. The exact same decomposition can be done with three-phase current.

The negative sequence to positive sequence ratio

$$\frac{V_2}{V_1} \quad (2.29)$$

is the IEC (International Electrotechnical Commission) standard of voltage imbalance [26], assuming V_{abc} to be ordered so that it has a positive rotation, and we will use the same ratio as a measure of current imbalance. In a perfectly balanced system, $V_0 = 0$ and $V_2 = 0$, in which case the ratio in Eq. (2.29) is zero. The further we are from zero, the more unbalanced the system is. If we have the opposite rotation of what we thought, Eq. (2.29) gives a number greater than one.

2.3 Power factor correction

Power factor correction is the procedure of installing reactive elements in a circuit in order to bring the power factor (2.22) closer to one [21]. This is useful because it allows for more efficient power use, by producing as much as possible active power, and because power companies charge industrial consumers for a poor power factor [21]. Power factor correction is thus both efficient and economically beneficial.

One can use capacitors for this purpose if the element causing the reduced power factor is inductive and vice versa, since the reactive effects of a capacitive and inductive element work towards cancelling each other out. Finding the element needed to bring the power factor to one is therefore a matter of calculating the reactive power of the circuit and adding an element which will have the same absolute reactive power but with opposite sign.

2.3.1 High-voltage compensation

Power factor correction is a standard procedure in submerged arc furnaces, especially since the power factor decreases with increasing furnace size [27]. In submerged arc furnaces the tradition is to place three capacitors in parallel on the primary side. This arrangement does not alter the power factor of the furnace, but can bring the power factor as seen from the grid closer to one [27]. We call this method high-voltage compensation (HVC) since the primary side is the high voltage side. Meintjes wrote in 1974 that capacitors “can theoretically be located on the secondary side [...], but the author knows of no practical application of this arrangement” [27], and the situation is largely the same today. There are however some more recent attempts at placing the capacitors on the secondary side, which we will treat later on.

Chapter 2. Circuit theory

Chapter 3

Graph theory

We will use the framework of graph theory when solving linear circuit problems, specifically for finding currents and voltages in all parts of a circuit when we know the source voltages, the source currents, and the impedances of all components. We will first go through the needed definitions and results from graph theory, and then go on to explain how we use this framework to set up and solve matrix equations in a structured way.

The solution method we use is found in a book by Bermúdez [28], but as will become apparent the method as presented there needs to be generalized. We therefore need a more rigorous graph theory framework. In an attempt to provide the necessary rigour without delving too deep, we below present graph theory definitions that are slightly adapted to our needs. This is all in the pursuit of being precise with the language and requirements for our solution method.

3.1 Definitions

There are slight differences in naming conventions and definitions between texts on graph theory, although the big picture is the same. We here provide definitions as given by Yadav [29] unless otherwise stated.

A simple graph \mathfrak{G} , from now on only called a graph, is a pair of finite sets (V, A) where $A \subseteq V \times V$. Or in other words, a graph consists of the elements in V , called nodes, and the elements in A , which are pairs of elements from V , called edges. The edges are denoted $\{a, b\}$, where $a, b \in V$. As for any set, the order of the elements a and b do not matter.

In a simple directed graph, or digraph, edges additionally have a specified direction or orientation. They are sometimes called arcs, but we will stick to the name edges. Let $r = (a, b) \in A$ be an edge of \mathfrak{G} . Then a is the tail and b is the head of r . Note that for a digraph, $(a, b) \neq (b, a)$ since the ordering matters. We will mostly be working with digraphs, but will give definitions for both graphs without a direction and for digraphs.

A path is a sequence of edges r_1, r_2, \dots, r_m for which there exists a sequence v_1, v_2, \dots, v_{m+1} of distinct nodes such that $r_i = \{v_i, v_{i+1}\} \forall i \in \{1, \dots, m\}$. If we do not require the sequence of nodes v_1, v_2, \dots, v_{m+1} to be distinct, we instead call the sequence of edges a trail. Two nodes a and b are connected if there exists a path between them or if $a = b$.

A directed path has the same definition, except that the sequence of edges r_1, r_2, \dots, r_m has a direction, that is $r_i = (v_i, v_{i+1})$. And similarly, if we do not require the sequence of nodes v_1, v_2, \dots, v_{m+1} to be distinct, we get a directed trail. There are

several concepts or degrees of connectivity for digraphs, but for our purposes it is enough to know whether the nodes of the underlying non-directed graph are connected. We will therefore use the non-directed definitions of connectivity also for directed graphs.

We can partition the nodes of a graph into groups in such a way that all nodes within each group are connected, and no two nodes in different groups are connected. Each such group is called a connected component. It can be shown that connectivity is an equivalence relation with connected components as its equivalence class. A graph \mathfrak{G} is called connected if it only has one connected component, or equivalently if all pairs of nodes in the graph are connected. We will use this same definition of connected components for digraphs.

Consider the graph $\mathfrak{G} = (V, A)$. A graph $\mathfrak{S} = (V', A')$ is a subgraph of \mathfrak{G} if and only if $V' \subseteq V$, $A' \subseteq A$ and $A' \subseteq V' \times V'$. An equivalent definition applies to directed graphs.

Given a graph \mathfrak{G} with a trail r_1, r_2, \dots, r_n and a corresponding sequence of nodes $v_1, v_2, \dots, v_n, v_1$, where v_1 is the only repeating node, meaning that this trail starts and ends at the same node. Then the subgraph \mathfrak{S} induced by this trail is called a cycle of \mathfrak{G} . If the graph and trail are directed, the resulting subgraph is a directed cycle. Note that a digraph may have no directed cycles, but the underlying non-directed graph can still have one or more cycles.

A tree is a connected graph \mathfrak{G} with no cycles. A graph where all its connected components are trees is called a forest. Thus, a forest with one connected component is also a tree. A spanning tree \mathfrak{T} is a subgraph of a connected graph \mathfrak{G} that contains all nodes of \mathfrak{G} and no cycles. That is, \mathfrak{T} is a tree that contains the same nodes as \mathfrak{G} . In extension of this concept, we also define a spanning forest \mathfrak{F} as a subgraph consisting of one spanning tree from each connected component.

For a directed tree and a directed spanning tree, we will differ from Yadav [29] and define it as a tree and spanning tree of the underlying non-directed graph, but with edges given the same orientation as the corresponding edges of the digraph. In accordance with Bermúdez [28], we will call the edges of a spanning tree \mathfrak{T} branches and the edges of the graph not belonging to the spanning tree we call bonds or chords. The bonds make up what we call the co-tree of the graph.

The incidence matrix, as defined in [28], is a way of representing a digraph as a matrix. Given a directed graph \mathfrak{G} with N nodes and E edges, the incidence matrix \mathcal{A} of \mathfrak{G} is an $N \times E$ matrix with elements

$$a_{ij} = \begin{cases} -1, & \text{if node } i \text{ is the tail node of } j \\ 1, & \text{if node } i \text{ is the head node of } j \\ 0, & \text{otherwise.} \end{cases} \quad (3.1)$$

Note that all N columns contain exactly one 1, one -1 and otherwise zeros, which means that the sum of all the rows is a zero vector and thus the rows are linearly dependent.

We will also need the concept of a cycle matrix as given by Bermúdez [28]. Given a digraph \mathfrak{G} with N nodes and E edges, where the underlying non-directed graph has L cycles. We give each cycle an arbitrary orientation, such that the edges belonging to the cycle may have the same or opposing direction to the cycle itself. The cycle matrix \mathcal{B} of size $E \times L$ is then defined as

$$b_{jl} = \begin{cases} -1, & \text{if edge } j \text{ belongs to cycle } l \text{ with opposing directions} \\ 1, & \text{if edge } j \text{ belongs to cycle } l \text{ with the same direction} \\ 0, & \text{otherwise.} \end{cases} \quad (3.2)$$

3.2 Results for digraphs

We here state results and theorems from graph theory that will be used further on.

For a digraph \mathfrak{G} with N nodes and M connected components it holds that

$$\text{rank}(\mathcal{A}) = N - M, \quad (3.3)$$

where \mathcal{A} is the incidence matrix of \mathfrak{G} [28]. Thus \mathcal{A} has exactly $N - M$ linearly independent columns.

If \mathfrak{G} is a connected digraph with N nodes and E edges, any selection of $N - 1$ rows from the incidence matrix are linearly independent if and only if they constitute the edges of a directed spanning tree \mathfrak{T} . The remaining $E - 1 + N$ rows correspond to the edges of its co-tree [28]. This result can be generalized to a graph with M connected components. Then, any selection of $N - M$ rows from the incidence matrix are linearly independent if and only if they constitute the edges of a directed spanning forest \mathfrak{F} .

For a connected digraph \mathfrak{G} with N nodes and E edges, we have

$$\text{rank}(\mathcal{B}) = E - N + 1$$

for the cycle matrix \mathcal{B} defined in Eq. (3.2) [28]. This result can be generalized to

$$\text{rank}(\mathcal{B}) = E - N + M \quad (3.4)$$

if the digraph instead has M connected components. Given a digraph \mathfrak{G} with N nodes, E edges and M connected components. It can be shown that

$$\mathcal{A}\mathcal{B} = 0 \quad (3.5)$$

for any incidence matrix and its corresponding cycle matrix. That means the columns of \mathcal{B} belong to the kernel of \mathcal{A} . From Eq. (3.3) and the fact that \mathcal{A} has E columns, the rank-nullity theorem from linear algebra tells us that the nullity of \mathcal{A} is $E - N + M$, which combined with Eq. (3.4) gives us

$$\text{nullity}(\mathcal{A}) = \text{rank}(\mathcal{B}). \quad (3.6)$$

Let \mathfrak{G} be a digraph with N nodes, E edges and M connected components, and \mathfrak{F} be a directed spanning forest. \mathfrak{F} has $N - M$ edges, and adding any one of the $E - N + M$ remaining edges will result in a cycle for the underlying non-directed graph. We call such a cycle a fundamental cycle. A submatrix of the cycle matrix as defined in Eq. (3.2) consisting of the columns corresponding to these fundamental cycles is called a matrix of fundamental cycles. These $E - N + M$ columns are linearly independent, and the matrix of fundamental cycles is therefore a basis for \mathcal{B} .

3.3 Finding a basis of $\ker(\mathcal{A})$

We will need a way to find a basis of the kernel of the incidence matrix \mathcal{A} when we use graph theory to solve circuit problems. We here describe a generalization of the solution method outlined by Bermúdez [28]. Bermúdez assumes the graph to be connected, but we will look at the general case.

Equations (3.5) and (3.6) together tell us that

$$\ker(\mathcal{A}) = \text{im}(\mathcal{B}),$$

and therefore a basis of \mathcal{B} will also be a basis of $\ker(\mathcal{A})$. This basis is a matrix of fundamental cycles, which we will denote as \mathcal{B}_F . It remains to find \mathcal{B}_F .

For the digraph \mathfrak{G} with a corresponding directed spanning forest \mathfrak{F} , we can without loss of generality assume that the edges of the graph are numbered such that the edges contained in the spanning forest come first. We define the reduced incidence matrix \mathcal{A}_R as any submatrix of \mathcal{A} with $N - M$ rows, where it holds that the M removed rows correspond to nodes from different trees of the forest. \mathcal{A}_R can then be decomposed as

$$\mathcal{A}_R = (\mathcal{A}_T, \mathcal{A}_C),$$

where \mathcal{A}_T is a $(N - M) \times (N - M)$ matrix with columns corresponding to the edges of the spanning forest, and \mathcal{A}_C is a $(N - M) \times (E - N + M)$ matrix with columns corresponding to the edges of the co-trees of the connected components. The matrix \mathcal{B}_F can be decomposed as

$$\mathcal{B}_F = \begin{bmatrix} \mathcal{B}_T \\ \mathcal{I} \end{bmatrix},$$

where \mathcal{I} is the identity matrix of size $(E - N + M) \times (E - N + M)$ and \mathcal{B}_T is a matrix of size $(N - M) \times (E - N + M)$. From Eq. (3.5) we get that

$$0 = \mathcal{A}_R \mathcal{B}_F = \mathcal{A}_T \mathcal{B}_T + \mathcal{A}_C,$$

and solving for \mathcal{B}_T ,

$$\mathcal{B}_T = -\mathcal{A}_T^{-1} \mathcal{A}_C. \quad (3.7)$$

The above expression is always well defined, since \mathcal{A}_T is a square matrix of full rank.

3.4 Solving circuit problems with graph theory

3.4.1 General case

The solution method presented here can be found in [28]. We start by modelling the circuit of interest as a directed graph where edges correspond to the electrical components and nodes correspond to the junctions between them. The direction of the edges are chosen arbitrarily. Let \mathcal{A} be the incidence matrix of this graph as defined in Eq. (3.1), of size $N \times E$ and with elements denoted by a_{ij} .

We denote the current along edge j at time t by $I_j(t)$, $j = 1, 2, \dots, E$ and let $\Psi_i(t)$, $i = 1, 2, \dots, N$ be an external current source entering at node i . Kirchhoff's current law (2.1) can then be rewritten as

$$\sum_{j=1}^E a_{ij} I_j(t) = -\Psi_i(t) \quad (3.8)$$

for each node $i = 1, 2, \dots, N$.

The voltage at a node i and time t is denoted by $V_i(t)$, $i = 1, 2, \dots, N$. We can then write the potential drop over the electrical components, which corresponds to the potential difference between the two nodes of an edge, in the following way: Let the nodes m_{1j} and m_{2j} be the head and tail, respectively, of edge j . If edge j is a resistor with resistance R_j , Eq. (2.3) can be rewritten as

$$V_{m_{1j}}(t) - V_{m_{2j}}(t) = R_j I_j(t). \quad (3.9)$$

If edge j is a capacitor with capacitance C_j , Eq. (2.5) can be rewritten as

$$V_{m_{1j}}(t) - V_{m_{2j}}(t) = \frac{1}{C_j} \left(Q_j(0) + \int_0^t I_j(s) ds \right), \quad (3.10)$$

where $Q_j(0)$ is the initial charge stored in the capacitor. If edge j is an inductor with inductance L_j , Eq. (2.4) can be rewritten as

$$V_{m_{1j}}(t) - V_{m_{2j}}(t) = L_j \frac{dI_j}{dt}(t). \quad (3.11)$$

If the edges l_1, l_2, \dots, l_S are magnetically coupled, we define the inductance matrix \mathcal{L}^S as the matrix with the self-inductance of the edges on the diagonal and the mutual inductance of the edges on the off-diagonals, that is

$$\begin{aligned} \ell_{ii} &= L_i, \\ \ell_{ij} &= M_{ij}. \end{aligned}$$

$M_{ij} = M_{ji}$ and the matrix \mathcal{L}^S is symmetric positive definite. This leads to the matrix equation

$$\mathcal{L}^S \frac{d\vec{I}_S}{dt}(t) = \Delta \vec{V}_S(t), \quad (3.12)$$

where

$$\begin{aligned} \vec{I}_S(t) &= (I_{l_1}(t), I_{l_2}(t), \dots, I_{l_S}(t))^T, \\ \Delta \vec{V}_S(t) &= \left(V_{m_{1l_1}}(t) - V_{m_{2l_1}}(t), \dots, V_{m_{1l_S}}(t) - V_{m_{2l_S}}(t) \right)^T, \end{aligned}$$

are the vectors with the currents through and voltages over the edges. If no edges are magnetically coupled, Eq. (3.12) reduces to Eq. (3.11). And lastly, if edge j is a power source with source voltage $E_j(t)$, we have the equation

$$V_{m_{1j}}(t) - V_{m_{2j}}(t) = r_j I_j(t) - E_j(t), \quad (3.13)$$

where r_j is the internal resistance of the power generator. We will often assume that $r_j = 0$.

We now define the vectors

$$\begin{aligned} \vec{I}(t) &= (I_1(t), I_2(t), \dots, I_E(t))^T, \\ \vec{V}(t) &= (V_1(t), V_2(t), \dots, V_N(t))^T, \\ \vec{E}(t) &= (E_1(t), E_2(t), \dots, E_E(t))^T, \\ \vec{\Psi}(t) &= (\Psi_1(t), \Psi_2(t), \dots, \Psi_N(t))^T, \end{aligned}$$

of currents, voltages, source voltages and source currents, respectively. Define also a linear operator \mathcal{D} working on the vector $\vec{I}(t)$ by

$$\mathcal{D}(\vec{I})_j(t) = \begin{cases} R_j I_j(t), & \text{if edge } j \text{ is a resistor} \\ \frac{1}{C_j} \left(Q_j(0) + \int_0^t I_j(s) ds \right), & \text{if edge } j \text{ is a capacitor} \\ L_j \frac{dI_j}{dt}(t), & \text{if edge } j \text{ is an inductor} \\ r_j I_j(t), & \text{if edge } j \text{ is a power source} \end{cases} \quad (3.14)$$

and

$$\mathcal{D}(\vec{I})_S(t) = \mathcal{L}^S \frac{d\vec{I}_S}{dt}(t), \quad (3.15)$$

where $\mathcal{D}(\vec{I})_S = (\mathcal{D}(\vec{I})_{l_1}, \mathcal{D}(\vec{I})_{l_2}, \dots, \mathcal{D}(\vec{I})_{l_S})^T$. The circuit problem where the input currents $\vec{\Psi}(t)$ and source voltages $\vec{E}(t)$ are known and we wish to find the currents $\vec{I}(t)$ and potentials $\vec{V}(t)$, can then be compactly written as

$$\mathcal{D}(\vec{I})(t) + \mathcal{A}^T \vec{V}(t) = \vec{E}(t), \quad (3.16)$$

$$\mathcal{A} \vec{I}(t) = -\vec{\Psi}(t). \quad (3.17)$$

If we solve Eqs. (3.16) and (3.17), we have solved the circuit problem. This system consists of $E + N$ equations, and we have $E + N$ unknowns. However, the equations are linearly dependent because of the non-trivial relationship between the currents $\vec{I}(t)$ and potentials $\vec{V}(t)$. It is therefore possible to find a smaller and linearly independent system of equations.

Assuming that the graph corresponding to the circuit has M connected components, the rank of the incidence matrix \mathcal{A} is $N - M$ and hence

$$\dim \ker(\mathcal{A}) = E - N + M.$$

We can then find a basis $\{\mathbf{u}_1, \mathbf{u}_2, \dots, \mathbf{u}_{E-N+M}\}$ of $\ker(\mathcal{A})$ as described in Sec. 3.3, with the property

$$\mathbf{u}_k^T \mathcal{A}^T = \mathbf{0} \quad \forall k = 1, 2, \dots, E - N + M.$$

Multiplying Eq. (3.16) with \mathbf{u}_k^T from the left thus results in the equations

$$\mathbf{u}_k^T \mathcal{D}(\vec{I})(t) = \mathbf{u}_k^T \vec{E}(t) \quad \forall k = 1, 2, \dots, E - N + M.$$

Next define the $E \times (E - N + M)$ matrix \mathbf{U} as

$$\mathbf{U} = (\mathbf{u}_1, \mathbf{u}_2, \dots, \mathbf{u}_{E-N+M}).$$

A new set of equations for the circuit problem is then

$$\mathbf{U}^T \mathcal{D}(\vec{I})(t) = \mathbf{U}^T \vec{E}(t), \quad (3.18)$$

together with $N - M$ linearly independent equations from (3.17). This is a set of exactly E equations where the unknowns are the E current intensities $\vec{I}(t)$. And once the currents are known, we can easily find the potentials $\vec{V}(t)$.

This method works for source voltages and currents of any form, and can handle both single phase and three-phase circuits, transient and stationary behaviour equally well in theory. But in practice it might require a numerical scheme because the equations involve both integrals and derivatives. Bermúdez proposes a general method using discretised time series, the backward formula as an approximation to the derivative and the composed trapezoidal rule as an approximation to the integral.

3.4.2 Harmonic problems

The circuit problem where all voltage and current sources are harmonic functions is simpler, as we can evaluate the required integrals and derivatives exactly and reduce the problem to a system of linear algebraic equations. This section also follows the methods of [28].

When the source voltages and currents are harmonic functions of time, so will all potentials and current intensities in the circuit be when we work with linear circuits. We therefore define

$$\vec{I}(t) = \operatorname{Re}(\tilde{\mathbb{I}}e^{i\omega t}), \quad (3.19)$$

$$\vec{V}(t) = \operatorname{Re}(\tilde{\mathbb{V}}e^{i\omega t}), \quad (3.20)$$

$$\vec{E}(t) = \operatorname{Re}(\tilde{\mathbb{E}}e^{i\omega t}), \quad (3.21)$$

$$\vec{\Psi}(t) = \operatorname{Re}(\tilde{\Psi}e^{i\omega t}), \quad (3.22)$$

where $\tilde{\mathbb{I}}$, $\tilde{\mathbb{V}}$, $\tilde{\mathbb{E}}$ and $\tilde{\Psi}$ are complex vectors, with the so-called complex amplitudes of their respective quantities. We now use i to denote the imaginary unit. Then for a general $\mathbb{A}e^{i\omega t}$,

$$\frac{d}{dt}\mathbb{A}e^{i\omega t} = i\omega\mathbb{A}e^{i\omega t}$$

and

$$\int \mathbb{A}e^{i\omega t} dt = \frac{1}{i\omega}\mathbb{A}e^{i\omega t}.$$

From this it can be seen that we can substitute the operator \mathcal{D} working on $(\vec{I})(t)$ as defined in Eqs. (3.14) and (3.15) by a product $\mathcal{D}(\omega)\tilde{\mathbb{I}}e^{i\omega t}$, where $\mathcal{D}(\omega)$ is a matrix defined by

$$\mathcal{D}(\omega)_{jj} = \begin{cases} R_j, & \text{if edge } j \text{ is a resistor} \\ -\frac{i}{\omega C_j}, & \text{if edge } j \text{ is a capacitor} \\ i\omega L_j, & \text{if edge } j \text{ is an inductor} \\ r_j, & \text{if edge } j \text{ is a power source} \end{cases} \quad (3.23)$$

and

$$\mathcal{D}(\omega)_S = i\omega\mathcal{L}^S, \quad (3.24)$$

where \mathcal{L}^S is the inductance matrix as before. $\mathcal{D}(\omega)$ is called the impedance matrix, as its diagonal elements equal the impedances (2.11), (2.12) and (2.13). The system of equations (3.16) and (3.17) can then be written as

$$\begin{aligned} \mathcal{D}(\omega)\tilde{\mathbb{I}}e^{i\omega t} + \mathcal{A}^T\tilde{\mathbb{V}}e^{i\omega t} &= \tilde{\mathbb{E}}e^{i\omega t}, \\ \mathcal{A}\tilde{\mathbb{I}}e^{i\omega t} &= -\tilde{\Psi}e^{i\omega t}, \end{aligned}$$

which simplifies to

$$\mathcal{D}(\omega)\tilde{\mathbb{I}} + \mathcal{A}^T\tilde{\mathbb{V}} = \tilde{\mathbb{E}}, \quad (3.25)$$

$$\mathcal{A}\tilde{\mathbb{I}} = -\tilde{\Psi}. \quad (3.26)$$

Equations (3.25) and (3.26) are only algebraic, and are therefore easily solvable if a solution exists. We can however reduce the number of equations as described in the general case. Let \mathbf{U} be a matrix with columns that form a basis of $\ker(\mathcal{A})$. Then

$$\mathbf{U}^T\mathcal{D}(\omega)\tilde{\mathbb{I}} = \mathbf{U}^T\tilde{\mathbb{E}} \quad (3.27)$$

together with $N - M$ independent equations from (3.26) constitute a system of E equations for the E unknowns $\tilde{\mathbb{I}}$. $\tilde{\mathbb{V}}$ can then be found from (3.25) as the solution of

$$\mathcal{A}^T\tilde{\mathbb{V}} = \tilde{\mathbb{E}} - \mathcal{D}(\omega)\tilde{\mathbb{I}}, \quad (3.28)$$

and we extract the real, time-dependent solutions $\vec{I}(t)$ and $\vec{V}(t)$ according to Eqs. (3.19) and (3.20).

Chapter 3. Graph theory

Chapter 4

Furnace power supply

4.1 Circuit models

We here define the circuit equivalent models of the furnace described in Sec. 1.1.2 that we will use for our further analysis. We first define models for the primary and secondary sides separately, and then combine them into one model for the entire system.

For all the models, we will need the impedance of the different elements. On the primary side, we know the voltage input from the grid and the capacitance. The conducting lines are set to have non-zero, but negligibly small, resistance. For the transformers we know the winding ratios, but not the inductance of either side, the mutual inductance or the resistance of the coils. Here we must resort to crude approximations, which we will do in Sec. 7.1. We can measure the electrode current and voltage as described in Sec. 4.5, and we can therefore calculate the electrode impedance.

4.1.1 Secondary side

We begin by modelling the secondary side circuit, that is the secondary side of the transformers and the furnace itself. Valderhaug [2] presents a detailed equivalent circuit of a submerged arc furnace for ferrosilicon in chapter 4.3.1 and Figure 4.5 of that chapter. Even though the values assigned to elements of this circuit will be different for a ferromanganese furnace, the structure is the same. The circuit model shows the different paths the currents can follow and models the different internal parts of the furnace with their own separated impedances. By assuming the electrode to electrode current to be negligible and lumping together some impedances, we can simplify the model somewhat. It is however still complicated enough that Valderhaug assumes symmetric conditions before proceeding with analytic studies.

We may make the model even simpler, by not modelling the arc and ohmic conduction between the electrodes and charge material separately. This is a possibly huge simplification, given that the arc is a non-linear element. We also assume that the electrodes are not mutually inductive, although in reality they are [2]. With these assumptions, we get the circuit diagram shown in Fig. 4.1a, which is the same equivalent circuit as the one used by Barker *et al.* [30]. The transformers are modelled as sinusoidal voltage sources with non-zero internal resistance, with the bus bars and flexible conductors as ideal conducting lines. The electrodes are modelled as elements with both resistive and inductive components and connected in a Y through the metal bath.

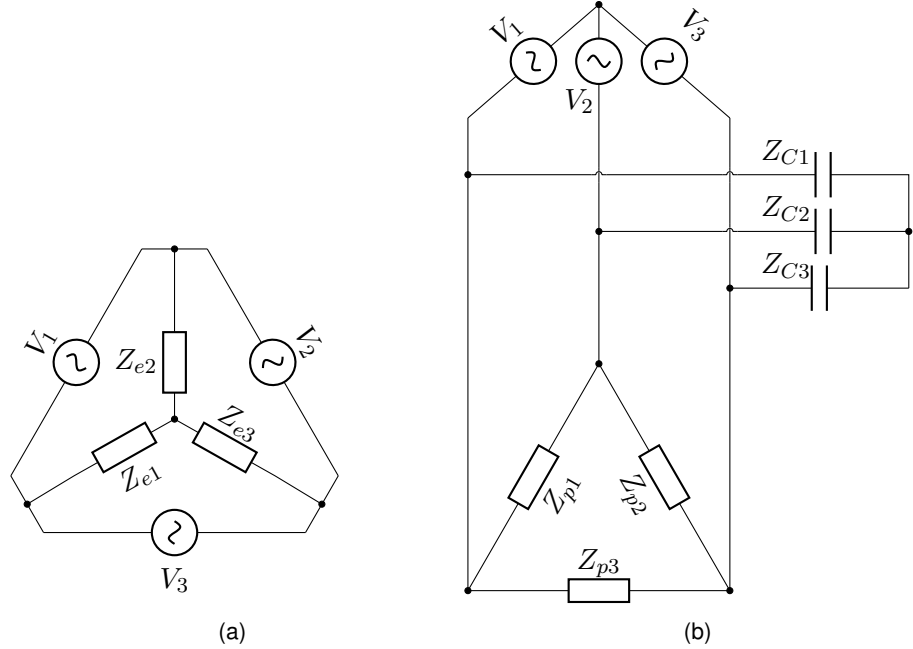


Figure 4.1: Circuit diagrams of (a) the secondary side equivalent circuit and (b) the primary side equivalent circuit.

4.1.2 Primary side

The primary side consists of the grid connection, capacitors for power factor correction and the primary side of the transformers, and we therefore do not need to make as many simplifications and assumptions. In order to impose a constant potential at the nodes connecting the grid to our circuit, we model the supply as three sinusoidal voltage sources that are connected in a Y on the grid side. We look at the primary side transformers as highly inductive elements with non-zero resistance that are connected in a Δ and model the capacitors as ideal. The resulting circuit diagram of the primary side model is shown in Fig. 4.1b. The conducting lines connecting the grid and capacitors to the Δ are given a negligible non-zero resistance which is not explicitly drawn.

4.1.3 Full equivalent circuit

Combining the primary and secondary side models described above gives us a model of the full system. We do that by substituting the primary side impedances and secondary side voltage sources with transformer equivalent circuits like the one in Fig. 2.3, connecting the two sides. The resulting circuit diagram is shown in Fig. 4.2. In this figure we have lumped the resistor and inductor of the non-ideal transformer into one inductor to simplify the drawing.

4.1.4 Low-voltage compensation

An alternative to high-voltage compensation as described in Sec. 2.3.1 is placing the capacitors on the secondary side, between the transformers and the furnace itself [31]. We call this low-voltage compensation (LVC), as the capacitors are placed on the low-voltage side. This is a far less established way of doing power factor correction, only recently being introduced as a serious option [31]. Figure 4.3 shows the setup as it

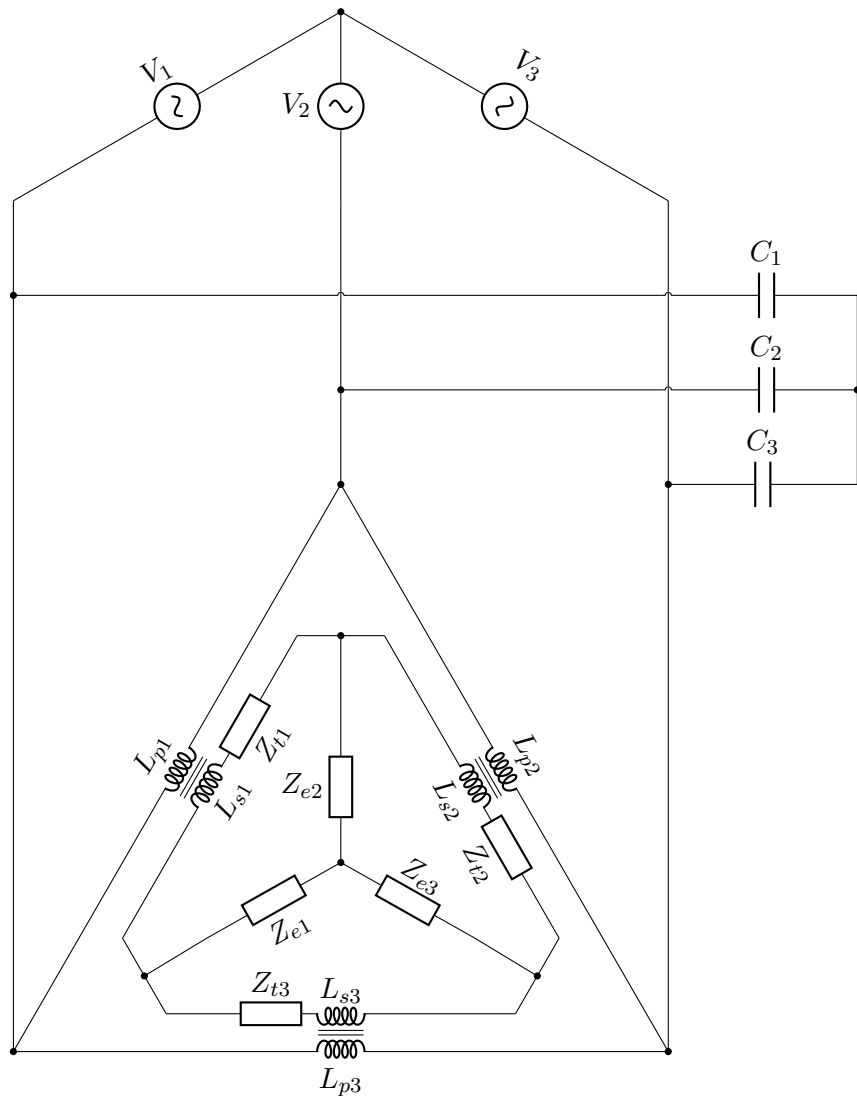


Figure 4.2: Circuit diagram of the full system, with the primary and secondary sides connected through transformers.

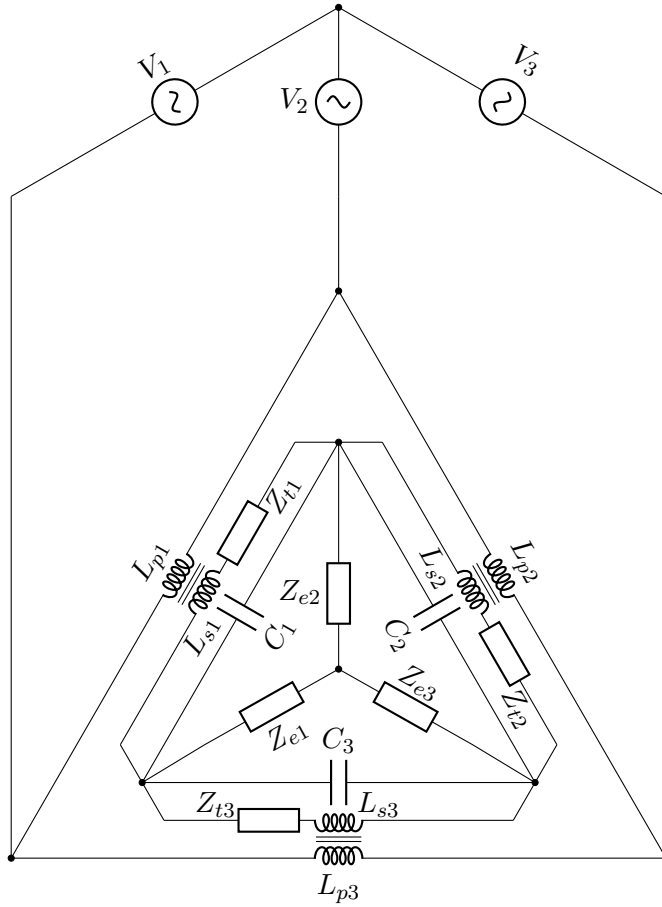


Figure 4.3: Circuit diagram of the full system with low-voltage compensation.

looks in our simplified model, where the capacitors are connected in parallel with the secondary side of the transformers. According to Li *et al.* [31], this has the advantage of making it possible to improve the power factor of the transformer, whereas primary side capacitors do not affect the transformers or secondary side at all [1], [27].

4.2 Defining circulating currents

There can exist circulating currents in the Δ connection on both the primary and secondary sides. Sævars Þóttir *et al.* [32] estimated the circulating current in the secondary side Δ due to skew tapping, a situation in which the three transformers operate at different tap positions and thus different secondary side voltages, by calculating the voltage difference and the impedance of the components. Although their calculations are based on a ferrosilicon furnace, the same situation can appear in a ferromanganese furnace. We can use the equivalent circuit models to calculate circulating current, but first we need to define circulating current as it appears in our model.

4.2.1 Secondary side

We want all the current being supplied to the secondary side to enter the electrodes and thus contribute to heating the furnace, but this will in general not be the case. There might be a so-called circulating current going around in the delta connection and never

entering the electrodes. This can be seen by decomposing the transformer currents I_x into the circulating current I_s and another part ΔI_x , such that

$$\begin{aligned}I_4 &= I_s + \Delta I_4 \\I_5 &= I_s + \Delta I_5 \\I_6 &= I_s + \Delta I_6.\end{aligned}$$

The currents going down into the electrodes are then

$$\begin{aligned}I_1 &= \Delta I_6 - \Delta I_4 \\I_2 &= \Delta I_4 - \Delta I_5 \\I_3 &= \Delta I_5 - \Delta I_6.\end{aligned}$$

We see that they are independent of I_s , and I_s is therefore truly a circulating current. If we require $\Delta I_4 + \Delta I_5 + \Delta I_6 = 0$, as would be the case for a balanced system with zero circulating current, the circulating current is given by

$$I_s = \frac{1}{3} (I_4 + I_5 + I_6). \quad (4.1)$$

4.2.2 Primary side

There can similarly exist a circulating current in the delta connection of the transformers on the primary side. We follow the same procedure as for the secondary side, defining transformer currents as deviation from circulating current I_s ,

$$\begin{aligned}I_{10} &= I_s + \Delta I_{10} \\I_{11} &= I_s + \Delta I_{11} \\I_{12} &= I_s + \Delta I_{12}.\end{aligned}$$

The current entering the transformer delta connection can then be expressed as

$$\begin{aligned}I_4 &= \Delta I_{11} - \Delta I_{10} \\I_5 &= \Delta I_{10} - \Delta I_{12} \\I_6 &= \Delta I_{12} - \Delta I_{10},\end{aligned}$$

which is independent of I_s . If we require $\Delta I_{10} + \Delta I_{11} + \Delta I_{12} = 0$, the circulating current is given by

$$I_s = \frac{1}{3} (I_{10} + I_{11} + I_{12}). \quad (4.2)$$

4.3 A furnace metamodel

As mentioned earlier, there are several well-developed physics-based models of submerged arc furnaces. However, one major drawback of physics-based models is the computational cost [33]. These models are therefore not fit for live simulations like control operations, or for running a large number of test cases in a short amount of time. A metamodel of one such physics-based has therefore been developed by Sparta et. al. [33]. A metamodel is here defined as “an approximation of an original physics-based model obtained by applying a suitable statistical analyses on a database generated with the original model” [33].

The metamodel is based on a physics-informed Finite Element Method (FEM) model. A database of inputs and outputs has been generated with due consideration of spanning the relevant input space as well as possible. Then they developed a statistical model based on this database using partial least squares regression. The resulting metamodel is computationally fast, and retains the general behaviour of the original FEM model. Input parameters are electrode currents, furnace geometry descriptors and conductivity of coke beds and charge. Outputs include electrode resistance and reactance, active and reactive power in different parts of the furnace.

A web-based simulator for the metamodel described above is openly available [34], [35], for both a ferromanganese [33] and a ferrosilicon [35] furnace. While this metamodel is static in nature, a sort of dynamic simulator has been made by generating input time series and successively solving the static model with changing input. For this thesis we have access to the source Python code for the ferromanganese model, so that we can build upon and make slight alterations to the functionality as needed. The metamodel can be used to for example find estimates of realistic parameters that are not readily available otherwise, study the effects of moving electrodes and run simulations.

4.4 Electrical furnace control

We distinguish between process control and process optimisation, as explained by Asphaug [1]. Process control is all about how to keep the furnace conditions stable under operation, whereas process optimisation is about finding the optimal working point. Here we present some control strategies for electrical control.

Controlling the electrical environment of the furnace is essential to keep it working optimally [5]. The electrical control consists of power controllers and electrode controllers. Power controllers work by adjusting the windings ratio of the transformer and electrode controllers work by adjusting the electrode displacement in order to control either the electrode current or the electrode resistance [2], [6]. We will be focusing on electrode control.

Electrode current control normally works as three monovariable controllers, and tries to control the current in each electrode separately by lowering or lifting that electrode. This comes with the problem of interaction, as moving one electrode causes the currents in the other two to change as well [36], but it is possible to design a so-called decoupled controller that is non-interacting [2]. The other option is three monovariable controllers that move the electrodes separately to control the resistance. In theory resistance control does not cause interaction [36]. However, the resistance calculation is based on voltage measurements that could be unreliable or difficult to maintain. The current is in contrast easy to measure accurately [2].

Current and resistance control can have structurally similar dead-zone control algorithm. We choose a current or resistance reference value that we aim for and a width for the so-called dead-zone around this reference value. The control system then works to keep the current or resistance within this dead-zone, by moving the electrode a fixed length after it has been outside of the dead-zone for a chosen length of time [2]. This waiting time is called the time-before-action period and is used to avoid moving the electrodes in response to fluctuations which correct themselves. The choice of parameter values for the reference value, width of the dead-zone and time-before-action will influence the performance of the control algorithm. For this thesis, we will use a resistance controller with parameter values supplied from a real world furnace.

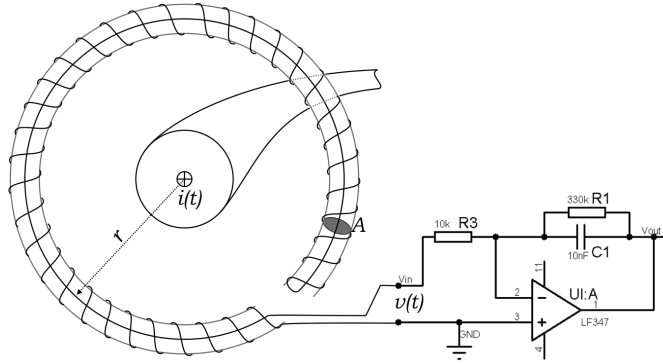


Figure 4.4: Schematic drawing of a Rogowski coil setup, from Wikimedia Commons [39]. The left part of the figure shows the Rogowski coil itself wrapped around the conducting line. The circuit to the right is the so-called integrator circuit.

4.5 Measurement strategies

In order to operate a furnace optimally, one needs to know the power consumption of the electrodes [37], and for this we need measurements of electrode current and voltage. For comparison with numerical models, we will also use measurements of transformer voltages and currents. Electrode currents are measured with a standard setup of an equivalent circuit on the primary side [1], and transformer voltages are measured directly by a voltmeter. The last two measurements are more complicated. For the secondary side transformer currents we can use Rogowski coils, and electrode voltages are measured with a technique called the Bøckman method.

4.5.1 Rogowski coils

Rogowski coils are used for measuring AC currents, based on Ampere's and Faradays' laws [38]. A schematic drawing of a Rogowski coil is shown in Fig. 4.4. The Rogowski coil itself is the coil wrapped around the conductor we wish to measure the current in. The changing current $i(t)$ in the conductor will then induce a voltage $v(t)$ in the Rogowski coil. The measured voltage in the coil is therefore proportional to the derivative of the current in the conductor,

$$v(t) = \frac{A}{s} \mu_0 \frac{di}{dt} \Big|_{t'=t}, \quad (4.3)$$

where $v(t)$ is the measured voltage, A is the cross-section area of the windings, s is the number of windings per unit length, μ_0 is the permeability constant and $\frac{di}{dt}$ is the derivative of the current [38]. Integrating this voltage signal we can thus find the current in the conductor, and the circuit connected to the Rogowski coil in Fig. 4.4 is an integrator circuit designed to do that.

Rogowski coils are advantageous because of their flexibility, relatively low cost, good transient response and ability to measure a large range of currents with large variations in frequency [38].

4.5.2 The Bøckman method

While measuring electrode currents is straightforward, measuring the voltage between the electrodes and the furnace bottom is more complicated. Simply connecting a point of the furnace bottom to a conductor to get the potential in the furnace bottom will

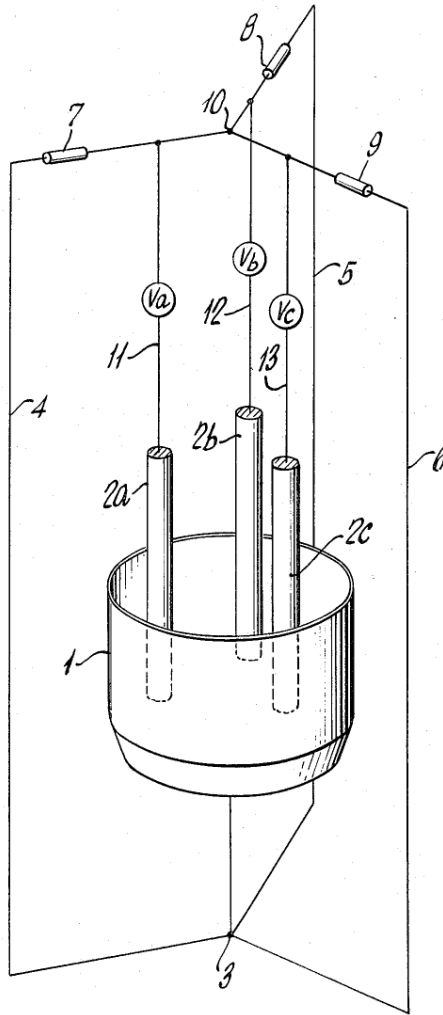


Figure 4.5: Schematic drawing of the Böckman method, courtesy of Böckman [41].

result in potentially large errors, as there will be non-negligible induced voltages in any such conductor due to the strong magnetic fields present. To remedy this one can use the so-called Böckman method [40], [41].

A schematic drawing of the measurement configuration in the Böckman method is shown in Fig. 4.5. Instead of using a single conductor, one connects three conducting lines to the furnace bottom, lines 4, 5, and 6 in the drawing. The conducting lines are placed symmetrically around the furnace, led to a point above the furnace with weak magnetic fields and connected through three equal resistances, 7, 8, and 9, in a Y connection, 10 on the drawing. The idea is that in the perfectly balanced case and with this symmetric arrangement, the induced voltages will cancel each other as they have the same magnitude and will be $2\pi/3$ radians shifted with respect to each other. That leaves us with the true potential of the furnace bottom. However, the measurements can still be faulty if the furnace is unbalanced [37]. While the Böckman method is the most accurate way of measuring electrode voltage, it can be difficult to implement and maintain reliably [1].

Chapter 5

Analytical solutions

Analytical approaches are feasible when treating the primary and secondary sides separately. In this chapter we thus find analytical solutions to these circuits separately, both in the balanced and unbalanced case, and use them to find analytical expressions for circulating currents, effects and power factor. We will need digraphs representing the circuit diagrams in Fig. 4.1, and they are presented in Fig. 5.1. When treating the whole system as one, we will need to use numerics.

5.1 Secondary side

The incidence matrix of the secondary side digraph in Fig. 5.1a is

$$\mathcal{A} = \begin{bmatrix} 1 & 1 & 1 & 0 & 0 & 0 \\ -1 & 0 & 0 & -1 & 0 & 1 \\ 0 & -1 & 0 & 1 & -1 & 0 \\ 0 & 0 & -1 & 0 & 1 & -1 \end{bmatrix}$$

and the inductance matrix is

$$\mathcal{D} = \begin{bmatrix} Z_{e1} & 0 & 0 & 0 & 0 & 0 \\ 0 & Z_{e2} & 0 & 0 & 0 & 0 \\ 0 & 0 & Z_{e3} & 0 & 0 & 0 \\ 0 & 0 & 0 & Z_{v1} & 0 & 0 \\ 0 & 0 & 0 & 0 & Z_{v2} & 0 \\ 0 & 0 & 0 & 0 & 0 & Z_{v3} \end{bmatrix},$$

where Z_{ei} , $i = 1, 2, 3$ are the electrode impedances and Z_{vi} , $i = 1, 2, 3$ are the source voltage impedances. Edges 4, 5 and 6 have voltage sources and there are no current sources, giving the vectors

$$\tilde{\mathbf{E}} = [0 \ 0 \ 0 \ V_1 \ V_2 \ V_3],$$

$$\tilde{\Psi} = [0 \ 0 \ 0 \ 0].$$

Following the method in Sec. 3.3, we find the basis of $\ker(\mathcal{A})$ to be

$$\mathbf{U} = \begin{bmatrix} -1 & 0 & 1 \\ 1 & -1 & 0 \\ 0 & 1 & -1 \\ 1 & 0 & 0 \\ 0 & 1 & 0 \\ 0 & 0 & 1 \end{bmatrix},$$

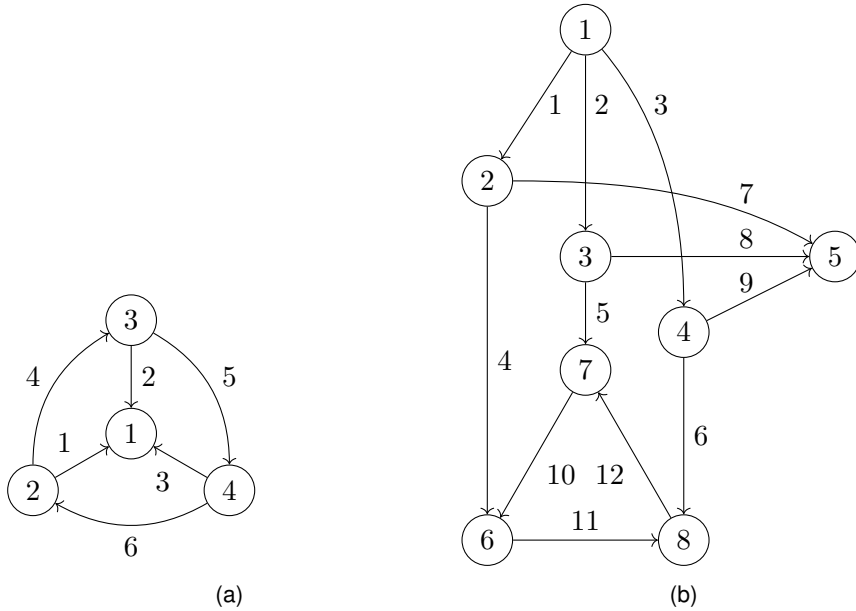


Figure 5.1: Directed graphs of (a) the secondary side circuit and (b) the primary side circuit.

resulting in the matrix equation

$$\begin{bmatrix} -Z_{e1} & Z_{e2} & 0 & Z_{v1} & 0 & 0 \\ 0 & -Z_{e2} & Z_{e3} & 0 & Z_{v2} & 0 \\ Z_{e1} & 0 & -Z_{e3} & 0 & 0 & Z_{v3} \\ 1 & 1 & 1 & 0 & 0 & 0 \\ -1 & 0 & 0 & -1 & 0 & 1 \\ 0 & -1 & 0 & 1 & -1 & 0 \end{bmatrix} \begin{bmatrix} I_1 \\ I_2 \\ I_3 \\ I_4 \\ I_5 \\ I_6 \end{bmatrix} = \begin{bmatrix} V_1 \\ V_2 \\ V_3 \\ 0 \\ 0 \\ 0 \end{bmatrix}. \quad (5.1)$$

This equation can be solved analytically, and we will be using SymPy [42] to do so.

5.1.1 Balanced circuit

In a balanced circuit the three source voltages are phase shifted by $2\pi/3$ relative to each other such that $V_1 + V_2 + V_3 = 0$, the electrode impedances are equal, meaning that $Z_{e1} = Z_{e2} = Z_{e3} = Z_e$, and the impedances of the source voltages are equal, $Z_{v1} = Z_{v2} = Z_{v3} = Z_v$. The solution of Eq. (5.1) is then

$$\begin{bmatrix} I_1 \\ I_2 \\ I_3 \\ I_4 \\ I_5 \\ I_6 \end{bmatrix} = \frac{1}{3Z_e + Z_v} \begin{bmatrix} V_3 - V_1 \\ V_1 - V_2 \\ V_2 - V_3 \\ V_1 \\ V_2 \\ V_3 \end{bmatrix}. \quad (5.2)$$

The circulating current as defined in Eq. (4.1) is

$$I_s = \frac{1}{3} (I_4 + I_5 + I_6) = \frac{V_1 + V_2 + V_3}{9Z_e + 3Z_v} = 0. \quad (5.3)$$

In a balanced circuit there is no circulating current.

5.1.2 Unbalanced electrodes

In a circuit where the electrodes are unbalanced, we still have $V_1 + V_2 + V_3 = 0$ and $Z_{v1} = Z_{v2} = Z_{v3} = Z_v$, but the electrode impedances are not equal. This will virtually always be the case in a real furnace during operation, since the electrodes are moved independently and the material in the furnace is not distributed perfectly symmetrical around them. In this case we get a solution of the form

$$\begin{bmatrix} I_1 \\ I_2 \\ I_3 \\ I_4 \\ I_5 \\ I_6 \end{bmatrix} = \frac{1}{\alpha} \begin{bmatrix} V_3(3Z_{e2} + Z_v) - V_1(3Z_{e3} + Z_v) \\ V_1(3Z_{e3} + Z_v) - V_2(3Z_{e1} + Z_v) \\ V_2(3Z_{e1} + Z_v) - V_3(3Z_{e2} + Z_v) \\ 2V_1Z_{e3} + V_1Z_v - V_2Z_{e1} - V_3Z_{e2} \\ 2V_2Z_{e1} + V_2Z_v - V_3Z_{e2} - V_1Z_{e3} \\ 2V_3Z_{e2} + V_3Z_v - V_1Z_{e3} - V_2Z_{e1} \end{bmatrix}, \quad (5.4)$$

where

$$\alpha = 3Z_{e1}Z_{e2} + 3Z_{e1}Z_{e3} + 2Z_{e1}Z_v + 3Z_{e2}Z_{e3} + 2Z_{e2}Z_v + 2Z_{e3}Z_v + Z_v^2.$$

The circulating current is

$$I_s = \frac{1}{3} (I_4 + I_5 + I_6) = \frac{V_1Z_v + V_2Z_v + V_3Z_v}{3\alpha} = 0. \quad (5.5)$$

There is no circulating current, even if the electrode impedances are not equal.

5.1.3 Unbalanced transformers

Unbalanced transformers may occur in some control scenarios, where the operators choose to use different windings ratios for different transformers [1], [32], and possibly if the transformers used are not of the same production. If the transformers are unbalanced, we model that as the voltage sources on the secondary side having different internal resistances, or more generally different impedances, but still assume that the supplied voltages are phase shifted by $2\pi/3$ compared to each other and of the same magnitude. However, for comparison with the study by Sævarsþóttir *et al.* [32], and perhaps more realistic, would be to look at unbalanced supply voltages. Thus, we have that $V_1 + V_2 + V_3 = 0$ and $Z_{e1} = Z_{e2} = Z_{e3} = Z_e$. The solution is in this case

$$\begin{bmatrix} I_1 \\ I_2 \\ I_3 \\ I_4 \\ I_5 \\ I_6 \end{bmatrix} = \frac{1}{\alpha} \begin{bmatrix} V_3(Z_{v1}Z_{v2} + Z_{v1}Z_e + Z_{v2}Z_e + Z_{v3}Z_e) - V_1(Z_{v2}Z_{v3} + Z_{v1}Z_e + Z_{v2}Z_e + Z_{v3}Z_e) \\ V_1(Z_{v2}Z_{v3} + Z_{v1}Z_e + Z_{v2}Z_e + Z_{v3}Z_e) - V_2(Z_{v1}Z_{v3} + Z_{v1}Z_e + Z_{v2}Z_e + Z_{v3}Z_e) \\ V_2(Z_{v1}Z_{v3} + Z_{v1}Z_e + Z_{v2}Z_e + Z_{v3}Z_e) - V_3(Z_{v1}Z_{v2} + Z_{v1}Z_e + Z_{v2}Z_e + Z_{v3}Z_e) \\ V_1Z_{v2}Z_{v3} + 2V_1Z_{v2}Z_e + 2V_1Z_{v3}Z_e + V_2Z_{v3}Z_e + V_3Z_{v2}Z_e \\ V_1Z_{v3}Z_e + V_2Z_{v1}Z_{v3} + 2V_2Z_{v1}Z_e + 2V_2Z_{v3}Z_e + V_3Z_{v1}Z_e \\ V_1Z_{v2}Z_e + V_2Z_{v1}Z_e + V_3Z_{v1}Z_{v2} + 2V_3Z_{v1}Z_e + 2V_3Z_{v2}Z_e \end{bmatrix}, \quad (5.6)$$

where

$$\alpha = Z_{v1}Z_{v2}Z_{v3} + 2Z_{v1}Z_{v2}Z_e + 2Z_{v1}Z_{v3}Z_e + 3Z_{v1}Z_e^2 + 2Z_{v2}Z_{v3}Z_e + 3Z_{v2}Z_e^2 + 3Z_{v3}Z_e^2.$$

We get a non-zero circulating current

$$I_s = \frac{1}{3} (I_4 + I_5 + I_6) = \frac{V_1(Z_{v2}Z_{v3} - 3Z_{v1}Z_e) + V_2(Z_{v1}Z_{v3} - 3Z_{v2}Z_e) + V_3(Z_{v1}Z_{v2} - 3Z_{v3}Z_e)}{3\alpha}. \quad (5.7)$$

5.2 Primary side

The incidence matrix and impedance matrix of the digraph in Fig. 5.1b are

$$\mathcal{A} = \begin{bmatrix} -1 & -1 & -1 & 0 & 0 & 0 & 0 & 0 & 0 & 0 & 0 & 0 \\ 1 & 0 & 0 & -1 & 0 & 0 & -1 & 0 & 0 & 0 & 0 & 0 \\ 0 & 1 & 0 & 0 & -1 & 0 & 0 & -1 & 0 & 0 & 0 & 0 \\ 0 & 0 & 1 & 0 & 0 & -1 & 0 & 0 & -1 & 0 & 0 & 0 \\ 0 & 0 & 0 & 0 & 0 & 0 & 1 & 1 & 1 & 0 & 0 & 0 \\ 0 & 0 & 0 & 1 & 0 & 0 & 0 & 0 & 0 & 1 & -1 & 0 \\ 0 & 0 & 0 & 0 & 1 & 0 & 0 & 0 & 0 & -1 & 0 & 1 \\ 0 & 0 & 0 & 0 & 0 & 1 & 0 & 0 & 0 & 0 & 1 & -1 \end{bmatrix},$$

$$\mathcal{D} = \begin{bmatrix} Z & 0 & 0 & 0 & 0 & 0 & 0 & 0 & 0 & 0 & 0 & 0 \\ 0 & Z & 0 & 0 & 0 & 0 & 0 & 0 & 0 & 0 & 0 & 0 \\ 0 & 0 & Z & 0 & 0 & 0 & 0 & 0 & 0 & 0 & 0 & 0 \\ 0 & 0 & 0 & Z & 0 & 0 & 0 & 0 & 0 & 0 & 0 & 0 \\ 0 & 0 & 0 & 0 & Z & 0 & 0 & 0 & 0 & 0 & 0 & 0 \\ 0 & 0 & 0 & 0 & 0 & Z & 0 & 0 & 0 & 0 & 0 & 0 \\ 0 & 0 & 0 & 0 & 0 & 0 & Z_{C1} & 0 & 0 & 0 & 0 & 0 \\ 0 & 0 & 0 & 0 & 0 & 0 & 0 & Z_{C2} & 0 & 0 & 0 & 0 \\ 0 & 0 & 0 & 0 & 0 & 0 & 0 & 0 & Z_{C3} & 0 & 0 & 0 \\ 0 & 0 & 0 & 0 & 0 & 0 & 0 & 0 & 0 & Z_{p1} & 0 & 0 \\ 0 & 0 & 0 & 0 & 0 & 0 & 0 & 0 & 0 & 0 & Z_{p3} & 0 \\ 0 & 0 & 0 & 0 & 0 & 0 & 0 & 0 & 0 & 0 & 0 & Z_{p2} \end{bmatrix},$$

where the impedance of edges 1 to 6 are set to the same Z , representing a small non-zero resistance in the conducting wires, Z_{Ci} , $i = 1, 2, 3$ are the impedances of the capacitors and Z_{pi} , $i = 1, 2, 3$ are the impedances of the primary side transformers. The complex amplitudes of the source voltages and currents are

$$\tilde{\mathbb{E}} = [V_1 \ V_2 \ V_3 \ 0 \ 0 \ 0 \ 0 \ 0 \ 0 \ 0 \ 0 \ 0],$$

$$\tilde{\Psi} = [0 \ 0 \ 0 \ 0 \ 0 \ 0 \ 0 \ 0 \ 0 \ 0],$$

and the basis of $\ker(\mathcal{A})$ is

$$\mathbf{U} = \begin{bmatrix} -1 & -1 & -1 & 1 & 0 \\ 1 & 0 & 1 & 0 & -1 \\ 0 & 1 & 0 & -1 & 1 \\ 0 & 0 & -1 & 1 & 0 \\ 0 & 0 & 1 & 0 & -1 \\ 0 & 0 & 0 & -1 & 1 \\ -1 & -1 & 0 & 0 & 0 \\ 1 & 0 & 0 & 0 & 0 \\ 0 & 1 & 0 & 0 & 0 \\ 0 & 0 & 1 & 0 & 0 \\ 0 & 0 & 0 & 1 & 0 \\ 0 & 0 & 0 & 0 & 1 \end{bmatrix}.$$

The equation for the primary side system is then

$$\begin{bmatrix} -Z & Z & 0 & 0 & 0 & -Z_{C1} & Z_{C2} & 0 & 0 & 0 & 0 \\ -Z & 0 & Z & 0 & 0 & -Z_{C1} & 0 & Z_{C3} & 0 & 0 & 0 \\ -Z & Z & 0 & -Z & Z & 0 & 0 & 0 & Z_{p1} & 0 & 0 \\ Z & 0 & -Z & Z & 0 & -Z & 0 & 0 & 0 & Z_{p3} & 0 \\ 0 & -Z & Z & 0 & -Z & Z & 0 & 0 & 0 & 0 & Z_{p2} \\ -1 & -1 & -1 & 0 & 0 & 0 & 0 & 0 & 0 & 0 & 0 \\ 1 & 0 & 0 & -1 & 0 & 0 & -1 & 0 & 0 & 0 & 0 \\ 0 & 1 & 0 & 0 & -1 & 0 & 0 & -1 & 0 & 0 & 0 \\ 0 & 0 & 1 & 0 & 0 & -1 & 0 & 0 & 0 & 0 & 0 \\ 0 & 0 & 0 & 0 & 0 & 1 & 1 & 1 & 0 & 0 & 0 \\ 0 & 0 & 0 & 1 & 0 & 0 & 0 & 0 & 1 & -1 & 0 \\ 0 & 0 & 0 & 0 & 1 & 0 & 0 & 0 & -1 & 0 & 1 \end{bmatrix} = \begin{bmatrix} I_1 \\ I_2 \\ I_3 \\ I_4 \\ I_5 \\ I_6 \\ I_7 \\ I_8 \\ I_9 \\ I_{10} \\ I_{11} \\ I_{12} \end{bmatrix} = \begin{bmatrix} V_2 - V_1 \\ V_3 - V_1 \\ V_2 - V_1 \\ V_1 - V_3 \\ V_3 - V_2 \\ 0 \\ 0 \\ 0 \\ 0 \\ 0 \\ 0 \\ 0 \end{bmatrix}. \quad (5.8)$$

5.2.1 Balanced circuit

The three voltage sources are balanced such that $V_1 + V_2 + V_3 = 0$, the capacitors have equal impedances $Z_{C1} = Z_{C2} = Z_{C3} = Z_C$ and the transformers have equal impedances $Z_{p1} = Z_{p3} = Z_{p2} = Z_p$. The solution of Eq. (5.8) is then

$$\begin{bmatrix} I_1 \\ I_2 \\ I_3 \\ I_4 \\ I_5 \\ I_6 \\ I_7 \\ I_8 \\ I_9 \\ I_{10} \\ I_{11} \\ I_{12} \end{bmatrix} = \frac{1}{3Z^2 + 6ZZ_C + ZZ_p + Z_CZ_p} \begin{bmatrix} V_1(3Z + 3Z_C + Z_p) \\ V_2(3Z + 3Z_C + Z_p) \\ V_3(3Z + 3Z_C + Z_p) \\ 3V_1Z_C \\ 3V_2Z_C \\ 3V_3Z_C \\ V_1(3Z + Z_p) \\ V_2(3Z + Z_p) \\ V_3(3Z + Z_p) \\ V_2Z_C - V_1Z_C \\ V_1Z_C - V_3Z_C \\ V_3Z_C - V_2Z_C \end{bmatrix}, \quad (5.9)$$

and the circulating current in the delta connected transformers, as defined in Eq. (4.2), is

$$I_s = \frac{1}{3} (I_{10} + I_{11} + I_{12}) = \frac{V_2Z_C - V_1Z_C + V_1Z_C - V_3Z_C + V_3Z_C - V_2Z_C}{9Z^2 + 18ZZ_C + 3ZZ_p + 3Z_CZ_p} = 0. \quad (5.10)$$

We can also calculate the reactive power Q , active power P and apparent power S in the primary side transformers and capacitors. We assume that the load in the conductors is purely resistive, such that $Z = R$ for some resistance R , and that the load in the conductors is purely reactive, such that $Z_C = -j/\omega C$ for some angular frequency ω and capacitance C . The impedance of the transformers are assumed to have both resistive and reactive elements, such that $Z_p = R_p + j\omega L$ for some resistance R_p , angular

frequency ω and inductance L . The reactive power in a transformer is then

$$\begin{aligned}
 Q_{10} &= \frac{1}{2}|I_{10}|^2 X_{p1} \\
 &= \frac{1}{2} \left| \frac{-V_1 Z_C + V_2 Z_C}{3Z^2 + 6ZZ_C + ZZ_p + Z_C Z_p} \right|^2 X_{p1} \\
 &= \frac{1}{2} \left| \frac{jV_0 \frac{1}{\omega C} - j \left(-\frac{1}{2} + j \frac{\sqrt{3}}{2} \right) V_0 \frac{1}{\omega C}}{3R^2 - j6R \frac{1}{\omega C} + R(R_p + j\omega L) - j \frac{1}{\omega C} (R_p + j\omega L)} \right|^2 \omega L \\
 &= \frac{V_0^2}{8\omega^2 C^2} \frac{\sqrt{3}^2 + 3^2}{\left(3R^2 + RR_p + \frac{L}{C} \right)^2 + \left(-\frac{6R}{\omega C} + R\omega L - \frac{R_p}{\omega C} \right)^2} \omega L \\
 &= \frac{\frac{3}{2} V_0^2 \omega L}{\left(3R^2 + RR_p + \frac{L}{C} \right)^2 \omega^2 C^2 + \left(-\frac{6R}{\omega C} + R\omega L - \frac{R_p}{\omega C} \right)^2 \omega^2 C^2},
 \end{aligned}$$

and because of symmetry the three primary side transformers have the same reactive power

$$Q_p = \frac{\frac{3}{2} V_0^2 \omega L}{\left(3R^2 + RR_p + \frac{L}{C} \right)^2 \omega^2 C^2 + \left(-\frac{6R}{\omega C} + R\omega L - \frac{R_p}{\omega C} \right)^2 \omega^2 C^2}. \quad (5.11)$$

For the capacitors

$$\begin{aligned}
 Q_7 &= \frac{1}{2}|I_7|^2 X_{C1} \\
 &= \frac{1}{2} \left| \frac{V_1(3Z + Z_p)}{3Z^2 + 6ZZ_C + ZZ_p + Z_C Z_p} \right|^2 X_{C1} \\
 &= \frac{\frac{1}{2} \left(9R^2 + 6RR_p + R_p^2 + \omega^2 L^2 \right) V_0^2 \omega C}{\left(3R^2 + RR_p + \frac{L}{C} \right)^2 \omega^2 C^2 + \left(-\frac{6R}{\omega C} + R\omega L - \frac{R_p}{\omega C} \right)^2 \omega^2 C^2},
 \end{aligned}$$

and again because of symmetry the reactive power of all three capacitors is

$$Q_C = \frac{\frac{1}{2} \left(9R^2 + 6RR_p + R_p^2 + \omega^2 L^2 \right) V_0^2 \omega C}{\left(3R^2 + RR_p + \frac{L}{C} \right)^2 \omega^2 C^2 + \left(-\frac{6R}{\omega C} + R\omega L - \frac{R_p}{\omega C} \right)^2 \omega^2 C^2}. \quad (5.12)$$

We similarly find that

$$P_p = \frac{\frac{3}{2} V_0^2 R_p}{\left(3R^2 + RR_p + \frac{L}{C} \right)^2 \omega^2 C^2 + \left(-\frac{6R}{\omega C} + R\omega L - \frac{R_p}{\omega C} \right)^2 \omega^2 C^2}$$

and

$$P_C = 0$$

since the capacitors are purely reactive. The apparent power is then

$$\begin{aligned}
 S_p &= \sqrt{P_p^2 + Q_p^2} \\
 &= \frac{\frac{3}{2} V_0^2 \sqrt{R_p^2 + \omega^2 L^2}}{\left(3R^2 + RR_p + \frac{L}{C} \right)^2 \omega^2 C^2 + \left(-\frac{6R}{\omega C} + R\omega L - \frac{R_p}{\omega C} \right)^2 \omega^2 C^2}
 \end{aligned}$$

and

$$\begin{aligned} S_C &= \sqrt{P_C^2 + Q_C^2} \\ &= \frac{\frac{1}{2} (9R^2 + 6RR_p + R_p^2 + \omega^2 L^2) V_0^2 \omega C}{(3R^2 + RR_p + \frac{L}{C})^2 \omega^2 C^2 + \left(-\frac{6R}{\omega C} + R\omega L - \frac{R_p}{\omega C}\right)^2 \omega^2 C^2} \end{aligned}$$

for the transformers and capacitors, respectively.

5.2.2 Unbalanced capacitors

We can also find the solution when we have unbalanced capacitors, that is with $V_1 + V_2 + V_3 = 0$ and $Z_{p1} = Z_{p3} = Z_{p2} = Z_p$, but not equal capacitor impedances. The expressions are quite long and can be found in Eq. B.1 in Appendix B. We find that the circulating current in the delta is

$$I_s = \frac{1}{3} (I_{10} + I_{11} + I_{12}) = 0, \quad (5.13)$$

so unbalanced capacitors do not lead to a circulating current.

5.2.3 Unbalanced transformers

When the transformers are unbalanced we have $V_1 + V_2 + V_3 = 0$ and $Z_{C1} = Z_{C2} = Z_{C3} = Z_C$. The current solution is shown in Eq. B.2 in Appendix B. We find the circulating current in the delta to be

$$\begin{aligned} I_s &= \frac{1}{3} (I_{10} + I_{11} + I_{12}) \\ &= \frac{V_1 Z_C (3Z^2 + ZZ_{p2} + 6ZZ_C + Z_{p2}Z_C)(Z_{p1} - Z_{p3})}{3\alpha} \\ &\quad + \frac{V_2 Z_C (3Z^2 + ZZ_{p3} + 6ZZ_C + Z_{p3}Z_C)(Z_{p2} - Z_{p1})}{3\alpha} \\ &\quad + \frac{V_3 Z_C (3Z^2 + ZZ_{p1} + 6ZZ_C + Z_{p1}Z_C)(Z_{p3} - Z_{p2})}{3\alpha}. \end{aligned}$$

When the transformers are unbalanced, there is a non-zero circulating current in the delta connected transformers on the primary side.

5.2.4 Power factor and capacitance

The power factor observed by the grid, corresponding to the power factor of edges 1, 2 and 3 in Fig. 5.1b, should ideally be 1, and this is the reason for including capacitors as high-voltage compensation. Assuming the circuit to be balanced, we can find the power factor directly from the phase difference between the voltage V_1 and current I_1 from Eq. (5.9). The voltage is

$$V_1 = V_0$$

for some real number V_0 , and thus has phase angle 0 in the complex plane. For the current expression we substitute $Z = R$, $Z_C = -j/\omega C$ and $Z_p = R_p + j\omega L$ as before.

This gives us a current

$$\begin{aligned} I_1 &= \frac{V_1(3Z + 3Z_C + Z_p)}{3Z^2 + 6ZZ_C + ZZ_p + Z_CZ_p} \\ &= V_0 \frac{3R - 3j\frac{1}{\omega C} + R_p + j\omega L}{3R^2 - j6R\frac{1}{\omega C} + R(R_p + j\omega L) - j\frac{1}{\omega C}(R_p + j\omega L)} \\ &\propto 9R^3 + 6R^2R_p - 6\frac{RL}{C} + RR_p^2 + R\omega^2L^2 + \frac{18R + 3R_p}{\omega^2C^2} \\ &\quad + j \left(\frac{9R^2 + 6RR_p + R_p^2 + \omega^2L^2}{\omega C} - \frac{3L}{\omega C^2} \right). \end{aligned}$$

We then find the power factor from the phase angle of $I_1 \propto a + jb$. Since we have a power supply and not power consumption at this point in the circuit, we let the power factor be the positive angle of I_1 instead of the negative angle.

$$\cos \varphi = \frac{a}{\sqrt{a^2 + b^2}}.$$

We can differentiate the above expression with respect to C to find the capacitance that gives us the greatest power factor, but this is a tedious process. Instead, we use the fact that $\cos \varphi = 1$ when $b = 0$. This gives us the equation

$$\frac{9R^2 + 6RR_p + R_p^2 + \omega^2L^2}{\omega C} - \frac{3L}{\omega C^2} = 0,$$

which solving for C yields

$$C_{\text{opt}} = \frac{3L}{9R^2 + 6RR_p + R_p^2 + \omega^2L^2}. \quad (5.14)$$

Under the assumptions we have made, this would then be the optimal choice of C .

Another approach is to set the reactive power in Eq. (5.11) of the transformers equal to the reactive power in Eq. (5.12) of the capacitors, as these are the only elements in the circuit with reactive components. The resulting equation shortens to

$$3L = (9R^2 + 6RR_p + R_p^2 + \omega^2L^2)C,$$

which solving for C gives the criterion

$$C_{\text{opt}} = \frac{3L}{9R^2 + 6RR_p + R_p^2 + \omega^2L^2},$$

agreeing with the optimal choice of C found in Eq. (5.14) above. We interpret this as all the reactive power being pumped between the capacitors and transformers, and thus none of the reactive power leaks back into the power grid.

Looking at current values at limits for C is also instructive. We have

$$\begin{aligned} \lim_{C \rightarrow \infty} I_1 &= V_0 \lim_{Z_C \rightarrow 0} \frac{3Z + 3Z_C + Z_p}{3Z^2 + 6ZZ_C + ZZ_p + Z_CZ_p} \\ &= V_0 \frac{3Z + Z_p}{3Z^2 + ZZ_p} \\ &= \frac{V_0}{Z}, \end{aligned}$$

and thus a power factor $\cos \varphi = 1$ for this limit. It is however useless in practice, as capacitors with infinite capacitance corresponds to having conductors with no resistance. All the current would therefore flow in this loop, and no current would enter the transformers. The other limit is

$$\begin{aligned}\lim_{C \rightarrow 0} I_1 &= V_0 \lim_{Z_C \rightarrow \infty} \frac{3Z + 3Z_C + Z_p}{3Z^2 + 6ZZ_C + ZZ_p + Z_C Z_p} \\ &= \frac{3V_0}{6Z + Z_p} \\ &= \frac{3V_0}{6R + R_p + j\omega L} \\ &= \frac{3V_0 (6R + R_p - j\omega L)}{(6R + R_p)^2 + (\omega L)^2} \\ &\propto 6R + R_p - j\omega L,\end{aligned}$$

with a power factor

$$\cos \varphi = \frac{6R + R_p}{\sqrt{(6R + R_p)^2 + (\omega L)^2}}.$$

This is the power factor one would get without having the capacitors as part of the circuit and thus without power factor correction.

Chapter 5. Analytical solutions

Chapter 6

Implementation

To look at bigger circuit problems than those in the previous chapter, we need to move on from analytical solutions to numerics. We implement a numerical solver for our circuit problems as a Python module, using the solution method in Sec. 3.4.2 for harmonic circuit problems. In our numerical solver the solution method is implemented as shown in Algorithm 1, with the use of NumPy [43]. The Python module is organised as a class hierarchy with different circuits making up the different classes. The base class *Circuit* takes any incidence matrix \mathcal{A} as argument, but to ensure the solver works properly, we have the following rules for numbering nodes and edges of the graph:

1. if there are M connected components, the last M nodes must be from different connected components,
2. edges must be numbered such that the edges constituting a spanning forest come first.

The most important function for this class is *solve*, which takes the impedance matrix \mathcal{D} , vector of source voltages $\tilde{\mathbf{E}}$ and vector of source currents $\tilde{\Psi}$ as input and solves for current and voltage amplitudes $\tilde{\mathbf{I}}$, $\tilde{\mathbf{V}}$ at all points in the circuit using Algorithm 1. With this implementation, the defining element of the class instance is the circuit geometry as represented by the incidence matrix, and the same circuit can be solved multiple times with different impedance values and different source voltages and currents. After *solve* has been called, we can call the other functions to get more information. We can extract time series of currents, node voltages and voltage drops over components for a specified number of time periods and calculate active, reactive, apparent and total power, as well as power factor. All other functions use the last current and voltage solutions from *solve*, and calling *solve* again will overwrite the previous solution with the new one.

As we will mostly be working with specific circuit configurations, we have subclasses for those where we do not need to supply the incidence matrix every time. They are *Primary*, with incidence matrix corresponding to the graph in Fig. 5.1b, *Secondary*, for the graph in Fig. 5.1a, *HVC*, for the graph in Fig. 7.1 and *LVC*, for the graph in Fig. 8.1. The structure of the impedance matrix for each of those circuits are also supplied, so when calling *solve* one supplies the impedance values of each component instead of the entire impedance matrix. Additionally, the classes *Primary* and *HVC* have a function *find_optimal_capacitance*, that returns the capacitance which gives a grid power factor of one.

To make it easier to add powers of several components, we use the following sign conventions in the implementation. For active power, a positive sign means that the component consumes power and a negative sign means that the component delivers

Algorithm 1 Numerical solver for a harmonic circuit problem.

Require: $\mathcal{A}, \mathcal{D}, \tilde{\mathbb{E}}, \tilde{\Psi}$
 $N \leftarrow$ number of rows in \mathcal{A}
 $E \leftarrow$ number of columns in \mathcal{A}
 $M \leftarrow N - \text{rank}(\mathcal{A})$
 $\mathcal{A}_T \leftarrow \mathcal{A}[0 : N - M, 0 : N - M]$
 $\mathcal{A}_C \leftarrow \mathcal{A}[0 : N - M, N - M :]$

$$\mathbf{U} \leftarrow \begin{bmatrix} -\mathcal{A}_T^{-1} \mathcal{A}_C \\ \mathcal{I}_{(E-N+M) \times (E-N+M)} \end{bmatrix}$$

$$\mathbf{A} \leftarrow \begin{bmatrix} \mathbf{U}^T \mathcal{D} \\ \mathcal{A}[0 : N - M] \end{bmatrix}$$

$$\mathbf{b} \leftarrow [\mathbf{U}^T \tilde{\mathbb{E}} \quad \tilde{\Psi}[0 : N - M]]^T$$

 $\tilde{\mathbb{I}} \leftarrow$ solution of $\mathbf{Ax} = \mathbf{b}$
 $\tilde{\mathbb{V}} \leftarrow$ least square solution of $\mathcal{A}^T \mathbf{x} = \tilde{\mathbb{E}} - \mathcal{D} \tilde{\mathbb{I}}$
return $\tilde{\mathbb{I}}, \tilde{\mathbb{V}}$

power. For reactive power, we use a positive sign for inductive components and a negative sign for capacitive components as per the definition. We have functions for both total and apparent power, where apparent power is the absolute value of total power, because we need to add total power and then find the absolute value when we want the apparent power of several components together.

All other code for this thesis uses the module described above to solve different variations of the circuit problems. We use the libraries Matplotlib [44] and Seaborn [45] to generate plots, and Pandas [46], [47] for data handling.

6.1 Validation

We first test the circuit solver on the classes *Primary* and *Secondary* by checking whether it agrees with the analytical solution. For the numerical solution, we want to use somewhat realistic parameter values. Table 6.1 shows the values chosen for the primary side. Voltage supply, angular frequency and capacitance are set to realistic values for a submerged arc furnace, and transformer resistance and reactance are chosen so that they give realistic power output. The conducting resistance is set to be very small, but non-zero. With these values, the generated active power in the transformers is 41.5 MW, the transformer power factor is 0.73 and the grid power factor is 0.83.

Table 6.2 shows the values chosen for the secondary side. The secondary side values are based on the latest version of the web metamodel [34]. Electrode impedances are read directly from the output and source voltages are $\sqrt{3}$ times the electrode voltages. We give the transformers an internal resistance of $2n\Omega$, chosen in accordance with the model from the metamodel. With these values, we see that the calculated peak electrode current with the numerical circuit model is 192.6 kA compared to 193.2 kA from the metamodel, which is 0.31 % smaller. However, the metamodel and numerical circuit

Table 6.1: The parameter values used for numerical solutions to the primary side circuit.

Parameter	Value
Voltage supply V_0	20 kV
Angular frequency ω	100π
Conductor resistance R	1 nΩ
Capacitance C	53 μF
Transformer resistance R_p	23.4 Ω
Transformer reactance X_p	21.6 Ω

Table 6.2: The parameter values used for numerical solutions to the secondary side circuit.

Parameter	Value
Voltage supply V_0	354 V
Angular frequency ω	100π
Electrode resistance R_e	681 μΩ
Electrode reactance X_e	812 μΩ
Voltage source resistance	2 nΩ

model work in fundamentally different ways, and to verify the numerical model we need to check it against analytical solutions.

We solve the *Primary* circuit class with the parameter values of Tab. 6.1 and insert the same values into the balanced analytical solution of the balanced primary side. For the currents in Eq. (5.9) and reactive powers of transformers and capacitors in Eqs. (5.11) and (5.12) we get relative errors of the order 10^{-16} or smaller, meaning the solutions are equal to machine precision. There is zero circulating current in the numerical solution both for the balanced case and when the capacitors are unbalanced, as it should be according to Eqs. (5.10) and (5.13).

We also check that the numerical and analytical solution gives the same circulating currents when the transformers are unbalanced. We calculate the circulating current for the case where the resistance and reactance of one transformer varies from 20 percent below to 20 percent above the other two. Figure 6.1 shows the result, with analytical solutions in Fig. 6.1a and numerical solutions in Fig 6.1b. There is no discernable difference, and calculations show that the largest absolute error is of order 10^{-13} .

We do the same kind of analysis of the secondary side, and here find the relative current error to be of the order 10^{-10} or smaller. The circulating current in the numerical model is zero both in the balanced case and when the electrodes are unbalanced, as it should be according to Eqs. (5.3) and (5.5). Figure 6.2 shows the circulating current as a function of varying one transformer resistance, in the model corresponding to the voltage source internal resistance, from 10 percent below to 10 percent above the two others. The analytical and numerical solutions agree, with a maximum absolute error of order 10^{-5} .

We conclude that the analytical and numerical solutions agree with each other, and our implementation of the solver is correct.

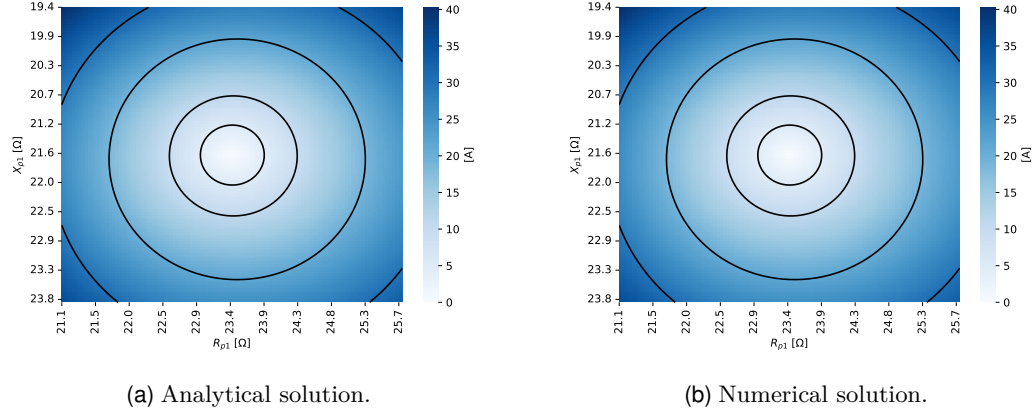


Figure 6.1: Primary side circulating currents for the case where one transformer has different resistance and reactance from the others.

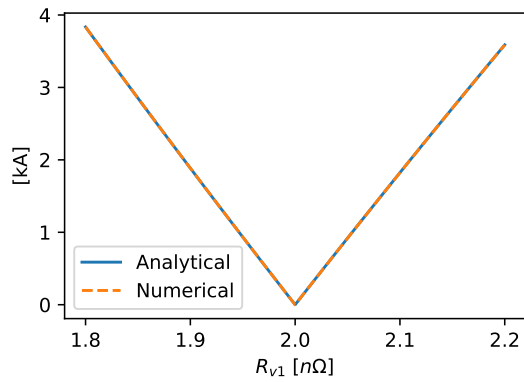


Figure 6.2: Secondary side circulating currents for the case where one voltage source has different resistance from the others.

Chapter 7

Full system

We are now ready to look at the whole system, supply and furnace together, using the circuit solver. A corresponding graph for the circuit in Fig. 4.2 is shown in Fig. 7.1, which the circuit class *HVC* is based on. When solving this system, we use the same values for voltage supply, angular frequency, capacitance, conductor resistance, and electrode impedance as when solving the primary and secondary sides separately. Deciding realistic parameter values for the transformer requires some deliberation.

7.1 Estimating transformer parameters

For the transformer we need self inductances for both the primary and secondary sides, mutual inductance, and the inductance and resistance representing the non-ideal conditions.

Starting with the self and mutual inductances, we use the formula

$$L = \frac{N^2 \mu_r \mu_0 A}{l}, \quad (7.1)$$

for self inductance L of a conducting coil wrapped around a core as a starting point [22]. Here N is the total number of windings, μ_r is the relative permeability of the core, μ_0 is the permeability constant, A is the cross-section area of the core and l is the core length. μ_0 is known, all the others are uncertain.

The relative permeability of a powder iron core typically ranges from 15 to 550 according to Hurley and Wölfle [22]. We arbitrarily choose a value in that range as our starting point, say $\mu_r = 120$. We further guess a cross-section area of $A = 10^{-2} \text{ m}^2$ and core length $l = 10 \text{ m}$. We know that the potential is about 10^4 V on the primary side and 10^2 on the secondary side, so we guess $N_p = 10^2 N_s$, where the subscripts p and s denote the primary and secondary sides, respectively. The absolute value is unknown, we make a guess at $N_s = 10^2$. With these values we get

$$\begin{aligned} L_p &= 15 \text{ H} \\ L_s &= 1.5 \text{ mH}. \end{aligned}$$

The mutual inductance is then given by Eq. (2.7).

We find reasonable values for the inductance L_t representing the magnetic leakage flux and the resistance R_t representing winding resistance by choosing values that give realistic output. Choosing $L_t = 0.1 \mu\text{H}$ and $R_t = 40 \mu\Omega$ gives results close to what can be expected from a furnace, namely a grid power factor of 0.74, an electrode current of

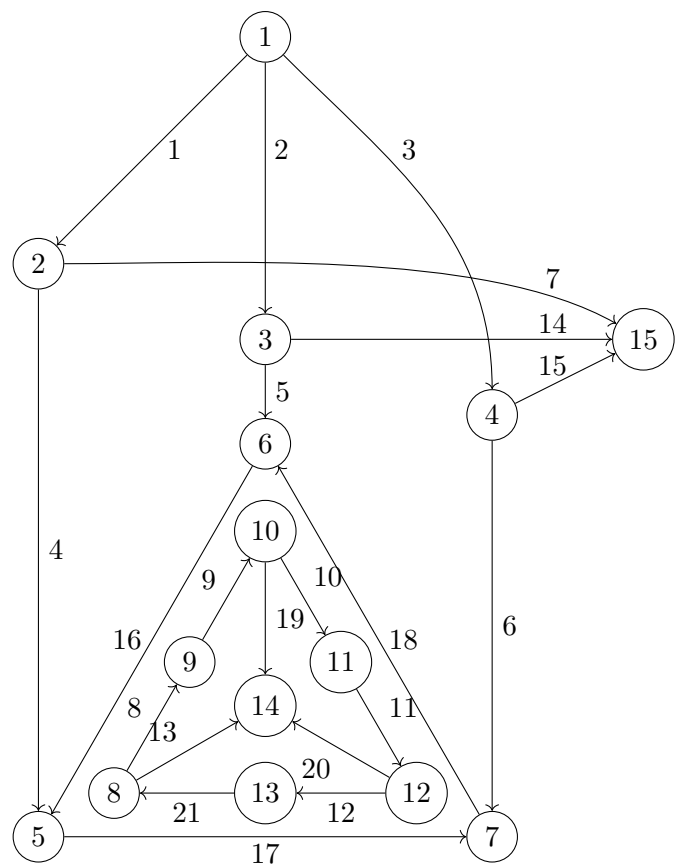


Figure 7.1: Directed graph of the full system.

Table 7.1: The parameter values used for numerical solutions to the full system.

Parameter	Value
Voltage supply V_0	20 kV
Angular frequency ω	100π
Conductor resistance R	1 nΩ
Capacitance C	53 μF
Primary side self inductance L_p	15 H
Secondary side self inductance L_s	1.5 mH
Magnetic leakage flux inductance L_t	0.1 μH
Winding resistance R_t	40 μΩ
Electrode resistance R_e	681 μΩ
Electrode reactance X_e	812 μΩ

186 kA, an active delivered power of 35 MW to the electrodes and a 2 percent loss of active power through the transformers due to resistance. We therefore use these values.

Note that all estimates found here are highly uncertain, and chosen ad hoc to best fit what we expect. While they seem to work well in that they give reasonable results for the furnace and supply, they could and should be updated if we get more information.

7.2 Comparison with separate models

We can now compare the numerical results of the full model with the separate models the primary and secondary sides. We should expect the two approaches to give similar results and show similar behaviour, and the comparison thus serves as a useful verification for the full model. The parameter values we use, some known and some estimated as described in the previous section, are listed in Tab. 7.1.

We start by comparing the currents and voltages as found by the full model and by the primary and secondary side models. The parameter values for the primary and secondary side models are chosen to correspond to the values in Tab. 7.1 as far as possible. Figure 7.2 shows the result for voltages. The full model and the two separate models give almost exactly the same results, with only secondary side transformer voltages having a slight deviation for the two models. It is just discernible in the plot, but secondary side transformer voltage has slightly different amplitudes and phase angles. All currents match perfectly.

The full numerical model also yields no circulating current when either the electrodes or the capacitors are unbalanced, in agreement with the secondary and primary side analytical solutions. When it comes to comparing circulating current effects due to unbalanced transformers, we need to take more care. Since the full circuit model includes non-ideal transformers, and changes on either the primary or secondary side affects the other side, there is no straightforward way of translating the transformer parameters into their corresponding values when viewing the primary or secondary side in isolation.

Figure 7.3 shows the circulating currents in the primary and secondary side deltas as the impedance of one transformer changes, calculated with both the full model and with the primary and secondary models. Figures 7.3a and 7.3b are calculated by varying the non-ideal elements of one transformer from 10 percent below to 10 percent above the other two. We see that this creates a circulating current with the same pattern on both sides, the only difference being that the secondary side circulating current is

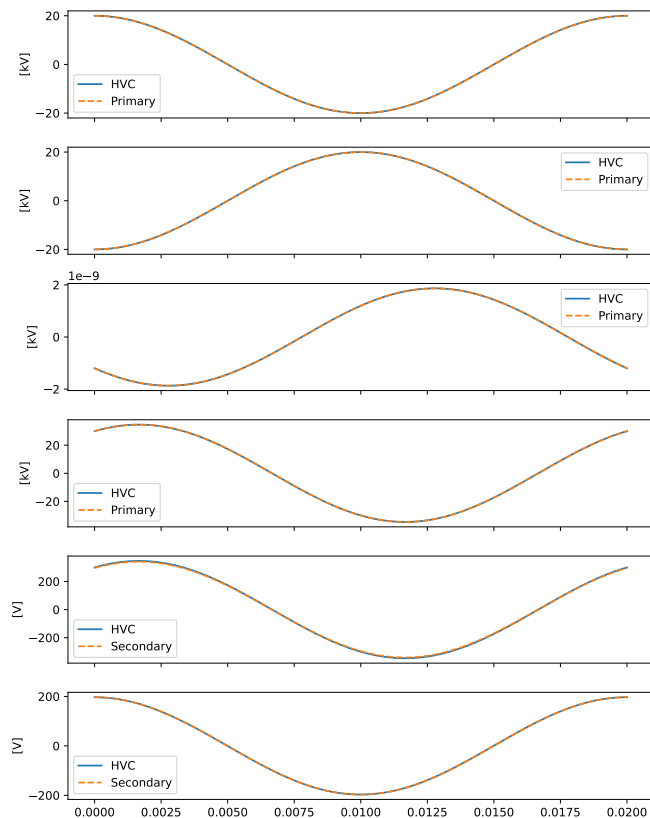


Figure 7.2: Time series of voltage drops covering one period, calculated both with the circuit model *HVC* and with the circuit model *Primary*. The values are from top to bottom grid supply, capacitors, conductors, primary side transformers, secondary side transformers, and electrodes.

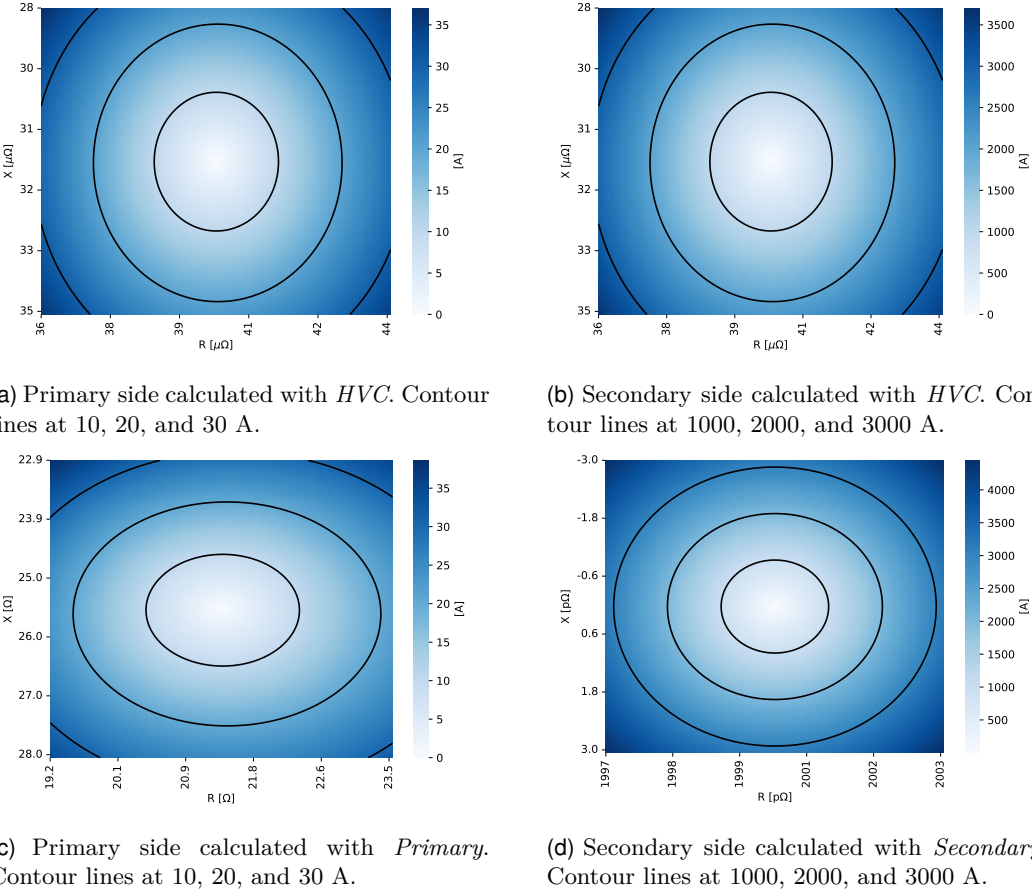


Figure 7.3: Circulating currents in primary and secondary side deltas when one transformer has different impedance from the others, calculated in different ways.

about 100 times bigger. Working with the primary side model, we vary the impedance elements representing one of the transformers up and down 10 percent. The result, in Fig. 7.3c, shows a significantly different behaviour from the one calculated with the full model in 7.3a, but they have about the same magnitude. This is probably because there is no linear relationship between the two sets of parameters, thus varying for example the reactance of the primary side model, is not the same as varying the internal loss inductance of the full model. For the secondary side, the model is much more sensitive to variance in the internal resistance or reactance of the voltage source. We here vary resistance and reactance up or down 0.15 percent of the internal resistance, and the result is seen in Fig. 7.3d. This gives circulating current of the same order of magnitude as in Fig. 7.3b, but again with a different pattern.

Figure 7.4 shows the power factor seen from the grid as a function of capacitance, calculated both with the full model and with the primary side model. The models give the exact same behaviour, having one peak where the power factor is one, approaching zero as the capacitance increases and approaching a limit value between zero and one when the capacitance approaches zero. This limit is the power factor one would have if there was no power factor correction.

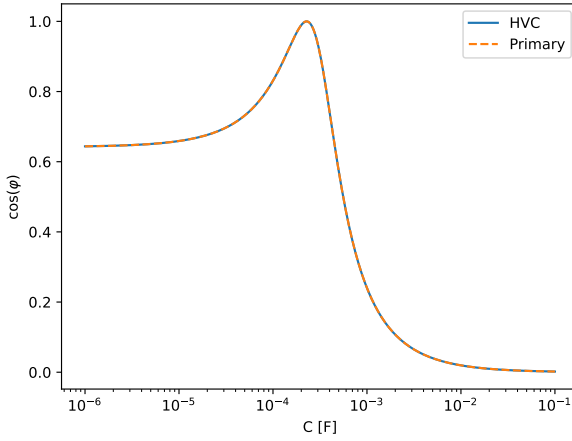


Figure 7.4: The power factor seen from the grid as a function of capacitance, calculated both with the circuit model *HVC* and the circuit model *Primary*.

7.3 Discussion

Given that we choose corresponding parameter values, the full circuit model and the separate primary and secondary side models yield the same currents and voltages, with secondary side transformer voltages being a small exception. That indicates that the transformer model we have chosen for the full model cannot be fully represented by a simple voltage source with internal resistance as we have done for the secondary side model. The models also show the same behaviour of grid power factor as a function of capacitance and existence of circulating currents in the same scenarios. But as changing the internal impedance of the transformer losses is not equivalent to changing the impedances on the primary or secondary side, we do not reproduce the exact same circulating current pattern, as seen in Fig. 7.3. We conclude that the models agree to the degree we could expect, and as we have confirmed that the analytical solutions agree with the primary and secondary side numerical models, the agreement between the full model and the separate numerical models serves as a good validation of the full model.

Having a fast, numerical model that combines the primary and secondary sides is useful since we can study how changes on one side affect the other side. Most modelling efforts to date focus on the secondary side, so the combined model can offer new insight and prove or disprove what has previously only been assumptions or intuition.

When it comes to parameter estimation for the full model, we are most uncertain about the transformer values, as we cannot measure them or, with the possible exception of windings ratio, set them to a specific value. We have also lumped the magnetic flux leakage and winding losses together on the secondary side, so we cannot distinguish between what happens internally on the primary and secondary sides of the transformers. This is a weakness of our modelling choice, but on the other hand it would only make sense not to lump them together if we had a reliable way of measuring the effects separately. However, even if our specific estimates and therefore the exact output values of our model are uncertain, we still capture the behaviour of the system.

We see in Fig. 7.4 that the power factor of the grid as a function of capacitance has one peak where it reaches one, and that the curve is the same whether one uses the primary or full numerical model. It is therefore possible to calculate this optimal capacitance using Eq. (5.14) that we found analytically for the primary side. For a real

7.3. Discussion

furnace supply system, R_p and L will be found from the impedance viewed from the primary side of the transformer. That is, we can measure the primary side current and voltage and use Eq. (2.10) for finding the impedance.

Chapter 8

Low-voltage compensation

With the framework we have in place, we can easily explore how the system behaves differently if we use low-voltage compensation instead of primary side capacitors. A graph corresponding to the LVC-circuit of Fig. 4.3 is shown in Fig. 8.1. We solve both this system and the system with primary side power factor correction for capacitor values in the range 10^{-5} F to 10^3 F. All other parameters are kept constant and equal between the two systems. Some results are depicted in Fig. 8.2, where we can see the behaviour of some quantities of interest as a function of capacitance.

The uppermost left subplot shows the power factor observed by the grid. Notably, with LVC there are two maxima where the power factor reaches 1, compared to a single maximum for the normal configuration. The right maximum, corresponding to the largest capacitance, results in several unwanted peaks. For example, a current drawn from the grid of almost 150 kA, delivered apparent power in the range of GVA for the transformer and a current of over 8 MA through the secondary side of transformer. We therefore consider the left maximum, corresponding to the lower capacitance, to be the realistic operating point.

The optimal capacitor values as found above are presented in the top row of Tab. 8.1. The table also lists values for all other quantities shown in Fig. 8.2 at this capacitance. We see that the optimal capacitance for low-voltage compensation is about 3400 times larger than the optimal capacitance for normal primary side setup.

From the uppermost right plot, we can see that the chosen maximum for low-voltage compensation is also optimal in the sense that it achieves a maximum power factor for the delivered power on the secondary side of the transformer. The power factor here is close to 1, but slightly below as the transformer is non-ideal. Choosing the other maximum would have given a terribly low power factor for the transformer. The transformer power factor is constant at 0.6430 with the normal setup, a good deal below the best we achieve with low-voltage compensation.

Plots of the delivered active and apparent power from the transformer, as seen in the second row, show that for the optimal capacitance in LVC there is a minimum for the apparent power without a dip in active power. This is possible due to the maxima in power factor. Both active and apparent power in the transformer is constant for the normal setup.

In the middle row, we see the current from the grid and through the secondary side of the transformer. The grid current changes as a function of capacitance for both setups, and both setups achieve a minimum for the optimal capacitance, where the grid power factor is 1. The current on the secondary side of the transformer is constant for the normal setup, but varies for the low-voltage compensation. Again, we have a minimum

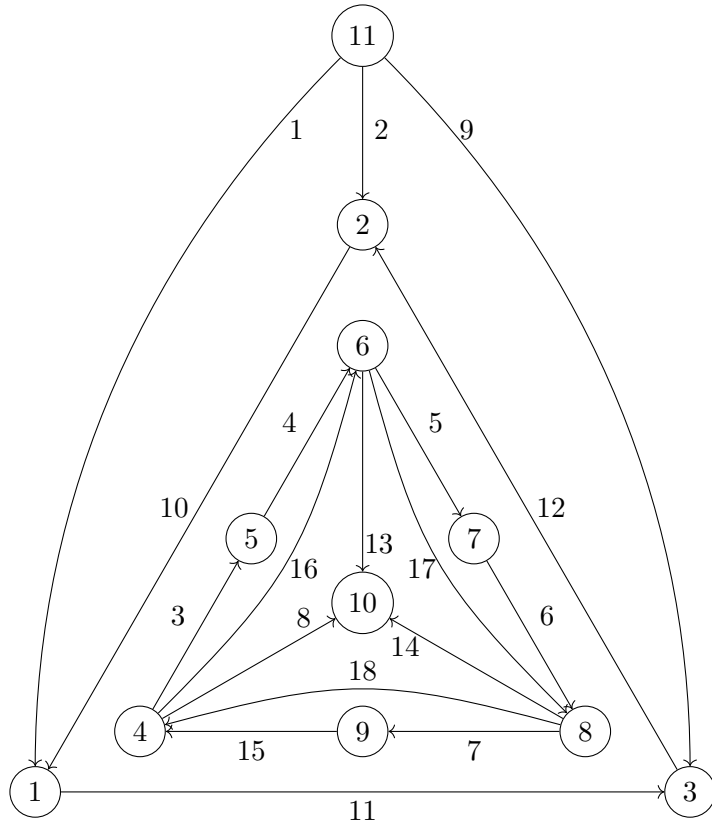


Figure 8.1: Directed graph of the full system circuit with low-voltage compensation.

Table 8.1: Optimal capacitance and other circuit values at this optimal capacitance, for both high-voltage and low-voltage compensation. All transformer values are given for the secondary side.

	High-voltage compensation	Low-voltage compensation
Capacitance (mF)	0.2279	777.8
Transformer power factor	0.6430	0.9999
Transformer active power (MW)	11.76	11.94
Transformer apparent power (MVA)	18.30	11.95
Grid current (kA)	1.199	1.204
Transformer current (kA)	107.3	69.52
Electrode current (kA)	185.8	187.2
Electrode power (MW)	11.76	11.94
Capacitor current (kA)	1.432	83.98
Capacitor voltage (kV)	20.00	0.3437

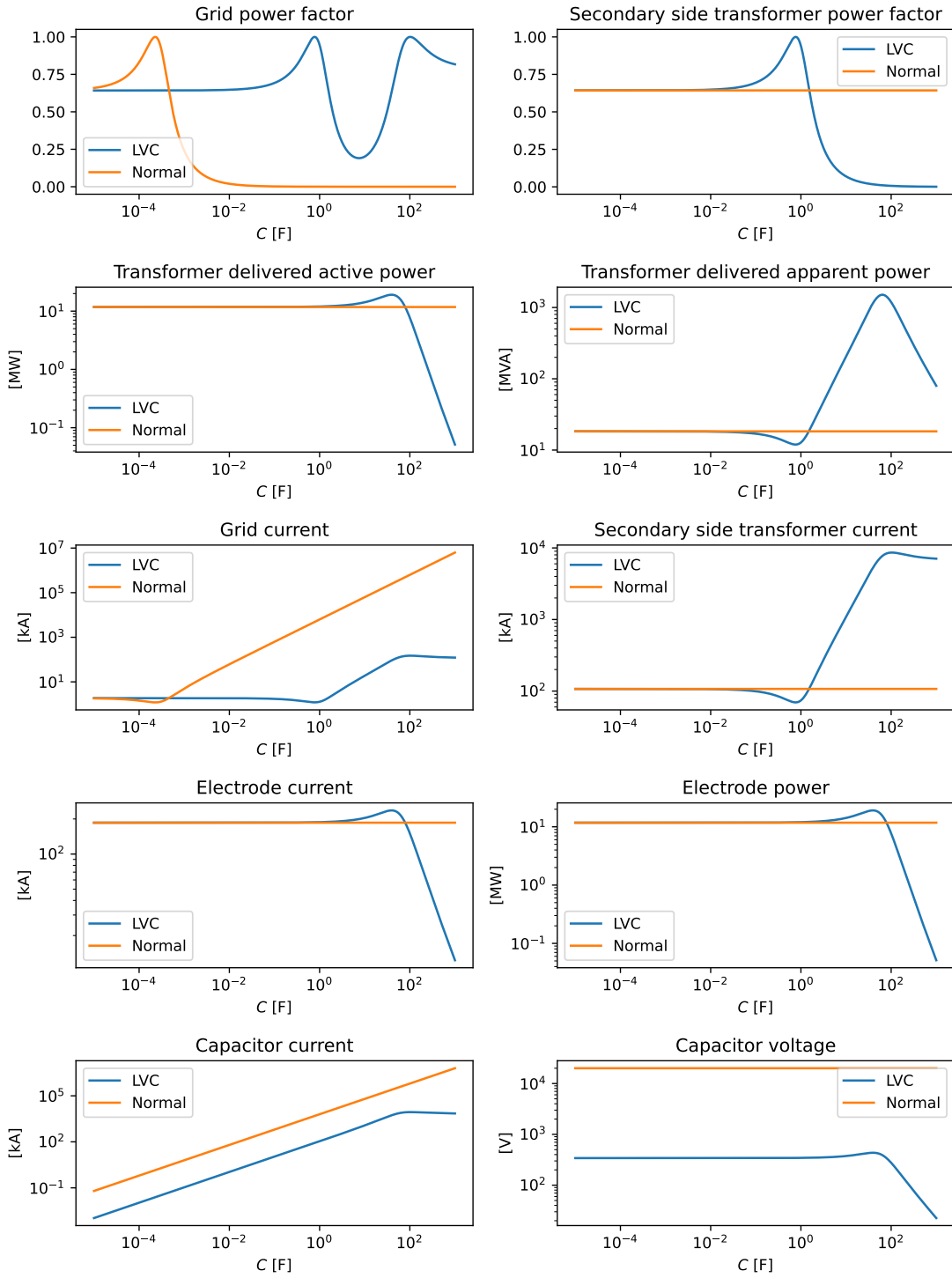


Figure 8.2: Behaviour of some power factors, powers, currents and voltages in different parts of the system as a function of capacitance, for both low-voltage compensation and high-voltage compensation.

Table 8.2: Slope and intercept of a first-order linear regression done on logarithmic data of transformer winding ratio versus ratio of LVC values to HVC values for several quantities.

	Slope	Intercept
Optimal capacitance ratio	2.002	-1.084
Capacitor current ratio	1.002	-0.5430
Capacitor voltage ratio	-0.9999	0.5407

for the optimal capacitance, where the power factor reaches a maximum in both the grid and the transformer.

The second to last row shows the current and power in an electrode. The peaks for an LVC setup are unrealistic, as they correspond to the rightmost grid power factor maximum. But even at the other maximum, the current and power are slightly larger for the LVC setup than for the normal setup, as can be seen in Tab. 8.1.

Lastly, the two bottom plots show that the capacitors will be subject to currents and voltages of varying magnitude, depending both on the setup used and on the capacitance. The currents and voltages that the capacitors will be subject to when the capacitance is chosen to get a grid power factor of 1, are presented in the last rows of Tab. 8.1. A capacitor in an LVC setup will at this optimal point experience currents that are almost two orders of magnitude larger and voltages that are roughly two orders of magnitude smaller than a capacitor at the optimal point for the normal setup. It is also worth noting that within the interesting range of capacitor values, that is below the peaks corresponding to the rightmost peak of grid power factor, the current increases with increasing capacitance and the voltage is almost constant.

Suppose $y \propto x^a$. Then $\ln y \propto a \ln x$, or to be more precise

$$y = bx^a \implies \ln y = a \ln x + \ln b. \quad (8.1)$$

In other words, a loglog plot of y vs x should result in a straight line with slope a and intercept $\ln b$. We use this to investigate the proportionality factor between different quantities.

This has been done for the ratio of optimal capacitor value, the current through the capacitor at this value and the voltage over the capacitor. Figure 8.3 shows loglog plots of the ratios, together with the fitted linear line. From the graph, it looks like the points closely follow the linear line, indicating that there is a polynomial relationship between the quantities. Table 8.2 show the slopes and intercepts of the linear fit. We see that optimal capacitance has a slope close to 2 and current and voltage has a slope close to plus and minus 1, respectively. This means that there is a quadratic relationship between windings ratio and ratio of optimal capacitance, a linear relationship between windings ratio and ratio of current through the capacitor, and an inverse linear relationship between windings ratio and ratio of voltage over the capacitor.

8.1 Discussion

Our results on low-voltage compensation show that it can indeed improve the power factor of the transformer, as reported by Li *et al.* [31]. Connected to this, we see a minimum for apparent power without a decrease in active power for the optimal capacitance. This means that with LVC we can deliver the same power with a smaller load on the transformer, meaning we can use a smaller transformer. A minimum for the

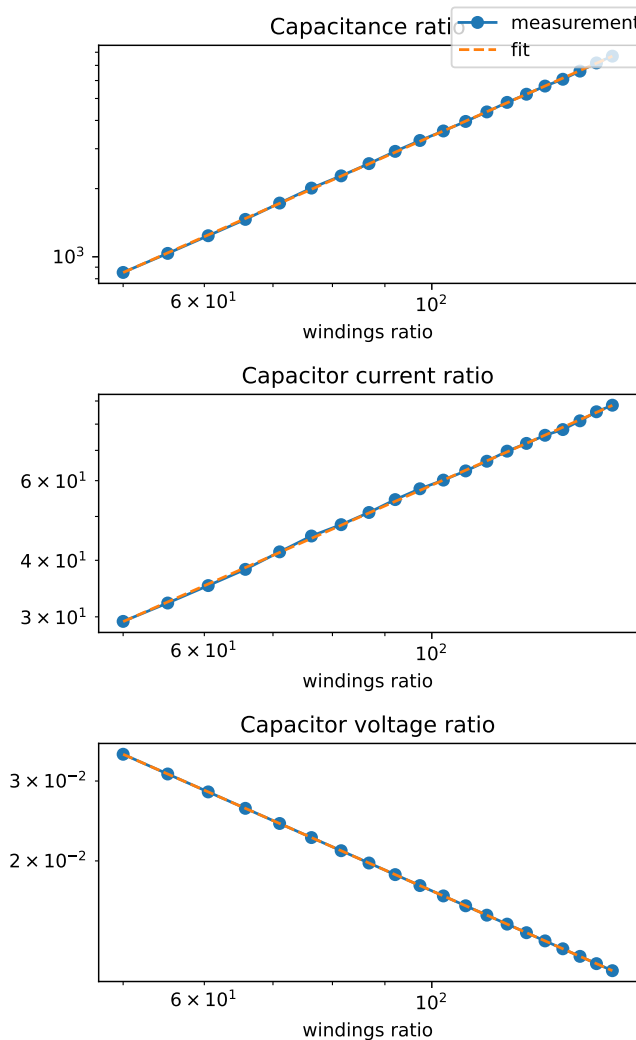


Figure 8.3: LVC to HVC ratio of optimal capacitance, capacitor current and capacitor voltage as a function of transformer windings ratio. The axes are logarithmic.

current at this optimal point also means that we reduce the losses in the transformers and bus bars of the secondary side.

However, there are also disadvantages to LVC when compared to HVC. The capacitors are placed in a more critical area when on the secondary side, and the LVC arrangement could also complicate current measurements in the electrodes, as it would no longer be possible to calculate electrode currents directly from secondary side transformer currents.

If operating with low-voltage compensation, one can use Eq. (5.14) to find the optimal capacitance for HVC and the relationship in Eq. (8.1) together with the windings ratio and the slope and intercept of Tab. 8.2 to find the optimal capacitance for LVC. The same approach can also be used to find out how much current and voltage the capacitors will be subjected to when placed on the secondary side and when the windings ratio change. Note however that all the above calculations are based on a balanced system. We have not studied how much variation is introduced if the system becomes unbalanced, as all real systems are.

It is not within the scope of this thesis to answer whether LVC or the traditional HVC is the best method, but calculated estimates like the ones provided by our circuit models might help experts in the decision.

Chapter 9

Metamodel simulations

The circuit model as it is implemented is static. However, given a time series of inputs we can solve the circuit model successively with the input for each time step and create time series of outputs that way. We will do such simulations with the assumption of constant voltage from the grid and constant capacitor and transformer values. The changes come from changes in metallurgical conditions, manifesting in the form of changes in electrode impedance in the circuit model. We will use the ferromanganese metamodel [33], [34] described in Sect. 4.3 to generate time series of electrode impedances according to different scenarios. This way we can study electrical conditions not available with the metamodel, notably primary side conditions.

We begin by simulating a furnace running with resistance control as described in Sec. 4.4. We implement the control algorithm in the metamodel code, allowing time simulations to run with this control strategy. Then we simulate 48 hours of operation from a random but realistic starting point, with one minute time resolution. The electrode impedance given as output from this metamodel simulation is then used as input for the circuit model, allowing us to study the electrical conditions on both the primary and secondary sides during these 48 hours, as well as the workings of the control algorithm itself.

Figure 9.1 shows the movement of the clamp holders and the resistance of the electrodes during operation, Fig 9.1a shows the entire 48 hours of the simulation and Fig. 9.1b is zoomed in on the first five hours. The clamp positions often make minor adjustments, and sometimes move in one direction for a longer period of time. The electrodes resistances are mostly kept within their deadband. We see that the times the resistances move significantly outside their deadband is when the clamp holders are already at maximum or minimum height, and therefore cannot move further to bring the resistances inside again.

9.1 Interaction effect

As stated by Barker *et al.* [36], the resistance controller should in theory not have an interaction effect, as changing the height of one electrode does not affect the resistance of the other two electrodes. We do however observe interaction with the resistance controller implemented in the metamodel. Figure 9.2 shows one example where the interaction becomes apparent. We start with all three electrodes having the same clamp position of 0.2 m and symmetrical conditions. Then electrode 1 and 2 are moved in sync in steps of 0.05 m and the third electrode is kept stationary, and we calculate

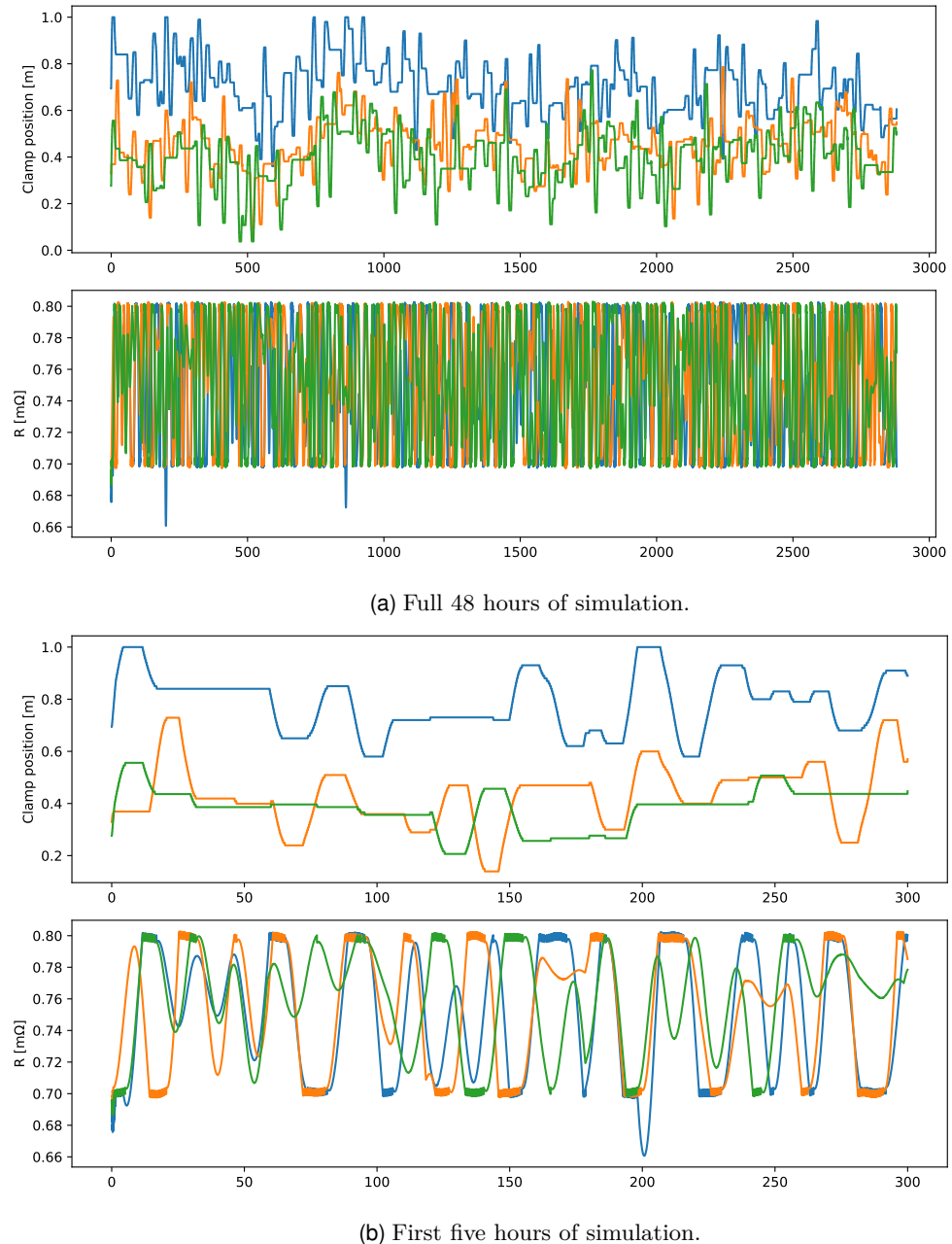


Figure 9.1: Clamp positions and electrode resistances from a ferromanganese metamodel simulation of operation with resistance control. The resistance dead-zone is $0.75 \text{ m}\Omega \pm 0.05 \text{ m}\Omega$ and the clamp positions are limited to between 0 and 1. [hide dead-zone values?](#)

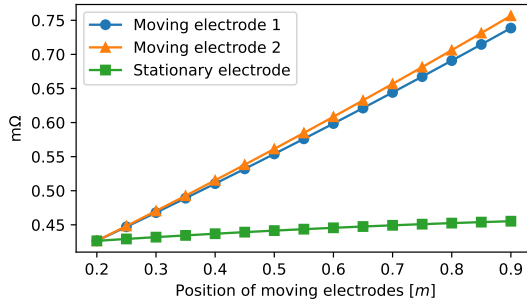


Figure 9.2: An example of the interaction effect on resistance. We move two electrodes in sync and keep the third electrode stationary. If there was no interaction the resistance of the stationary electrode would be constant.

Table 9.1: The slope of the lines in Fig. 9.2, where we move two electrodes in sync and observe the change in resistance for all three electrodes.

	Slope [mΩ/m]
Moving electrode 1	0.446
Moving electrode 2	0.472
Stationary electrode	0.0412

the resulting resistances. An increased clamp position means that the electrode tip is physically lifted further up in the furnace.

We see that the resistance of the stationary electrode changes when the positions of the other two change, albeit much less than the resistance of the other two. Note that the resistance of the two moving electrodes differ as well, with electrode 2 having a slightly larger increase in resistance than electrode 1. The slope of each electrode is presented in Tab. 9.1. The stationary electrode has a slope that is 9.2 percent and 8.7 percent that of electrode 1 and 2, respectively. Electrode 1 has a slope that is 94 percent that of electrode 2.

Figure 9.3 shows how the zero sequence component of the electrode voltages changes in this scenario, plotted in the complex plane and with the phase angles of the three electrode voltages marked as well. The innermost point of v_0 is the balanced case, and the absolute value increases as the two electrodes are moved up. The phase angle of the v_0 component is somewhere in between the phase angles of the two moving electrodes, skewed towards the moving electrode with the highest resistance.

9.2 Discussion

From Fig. 9.1a it seems like the electrode clamp positions more seldom reach their maximum or minimum positions. Clamp positions that do not reach their limit values are highly desirable, as in turn results in fewer deviations from the resistance dead-zone. We cannot however conclude after one random simulation run. Further research would be needed, looking at more runs with different starting positions, longer time periods and so on.

We must also be careful about inferring too much from the behaviour of the control simulation in general. This is because the metallurgical effects in the furnace are modelled as random noise in the metamodel. The metamodel simulation therefore does

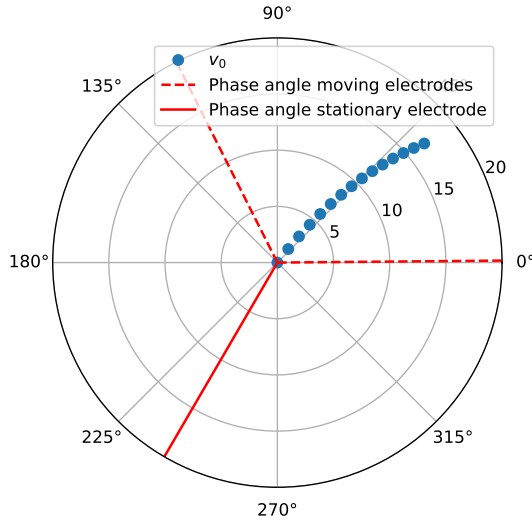


Figure 9.3: The zero sequence component v_0 of the electrode voltages from the interaction example plotted in the complex plane. The dot in the origin corresponds to the balanced case where $v_0 = 0$, and v_0 moves further away from the origin as the two moving electrodes get further away from the stationary electrode. The phase angles of the three electrode voltages are marked with red lines.

not capture the effect of the electrical conditions on the metallurgical conditions. The link between the control and upstream electrical behaviour is thus probably the most reliable and valuable output from the metamodel simulation coupled with the circuit model.

9.2.1 Interaction effect

As seen in Sec. 9.1, there is resistance interaction in the metamodel even if there theoretically should not be. In our example scenario the resistance change in the stationary electrode is slightly below 10 percent the change in the two moving electrodes, and the resistance in the moving electrodes do not change by exactly the same amount. If the model were non-interacting, the stationary electrode would have constant resistance and the two moving electrodes would have exactly the same resistance. Although no efforts have been made at this point to quantify the interaction effect more generally, the example shows that the effect can be large enough to warrant consideration. The resistance of the stationary electrode changes about $0.03 \text{ m}\Omega$ in total, and given that the width of our dead-zone is $0.1 \text{ m}\Omega$, this change represents a realistic possibility of moving the electrode resistance outside of the dead-zone.

One possible explanation for the interaction effect is that it is an artefact of the metamodel. It could be that the metamodel, due to some statistical error, has introduced the resistance interaction even though it is an unphysical element.

There is however a plausible physical interpretation. The resistance is calculated based on current and voltage measurements. As explained earlier, the current measurement is straightforward and the voltage measurement, done with the Bøckman technique, is more complicated. The voltage measurement is done with an attachment point at the furnace bottom, thought to be the neutral point or point defined to have zero potential. But as the furnace has a three-dimensional and changing electrical field, the

“true” neutral might not be at the measure point. It might on the contrary move around as the furnace geometry changes, for example when electrodes move. This then affects the resistance as we calculate it, and could result in an observed change in electrode resistance, even if the physical resistance in the electrode does not change.

We interpret the zero sequence component v_0 , plotted in Fig. 9.3, as the deviation from the true neutral. As we would subtract v_0 from the electrode voltages to get the true neutral, this means that the true neutral moves further away from the stationary electrode and closer to the moving electrodes when they are lifted higher up in the furnace.

No effort has been made at this point to develop an interaction-free resistance control algorithm, but we here present a suggested route. As seen in Fig. 9.3 and later in Fig. 10.4, there is a significant and changing zero sequence for the symmetrical components of electrode voltage. We interpret v_0 as an expression of the deviation from the true neutral. That way, we can find the voltage as it would be measured from the true neutral by subtracting v_0 from the real measurements. Our suggestion is that using this corrected voltage to calculate electrode resistance might get rid of the interaction effect, but this would need to be properly tested. For the metamodel, this would probably look like training the model on a dataset where the underlying physical model has been corrected for the true neutral.

Chapter 10

Measurement comparison

We lastly compare the circuit model to measurement data from a ferromanganese submerged arc furnace in operation. We have two measurement sets from the same furnace taken several weeks apart. The first set has data for 3.75 minutes and the second for 20 minutes. To protect industry secrets, all measurement data presented will either be scaled or plotted without labels on the y-axis.

For each instance there are two kinds of data. The first is what we will call process data, which contain measurements with one second resolution of voltage supply, r.m.s. electrode voltages, r.m.s. electrode currents, electrode power factors, electrode resistances, total active power and total reactive power. These measurements are fairly standard. The other kind of data is high-resolution measurement data, from now on simply referred to as measurement data. It contains instantaneous values for electrode voltages measured with the Böckman technique and currents and voltages of the secondary side transformers measured with Rogowski spoles. The sample frequency of these data are 10 kHz, meaning that we have 200 measurements per period when the angular frequency is 100π .

10.1 Data preprocessing

The high-resolution measurement data has been cleaned before we received them, so we know beforehand that there is no missing data, but we still need to do some processing before we can compare them to process data and the circuit model. Namely, we need to extract phases and amplitudes from instantaneous measurements, find and apply scaling factors and choose between sets of overlapping measurements.

10.1.1 Phase and amplitude estimation

We want to extract time series of phases and r.m.s. values from the instantaneous signals. For this we use the Fourier transform, specifically a discrete Fourier transform (DFT) algorithm from SciPy [48]. For more details on the Fourier transform, see Appendix C. Given a time signal $f(t)$, we denote the complex valued Fourier transform by $\mathcal{F}(\omega)$, where ω are the discrete angular frequencies of the DFT. For each ω we find the amplitude of this frequency by

$$A = |\mathcal{F}(\omega)| \quad (10.1)$$

and the phase angle by

$$\phi = \arctan \left(\frac{\text{Im}(\mathcal{F}(\omega))}{\text{Re}(\mathcal{F}(\omega))} \right), \quad (10.2)$$

being careful to choose the angle in the correct quadrant. We assume that our signal, when seen over a short period of time, consists of one, albeit more or less noisy, sinusoidal. Therefore we should have one dominant angular frequency, that is one frequency for which the amplitude is much higher than for all the rest. Denote this angular frequency ω_{\max} . The amplitude and phase we are looking for are then found by Eqs. (10.1) and (10.2) evaluated at ω_{\max} .

As we want to compare the high-resolution measurement data with measurements with one second resolution, we divide the whole time series of measurements into one second long sections and do the Fourier transform on each section. This gives us phase and amplitude time series with one second resolution.

10.1.2 Scaling

The high-resolution measurements need scaling in one form or another. Most scaling factors are provided by the furnace company, but we still need to scale the Rogowski coil currents and the directly measured transformer voltages.

We have two kinds of measurements for the transformer voltages. The first is a direct measurements, the second is to calculate the transformer voltages from the electrode Bøckman voltages. As the direct measurements have an unknown scaling factor, we use the Bøckman voltage calculations to scale them. Therefore, the secondary transformer voltages are scaled so that the r.m.s. voltage time series of each transformer has same mean as the voltage time series calculated from Bøckman voltages.

Rogowski coil measurements of transformer current are scaled such that the calculated electrode currents fit the electrode currents from process data. This turns out to be the same as scaling the Rogowski measurements to fit the transformer currents calculated by the circuit model with process data impedance as input. This scaling factor is thought to be a geometric factor, and should therefore be constant across datasets. Choosing the factors that make a few minutes of measurements fit best might therefore lead to overfitting. Therefore, we choose the scaling factors that seem to be the best compromise between the two sets of measurements. The approximate range of scaling factors is from 0.7 to 1.2.

10.1.3 Choosing which measurements to use

For the Rogowski coils, there are two sets of three coils, meaning there are two coils at each transformer that should measure the same current. They are called A1, A2, B1, B2, C1, and C2. We see however that the two options for each transformer follow the same trends, but have differing scales and phases. The somewhat differing scale does not matter, as the measurements need to be scaled to fit process data anyway. C1 is broken. That leaves the combinations A1 B1 C2, A1 B2 C2, A2 B1 C2, and A2 B2 C2. Looking at relative phase differences, we see that only the combination A2, B2, C2 gives the correct relative phases, approximately 120 degrees separate. We therefore proceed with this combination.

10.2 Data exploration

One advantage of high-resolution measurements is that we can view how the current and voltage varies within each period, not just how the r.m.s. value varies over time. Figure 10.1 shows the two first periods of the current in electrode 1, voltage in electrode 1 and voltage in transformer A as calculated from the voltages in electrode 1 and 2,

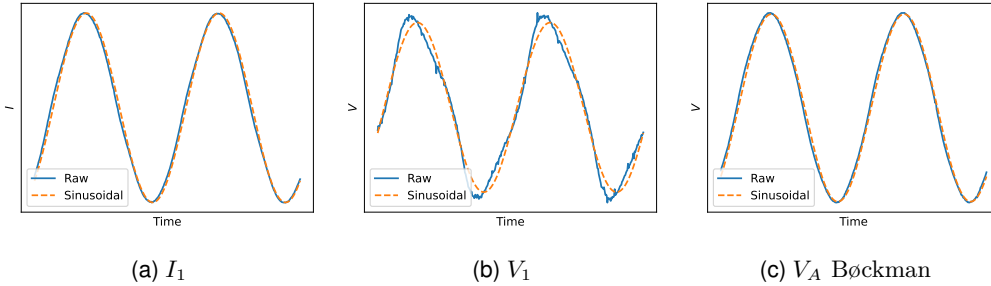


Figure 10.1: Time series of two periods of high-resolution measurement data for current in electrode 1, voltage over electrode 1, and voltage over transformer A.

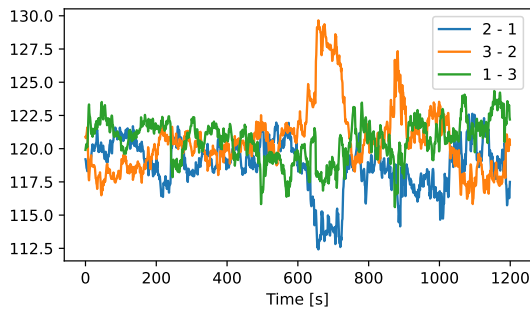


Figure 10.2: Phase differences between the three electrode currents. The phases are extracted from high-resolution measurement data.

both as measured raw data and as a pure sinusoidal with the r.m.s. value and phase found as described in Sec. 10.1.1. The current in electrode 1, see Fig. 10.1a, is close to a perfect sinusoidal. The electrode voltage however, as seen in Fig. 10.1b, is clearly not sinusoidal, although it has regular oscillations. Interestingly, the voltage over transformer A, calculated as $V_1 - V_2$ and shown in Fig. 10.1c, is close to a perfect sinusoidal even though V_1 and V_2 are not. All other quantities except the electrode voltages are close to perfect sinusoids, and we see that our method of extracting phase and amplitudes give sinusoids that line up well with the true signal.

As we can extract phases from high-resolution measurements, we can also look at phase shifts between different parts of the furnace. For example, Fig. 10.2 shows the phase differences between the electrode currents. We see that the phase difference varies around 120° , deviating as far as up to 130° or down to 112° at most during the 20 minutes depicted.

Plots of imbalance calculated as in Eq. (2.29) are shown in Fig. 10.3. The imbalance of the electrode voltage ranges from 0 to 2.5 percent and the imbalance of the transformer voltage ranges from 0 to 1.2 percent. The imbalance of the currents in the electrodes and in the transformers are equal, and higher than the voltage imbalances. It stays between 0 and at most just over 10 percent.

Looking at the absolute values of the zero sequence of symmetrical components also yields interesting information. We remember that the v_0 component defined as

$$v_0 = \frac{1}{3} (v_a + v_b + v_c)$$

is the constant part of the three phasors v_a , v_b , and v_c . For the secondary side transformers, this corresponds to the definition of circulating current given in Eq.

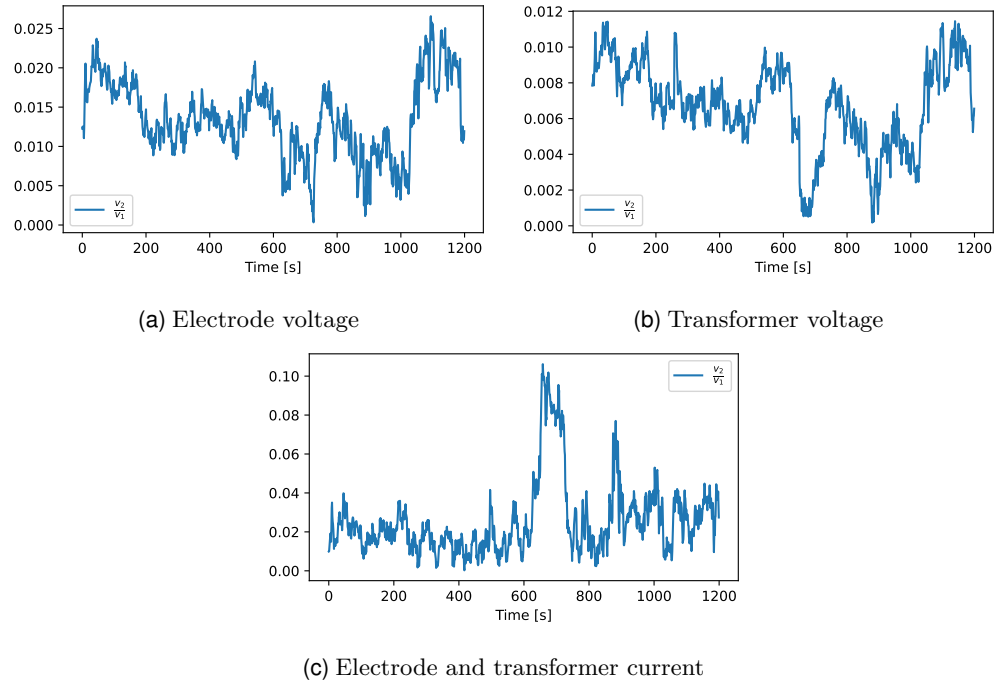


Figure 10.3: Imbalance in high-resolution measurement data, calculated from symmetrical components.

4.1. According to the analytical solutions in Sec. 5.1, there should only be a non-zero circulating current on the secondary side delta if the transformers are unbalanced, and specifically unbalanced electrodes do not lead to a circulating current. For the measurement data we know that the electrodes are unbalanced, and assume that the voltage supply and transformers are balanced. We find however that for the measurement data transformer currents v_0 is non-zero, with a constant value roughly 4 percent that of v_1 . For the electrode currents $v_0 = 0$.

There is also small non-zero zero sequence for the secondary side transformer voltages, with a constant value roughly 0.5 percent that of v_1 . And lastly, Fig. 10.4 shows the symmetrical components of the electrode voltages. We see that there is a non-zero, varying v_0 component of considerable size, meaning the electrode voltages have a common part that changes over time. The v_0 component is plotted in the complex plane in Fig. 10.5, with the phase angles of the electrode voltages drawn as well. We see that the v_0 phase varies, reaching all angles during the 20 minutes. The absolute value varies as well, with a few notable periods where it is farther from zero.

10.3 Comparison

With the preprocessing done as described above, the high-resolution measurement data and the process data line up well. This can be seen in Fig. 10.6, where we have plotted the r.m.s. values obtained from one set of high-resolution measurement data and process data together, for current, voltage and power factor of each electrode. Currents and voltages are scaled to stay between 0 and 1, with all currents having the same scaling and all voltages having the same scaling. Both the trends and the absolute values match for electrode voltage and electrode power factor. The trends also match well for electrode

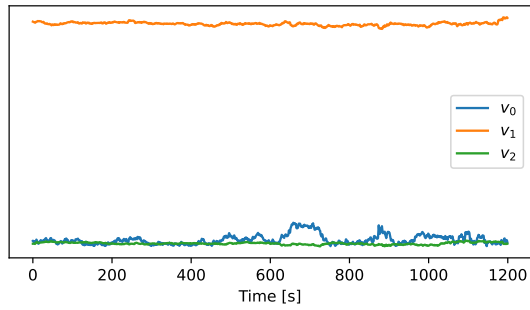


Figure 10.4: The symmetrical components of high-resolution electrode voltage measurements. The y axis is linear and starts at 0.

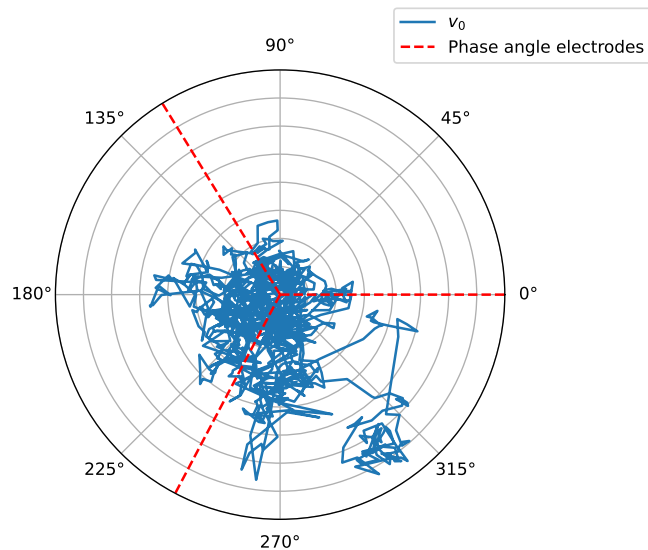


Figure 10.5: The zero sequence component v_0 of electrode voltage from 20 minutes of high-resolution measurement data plotted in the complex plane. The phase angles of the three electrode voltages are marked with red lines. The radial axis is linear.

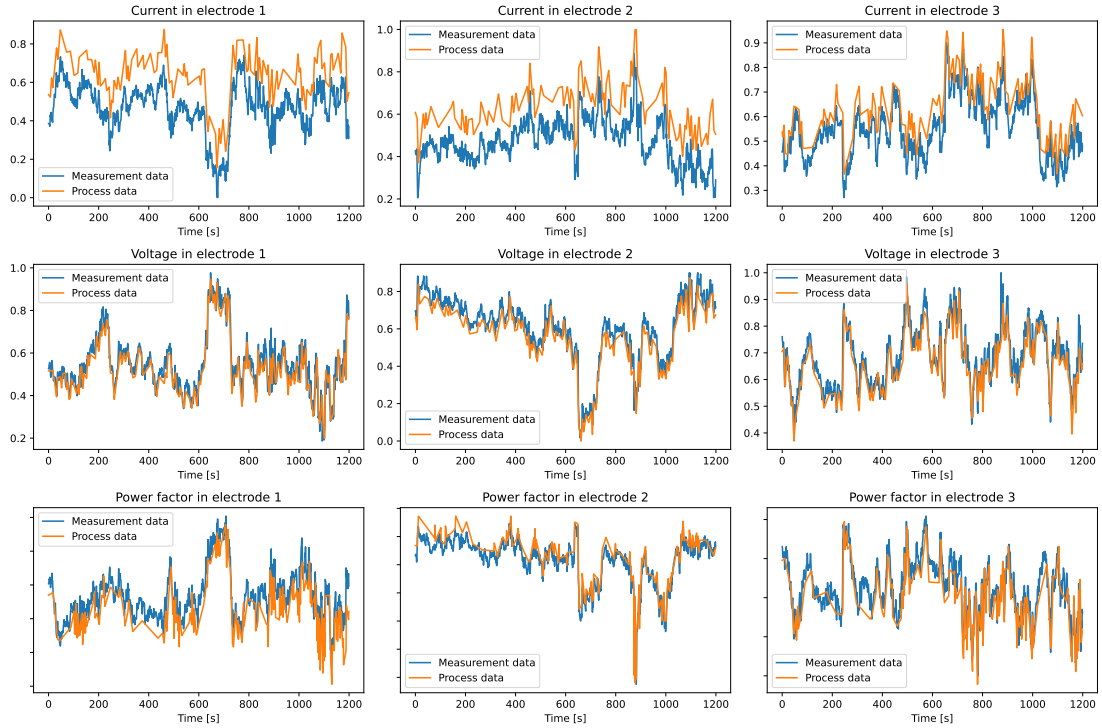


Figure 10.6: Comparison of r.m.s. values from process data and r.m.s. values calculated from high-resolution measurement data. Currents and voltages are scaled to lie between 0 and 1, and the y axis of the power factor plots is linear.

currents as seen in the first row, but with a slight difference in absolute value. This is because the scaling factor for currents is not chosen to fit this dataset perfectly, but is a compromise between this dataset and the other one.

Next we compare the high-resolution measurement data with the circuit model. We solve the circuit model with the electrode resistances from process data and with electrode reactance calculated from resistance and power factor in process data. The result is shown in Fig. 10.7, where we have plotted currents, voltages and power factor for both electrodes and secondary side transformers. Currents and voltages are scaled to between 0 and 1, with all currents having the same scaling and all voltages having the same scaling. Given the two measurements of transformer voltage, direct and calculated based on Böckman measurements, there are two different measurements for secondary side transformer voltage and power factor.

The circuit model match the pattern of the measurement data very well for all quantities except secondary side transformer voltage in the second to last row. The phase of the voltage seems to be accurate however, given the good match of the power factor pattern in the last row. Electrode voltages and power factors and secondary side transformer power factor calculated from Böckman additionally have good match in absolute value. The currents differ more in absolute value, both for the electrodes and the transformers. Especially the currents in electrode 1 and in transformer A differ.

Table 10.1 shows the r.m.s. errors of the circuit model compared to the high-measurement data after we have applied scaling to currents and voltages. That is, the error is calculated as

$$\frac{1}{n} \sqrt{\sum_{i=1}^n (x_i - y_i)^2} \quad (10.3)$$

10.3. Comparison

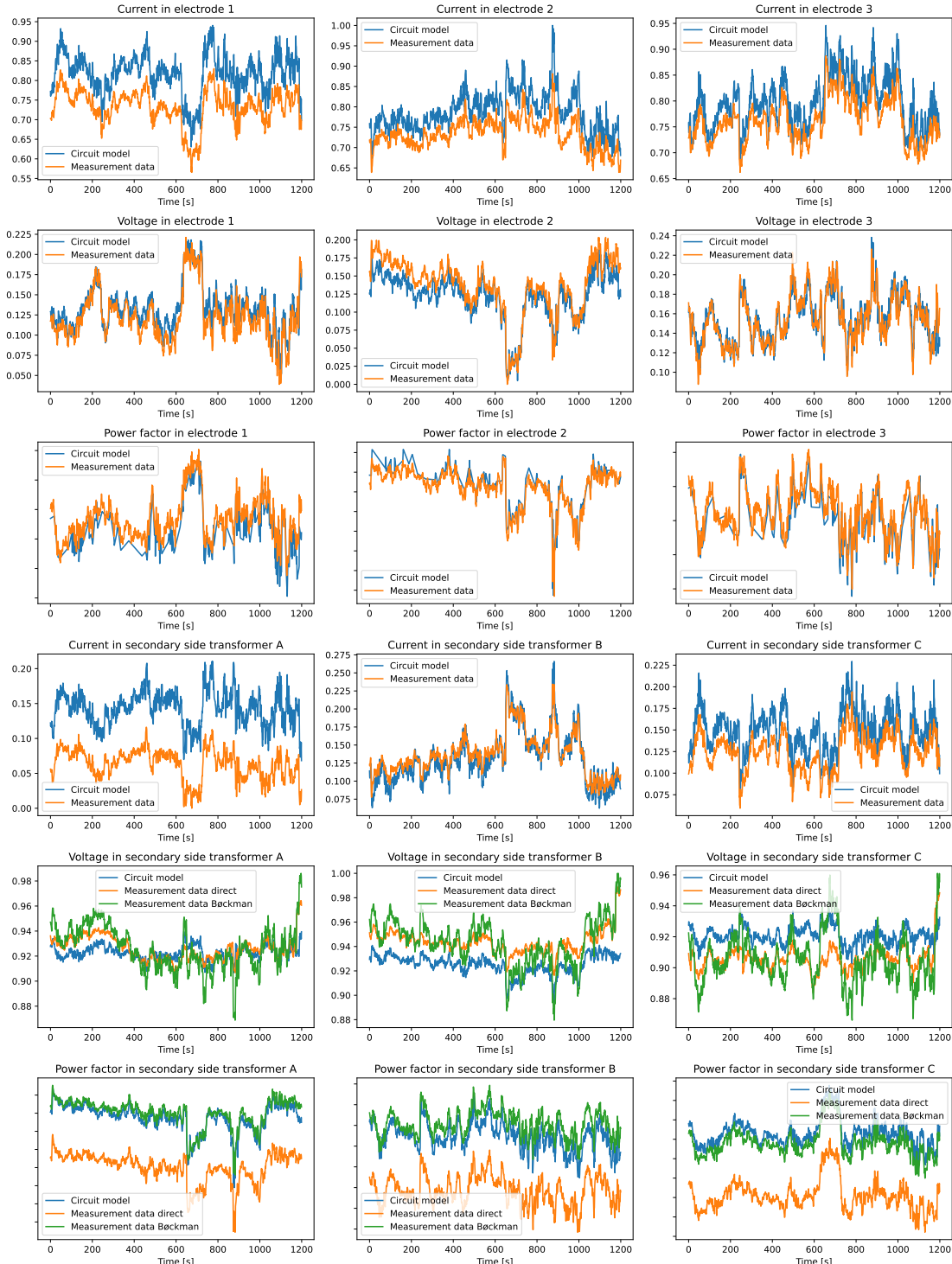


Figure 10.7: Comparison of r.m.s. values from the full equivalent circuit model *HVC* and r.m.s. values from high-resolution measurement data. Currents and voltages are scaled to lie between 0 and 1, and the y axis of the power factor plots is linear.

Table 10.1: R.m.s. error of values calculated with the full circuit model compared to high-resolution measurement data. All currents and voltages have been scaled to lie between 0 and 1 before calculating the error.

Quantity	Relative error
I_1	$2.486 \cdot 10^{-3}$
I_2	$1.641 \cdot 10^{-3}$
I_3	$1.171 \cdot 10^{-3}$
V_1	$4.258 \cdot 10^{-4}$
V_2	$5.312 \cdot 10^{-4}$
V_3	$2.871 \cdot 10^{-4}$
$\cos \phi_1$	$2.947 \cdot 10^{-4}$
$\cos \phi_2$	$2.336 \cdot 10^{-4}$
$\cos \phi_3$	$2.169 \cdot 10^{-4}$
I_A	$2.330 \cdot 10^{-3}$
I_B	$3.555 \cdot 10^{-4}$
I_C	$7.758 \cdot 10^{-4}$
V_A	$2.515 \cdot 10^{-4}$
V_B	$5.710 \cdot 10^{-4}$
V_C	$4.888 \cdot 10^{-4}$
V_A Bøckman	$4.251 \cdot 10^{-4}$
V_B Bøckman	$6.383 \cdot 10^{-4}$
V_C Bøckman	$5.531 \cdot 10^{-4}$
$\cos \phi_A$	$1.979 \cdot 10^{-3}$
$\cos \phi_B$	$1.518 \cdot 10^{-3}$
$\cos \phi_C$	$2.322 \cdot 10^{-3}$
$\cos \phi_A$ Bøckman	$2.398 \cdot 10^{-4}$
$\cos \phi_B$ Bøckman	$4.013 \cdot 10^{-4}$
$\cos \phi_C$ Bøckman	$3.847 \cdot 10^{-4}$

where x_i are the points from the scaled high-resolution measurements and y_i are the points from the scaled circuit model calculations and n is the number of points. We see that I_1 , I_2 , I_3 , I_A , $\cos \phi_A$, $\cos \phi_B$, and $\cos \phi_C$ have errors of order 10^{-3} and the rest of the quantities have errors of order 10^{-4} .

10.4 Discussion

10.4.1 Measurements

The process data and the high-resolution measurement data are shown to be in good agreement, as seen in Fig. 10.6, when we apply appropriate scaling factors and choose the right set of Rogowski coils. Thus our chosen method of extracting phases and amplitudes from the high-resolution measurement data works well. The internal consistency between the two methods also serves as a good check to both of them. There are however still some unanswered questions regarding the measurements.

Firstly, the three sets of two Rogowski coils should give the same measurements. We were able to “solve” the issue by choosing a set of internally matching coils, but the question still remains of why they give different measurements in the first place. We also see that we need slightly different scaling factors for the Rogowski coil measurements

to perfectly fit with the two data sets. The scaling factor is believed to be a geometric factor and therefore should be constant even for measurements made weeks or months apart. As our data sets cover only a short period of time, 3.75 and 20 minutes, one possible explanation is that there are slight disagreements between the high-resolution measurement and process data, and that choosing scaling factors so that they perfectly match for one instance is a type of overfitting. However, to better understand the changes and effects of scaling factors one would need more and longer data sets to compare.

For this thesis we have simply guessed Rogowski coil scaling factors that compromise between the data sets as well as possible. Choosing scaling factors can probably be done more rigorously, by some optimization process that balances the fit of each data set. One could imagine doing such an optimization on enough data sets to arrive at some standard scaling factor we believe to be as close to the true geometric factor as possible, but that has not been done at this stage.

From the symmetrical components we find that there is a circulating current in the transformer delta. To be in agreement with our theoretical results, that must mean that either the voltage supply or the transformers themselves are unbalanced. All real systems are unbalanced, and it is plausible that the effect should be noticeable. The fact that $v_0 = 0$ for the electrode currents is as it should be, since the sum of the electrode currents entering the Y connection must be zero due to charge conservation.

We interpret the zero sequence component of the electrode voltage as deviation from the “true” neutral point as discussed in Sec. 9.2.1. If desired, one can therefore use the v_0 component to adjust the electrode voltage measurements to be taken from this changing true neutral.

- must say something about uncertainties in the measurements themselves

10.4.2 Comparison with circuit model

From our comparison of high-resolution measurement data to the circuit model, the general picture is that they fit well in both patterns and absolute value, as presented in Fig. 10.7 and Tab. 10.1. I_A has larger error than I_C , which in turn has larger error than I_B due to the choice of scaling factor. Choosing a better scaling factor for the dataset shown would have resulted in larger errors for the other dataset. We note that this affects the errors of electrode current as well, with $I_1 = I_C - I_A$ having the largest error of the three, and $I_3 = I_B - I_C$ having the smallest error. But even with the differing scaling factors, the pattern of all currents fit well.

We see the poorest pattern match for transformer voltages, both between measurements and the circuit model, but also between the direct measurement and the voltage calculated from Böckman measurements. There is a tendency for the Böckman measurement to have more variation than the direct measurement. We do not have a good explanation for the differences between the two measurement methods. The poorer fit with the circuit model might possibly have something to do with how we model the transformer, by lumping all the resistance and leakage flux on the secondary side. But as we have not tested other transformer models, we cannot conclude at this stage. In the very end of the time series, the measured transformer voltages make a large jump that the circuit model does not capture. The jump could be due to the operators changing the transformer windings ratio, but this have not been confirmed either way.

For transformer power factor, we see a good pattern match between both measurements and the circuit model, but the direct measurements are shifted to lower values. This is due to a phase shift of roughly 5° to 7° between the direct voltage

measurement and the voltage as calculated from Bøckman measurements. The fact that Bøckman measurements give the best fit in this case is not surprising, given the input to the circuit model. We use electrode impedance from process data, which are calculated based on Bøckman measurements of electrode voltage, as input. That the circuit model therefore most closely resembles calculations based on Bøckman voltage measurements in other parts of the system is no surprise.

We see in Fig. 10.1b that the electrode voltage is periodic but non-sinusoidal. This is the effect of arcing, and means that this part of the circuit is non-linear, while our circuit model works under the assumption that everything is linear. This is a source of error in our model, but as seen in the comparison the errors in r.m.s. value and power factor are still small. For the furnace we consider it therefore seems like a linear system is a good approximation, able to capture most of the systems behaviour.

The fact that the circuit model fits measurement data as well as it does, especially the trends, shows that it is mostly a good representation of the furnace and supply system. This gives more credibility to the other results we have found by use of the circuit model as well, as agreement in the case we can check makes the numerical experiments we cannot easily check more credible. There are however specific areas where the circuit model performs worse, particularly it cannot capture the non-linear behaviour of electrode voltage and is a poorer match for secondary side transformer voltage than the other measurements.

Chapter 11

Conclusion

11.1 Summary

In this thesis we have set up circuit models of the primary side representing the supply system, the secondary side representing the furnace, and a full circuit model of the entire system, the last of which is a new approach. We have implemented and verified a numerical solver for harmonic circuit problems in general and the circuits under consideration in particular. The numerical solver was then used as a tool to study the combined supply and furnace system.

We used an equivalent circuit model of a furnace system with the fairly novel setup of low-voltage compensation to study the behaviour of the circuit as a function of capacitance, and compared it to the more standard setup of high-voltage compensation. Our results agree with previous literature on LVC, showing that LVC has the advantage of improving the power factor of the transformers in addition to the grid power factor. This means that with low-voltage compensation, the transformers can deliver the same amount of active power with a lower apparent power and lower currents running in the grid connection and through the transformers. We also estimated the currents and voltages the capacitor would be subjected to, hopefully providing a better foundation for experts to evaluate the method's potential usefulness and effectiveness. We found the ratio between several HVC and LVC values as a function of winding ratios in the transformers to be polynomial functions.

When using the previously developed metamodel to simulate a furnace running with resistance control, we observed that the model has an interaction effect on the resistances, even though literature reports that there should not be one. In our example the resistance of the stationary electrode changed about 9 percent as much as the resistance of the two moving electrodes, which is a considerable amount. We suggested that the uncertain measurements of electrode voltage due to a moving neutral point might be the cause of the observed interaction. More research is however needed to conclusively find the source of and properly quantify the interaction effect.

Lastly, we compared the numerical circuit model with high-resolution measurements of a real ferromanganese furnace at operation. Our circuit model agreed well with the measurements, showing that we are able to capture both the patterns and absolute value of the system to a good degree even with this simplified model, where we have disregarded non-linear elements and higher harmonics. We conclude that for a ferromanganese furnace of this type, the nonlinearity of the arcs do not distort the system enough to pose a serious error in our model, and the model is therefore correct enough to be a useful tool. This also gives credibility to our other results. Building on the results

presented in this thesis, the circuit models and numerical solver can be used for looking at the system behaviour either in real time or as a simulation, or carry out experiments we are unable or unwilling to conduct on a real furnace in operation.

11.2 Future work

For future work it would be interesting to try to implement a non-interacting resistance controller, for instance by adjusting the Bøckman voltage measurements to the true neutral point. It would also be useful to better understand the interaction effect in itself, why it appears, how large it is, in which scenarios it is most prominent, and to what degree it is harmful by for example causing excessive electrode movement.

We could also use the model to study higher harmonics, even without introducing a non-linear element, as that would still fit within the constraints of our harmonic solver.

Another route to take would be to develop and implement more complicated circuit models. One possibility is to create a model with a non-linear element in order to take arcing into account. This would also require implementation of a non-harmonic numerical solver. However, for the ferromanganese furnace we get good results even with a simple linear model, so our model is functional as it is. Perhaps more interesting would be to use a non-harmonic solver for transient signals, that is signals that vary over time. That way we could use the model to simulate what happens during startup and shutdown of the furnace.

Given access to measurements from furnaces producing alloys other than ferromanganese, we could find out how well the simplified equivalent circuit model works for those as well. This needs to be done before using the circuit model to draw conclusions about other types of furnaces, as for example the effect of arcing will be different for different materials.

Appendix A

Circuit diagram symbols

	Resistor
	Capacitor
	Inductor
	General component with impedance
	Sinusoidal voltage source
	Ideal transformer

Appendix A. Circuit diagram symbols

Appendix B

Analytical current solutions

The current solutions for the primary side with unbalanced capacitors are presented in Eq. B.1, where we have defined $Z_{xy} = Z_{C1}Z_{C2} + Z_{C1}Z_{C3} + Z_{C2}Z_{C3}$, $Z_x = Z_{C1} + Z_{C2} + Z_{C3}$ and

$$\alpha = 27Z^4 + 18Z^3(2Z_x + Z_t) + 3Z^2(12Z_{xy} + 6Z_tZ_x + Z_t^2) + 2ZZ_t(6Z_{xy} + Z_tZ_x) + Z_t^2Z_{xy}.$$

The current solutions of the primary side with unbalanced transformers are presented in Eq. B.2, where we have defined $Z_{xy} = Z_{p1}Z_{p3} + Z_{p1}Z_{p2} + Z_{p3}Z_{p2}$, $Z_x = Z_{p1} + Z_{p3} + Z_{p2}$ and

$$\begin{aligned}\alpha = & 3Z^4Z_x + 2Z^3(Z_{xy} + 6Z_CZ_x) + Z^2(Z_{p1}Z_{p3}Z_{p2} + 6Z_CZ_{xy} + 12Z_C^2Z_x) \\ & + 2ZZ_C(Z_{p1}Z_{p3}Z_{p2} + 2Z_CZ_{xy}) + Z_{p1}Z_{p3}Z_{p2}Z_C^2.\end{aligned}$$

Appendix B. Analytical current solutions

$$\begin{aligned}
& \left[\begin{array}{c} I_1 \\ I_2 \\ I_3 \\ I_4 \\ I_5 \\ I_6 \\ I_7 \\ I_8 \\ I_9 \\ I_{10} \\ I_{11} \\ I_{12} \end{array} \right] = \frac{1}{\alpha} \left[\begin{array}{l} \left[\begin{array}{l} V_1(27Z^3 + 9Z^2(3Z_x - Z_{C1} + 2Z_t) + Z(18Z_{xy} + 6Z_t(2Z_x - Z_{C1}) + 3Z_t^2) + 3Z_tZ_{xy} + Z_t^2(Z_{C2} + Z_{C3})) - (V_2Z_{C3} + V_3Z_{C2})(3Z + Z_t)^2 \\ V_2(27Z^3 + 9Z^2(3Z_x - Z_{C2} + 2Z_t) + Z(18Z_{xy} + 6Z_t(2Z_x - Z_{C2}) + 3Z_t^2) + 3Z_tZ_{xy} + Z_t^2(Z_{C1} + Z_{C3})) - (V_1Z_{C3} + V_3Z_{C1})(3Z + Z_t)^2 \\ V_3(27Z^3 + 9Z^2(3Z_x - Z_{C3} + 2Z_t) + Z(18Z_{xy} + 6Z_t(2Z_x - Z_{C3}) + 3Z_t^2) + 3Z_tZ_{xy} + Z_t^2(Z_{C1} + Z_{C2})) - (V_1Z_{C2} + V_2Z_{C1})(3Z + Z_t)^2 \\ 3V_1(6Z^2Z_{C1} + 2Z(3Z_{xy} + Z_{C1}Z_t) + Z_tZ_{xy}) - 3Z(V_2Z_{C2} + V_3Z_{C3})(3Z + Z_t) \\ 3V_2(6Z^2Z_{C2} + 2Z(3Z_{xy} + Z_{C2}Z_t) + Z_tZ_{xy}) - 3Z(V_1Z_{C1} + V_3Z_{C3})(3Z + Z_t) \\ 3V_3(6Z^2Z_{C3} + 2Z(3Z_{xy} + Z_{C3}Z_t) + Z_tZ_{xy}) - 3Z(V_1Z_{C1} + V_2Z_{C2})(3Z + Z_t) \\ V_1(27Z^3 + 18Z^2(Z_{C2} + Z_{C3} + Z_t) + 3ZZ_t(3Z_{C2} + 3Z_{C3} + Z_t) + Z_t^2(Z_{C2} + Z_{C3})) - (V_2Z_{C3} + V_3Z_{C2})(18Z^2 + 9ZZ_t + Z_t^2) \\ V_2(27Z^3 + 18Z^2(Z_{C1} + Z_{C3} + Z_t) + 3ZZ_t(3Z_{C1} + 3Z_{C3} + Z_t) + Z_t^2(Z_{C1} + Z_{C3})) - (V_1Z_{C3} + V_3Z_{C1})(18Z^2 + 9ZZ_t + Z_t^2) \\ V_3(27Z^3 + 18Z^2(Z_{C1} + Z_{C2} + Z_t) + 3ZZ_t(3Z_{C1} + 3Z_{C2} + Z_t) + Z_t^2(Z_{C1} + Z_{C2})) - (V_1Z_{C2} + V_2Z_{C1})(18Z^2 + 9ZZ_t + Z_t^2) \\ -V_1(9Z^2Z_{C1} + Z_{xy}(6Z + Z_t) + 3ZZ_{C1}Z_t) + V_2(9Z^2Z_{C2} + Z_{xy}(6Z + Z_t) + 3ZZ_{C2}Z_t) \\ V_1(9Z^2Z_{C1} + Z_{xy}(6Z + Z_t) + 3ZZ_{C1}Z_t) - V_3(9Z^2Z_{C3} + Z_{xy}(6Z + Z_t) + 3ZZ_{C3}Z_t) \\ -V_2(9Z^2Z_{C2} + Z_{xy}(6Z + Z_t) + 3ZZ_{C2}Z_t) + V_3(9Z^2Z_{C3} + Z_{xy}(6Z + Z_t) + 3ZZ_{C3}Z_t) \end{array} \right] \\ \left[\begin{array}{l} V_1(3ZZ_x(Z^2 + 3ZZ_C + 2ZZ_C^2) + 2ZZ_{xy}(Z + 2Z_C) + Z_{p1}Z_{p3}Z_{p2}(Z + Z_C) + Z_{p1}Z_{p2}Z_{C}^2 + Z_{p3}Z_{p2}Z_C^2) - (V_2Z_{p3} + V_3Z_{p1})Z_{p2}Z_C^2 \\ V_1(3ZZ_x(Z^2 + 3ZZ_C + 2Z_C^2) + 2ZZ_{xy}(Z + 2Z_C) + Z_{p1}Z_{p3}Z_{p2}(Z + Z_C) + Z_{p1}Z_{p2}Z_{C}^2 + Z_{p3}Z_{p2}Z_C^2) - (V_1Z_{p2} + V_3Z_{p1})Z_{p3}Z_C^2 \\ V_1(3ZZ_x(Z^2 + 3ZZ_C + 2Z_C^2) + 2ZZ_{xy}(Z + 2Z_C) + Z_{p1}Z_{p3}Z_{p2}(Z + Z_C) + Z_{p1}Z_{p2}Z_{C}^2 + Z_{p3}Z_{p2}Z_C^2) - (V_1Z_{p2} + V_2Z_{p3})Z_{p1}Z_C^2 \\ V_1(3ZZ_CZ_x(Z + 2Z_C) + ZZ_{p1}Z_{p2}Z_C + ZZ_{p3}Z_{p2}Z_C + Z_{p1}Z_{p2}Z_{C}^2 + Z_{p3}Z_{p2}Z_C^2) - (V_2Z_{p3} + V_3Z_{p1})Z_{p2}Z_C(Z + Z_C) \\ V_2(3ZZ_CZ_x(Z + 2Z_C) + ZZ_{p1}Z_{p3}Z_C + ZZ_{p1}Z_{p3}Z_{p2}Z_C + Z_{p1}Z_{p3}Z_{p2}Z_C + Z_{p3}Z_{p2}Z_{C}^2) - (V_1Z_{p2} + V_3Z_{p1})Z_{p3}Z_C(Z + Z_C) \\ V_3(3ZZ_CZ_x(Z + 2Z_C) + ZZ_{p1}Z_{p3}Z_C + ZZ_{p1}Z_{p3}Z_{p2}Z_C + Z_{p1}Z_{p3}Z_{p2}Z_C + Z_{p1}Z_{p2}Z_{C}^2) - (V_1Z_{p2} + V_2Z_{p3})Z_{p1}Z_C(Z + Z_C) \\ V_1(3Z^2Z_x(Z + 2Z_C) + 2Z^2Z_{xy} + ZZ_{p1}Z_{p3}Z_{p2} + Z_{p1}Z_{p3}Z_{p2}Z_C + 2ZZ_C(Z_{p1}Z_{p3} + Z_{xy})) - (V_2Z_{p1} + V_3Z_{p3})ZZ_{p2}Z_C \\ V_2(3Z^2Z_x(Z + 2Z_C) + 2Z^2Z_{xy} + ZZ_{p1}Z_{p3}Z_{p2} + Z_{p1}Z_{p3}Z_{p2}Z_C + 2ZZ_C(Z_{p1}Z_{p2} + Z_{xy})) - (V_1Z_{p1} + V_3Z_{p2})ZZ_{p3}Z_C \\ V_3(3Z^2Z_x(Z + 2Z_C) + 2Z^2Z_{xy} + ZZ_{p1}Z_{p3}Z_{p2} + Z_{p1}Z_{p3}Z_{p2}Z_C + 2ZZ_C(Z_{p3}Z_{p2} + Z_{xy})) - (V_1Z_{p3} + V_2Z_{p2})ZZ_{p1}Z_C \\ -V_1Z_C(3Z^2Z_{p3} + ZZ_{p3}Z_{p2} + 6ZZ_{p3}Z_C + Z_{p3}Z_{p2}Z_C) + V_2Z_C(3Z^2Z_{p2} + ZZ_{p3}Z_{p2} + 6ZZ_{p2}Z_C) \\ V_1Z_C(3Z^2Z_{p1} + ZZ_{p1}Z_{p2} + 6ZZ_{p1}Z_C + Z_{p1}Z_{p2}Z_C) - V_3Z_C(3Z^2Z_{p2} + ZZ_{p1}Z_{p2} + 6ZZ_{p3}Z_C) \\ -V_2Z_C(3Z^2Z_{p1} + ZZ_{p1}Z_{p3} + 6ZZ_{p1}Z_C + Z_{p1}Z_{p3}Z_C) + V_3Z_C(3Z^2Z_{p3} + ZZ_{p1}Z_{p3} + 6ZZ_{p3}Z_C) \end{array} \right] \end{array} \right] \quad (B.1) \\
& \left[\begin{array}{c} I_1 \\ I_2 \\ I_3 \\ I_4 \\ I_5 \\ I_6 \\ I_7 \\ I_8 \\ I_9 \\ I_{10} \\ I_{11} \\ I_{12} \end{array} \right] = \frac{1}{\alpha} \left[\begin{array}{l} \left[\begin{array}{l} V_1(3ZZ_x(Z^2 + 3ZZ_C + 2ZZ_C^2) + 2ZZ_{xy}(Z + 2Z_C) + Z_{p1}Z_{p3}Z_{p2}(Z + Z_C) + Z_{p1}Z_{p2}Z_{C}^2 + Z_{p3}Z_{p2}Z_C^2) - (V_2Z_{p3} + V_3Z_{p1})Z_{p2}Z_C^2 \\ V_1(3ZZ_x(Z^2 + 3ZZ_C + 2Z_C^2) + 2ZZ_{xy}(Z + 2Z_C) + Z_{p1}Z_{p3}Z_{p2}(Z + Z_C) + Z_{p1}Z_{p2}Z_{C}^2 + Z_{p3}Z_{p2}Z_C^2) - (V_1Z_{p2} + V_3Z_{p1})Z_{p3}Z_C^2 \\ V_1(3ZZ_x(Z^2 + 3ZZ_C + 2Z_C^2) + 2ZZ_{xy}(Z + 2Z_C) + Z_{p1}Z_{p3}Z_{p2}(Z + Z_C) + Z_{p1}Z_{p2}Z_{C}^2 + Z_{p3}Z_{p2}Z_C^2) - (V_1Z_{p2} + V_2Z_{p3})Z_{p1}Z_C^2 \\ V_1(3ZZ_CZ_x(Z + 2Z_C) + ZZ_{p1}Z_{p2}Z_C + ZZ_{p3}Z_{p2}Z_C + Z_{p1}Z_{p2}Z_{C}^2 + Z_{p3}Z_{p2}Z_C^2) - (V_2Z_{p3} + V_3Z_{p1})Z_{p2}Z_C(Z + Z_C) \\ V_2(3ZZ_CZ_x(Z + 2Z_C) + ZZ_{p1}Z_{p3}Z_C + ZZ_{p1}Z_{p3}Z_{p2}Z_C + Z_{p1}Z_{p3}Z_{p2}Z_C + Z_{p3}Z_{p2}Z_{C}^2) - (V_1Z_{p2} + V_3Z_{p1})Z_{p3}Z_C(Z + Z_C) \\ V_3(3ZZ_CZ_x(Z + 2Z_C) + ZZ_{p1}Z_{p3}Z_C + ZZ_{p1}Z_{p3}Z_{p2}Z_C + Z_{p1}Z_{p3}Z_{p2}Z_C + Z_{p1}Z_{p2}Z_{C}^2) - (V_1Z_{p2} + V_2Z_{p3})Z_{p1}Z_C(Z + Z_C) \\ V_1(3Z^2Z_x(Z + 2Z_C) + 2Z^2Z_{xy} + ZZ_{p1}Z_{p3}Z_{p2} + Z_{p1}Z_{p3}Z_{p2}Z_C + 2ZZ_C(Z_{p1}Z_{p3} + Z_{xy})) - (V_2Z_{p1} + V_3Z_{p3})ZZ_{p2}Z_C \\ V_2(3Z^2Z_x(Z + 2Z_C) + 2Z^2Z_{xy} + ZZ_{p1}Z_{p3}Z_{p2} + Z_{p1}Z_{p3}Z_{p2}Z_C + 2ZZ_C(Z_{p1}Z_{p2} + Z_{xy})) - (V_1Z_{p1} + V_3Z_{p2})ZZ_{p3}Z_C \\ V_3(3Z^2Z_x(Z + 2Z_C) + 2Z^2Z_{xy} + ZZ_{p1}Z_{p3}Z_{p2} + Z_{p1}Z_{p3}Z_{p2}Z_C + 2ZZ_C(Z_{p3}Z_{p2} + Z_{xy})) - (V_1Z_{p3} + V_2Z_{p2})ZZ_{p1}Z_C \\ -V_1Z_C(3Z^2Z_{p3} + ZZ_{p3}Z_{p2} + 6ZZ_{p3}Z_C + Z_{p3}Z_{p2}Z_C) + V_2Z_C(3Z^2Z_{p2} + ZZ_{p3}Z_{p2} + 6ZZ_{p2}Z_C) \\ V_1Z_C(3Z^2Z_{p1} + ZZ_{p1}Z_{p2} + 6ZZ_{p1}Z_C + Z_{p1}Z_{p2}Z_C) - V_3Z_C(3Z^2Z_{p2} + ZZ_{p1}Z_{p2} + 6ZZ_{p3}Z_C) \\ -V_2Z_C(3Z^2Z_{p1} + ZZ_{p1}Z_{p3} + 6ZZ_{p1}Z_C + Z_{p1}Z_{p3}Z_C) + V_3Z_C(3Z^2Z_{p3} + ZZ_{p1}Z_{p3} + 6ZZ_{p3}Z_C) \end{array} \right] \end{array} \right] \quad (B.2)
\end{aligned}$$

Appendix C

Fast Fourier transform

Appendix C. Fast Fourier transform

Bibliography

- [1] B. Asphaug, ‘The FeMn process,’ Elkem, Kristiansand, 10th Apr. 1992, Internal Elkem report courtesy of Elkem ASA and Eramet S.A.
- [2] A. M. Valderhaug, ‘Modelling and control of submerged-arc ferrosilicon furnaces,’ Accepted: 2014-12-19T14:06:29Z, Ph.D. dissertation, Norwegian University of Science and Technology, 1992. [Online]. Available: <http://hdl.handle.net/11250/260770>.
- [3] M. I. Gasik, Ed., *Handbook of ferroalloys: Theory and technology*, Amsterdam: Butterworth-Heinemann, 2013, ISBN: 978-0-08-097753-9.
- [4] P. Hannesson, *The Si process. Drawings*. Elkem Iceland, May 2016. [Online]. Available: <https://www.elkem.com/globalassets/iceland/si-process.pdf>.
- [5] A. De Waal, I. J. Barker, M. S. Rennie, J. Klopper and B. S. Groeneveld, ‘Electrical factors affecting the economic optimization of submerged-arc furnaces,’ in *Infacon VI: International Ferro-Alloy Congress*, Cape Town, South Africa: South African Institute of Mining and Metallurgy, Jun. 1995, pp. 247–252. [Online]. Available: <https://www.pyrometallurgy.co.za/InfaconVI/>.
- [6] A. B. Stewart, ‘An analysis of the electrical circuit of submerged-arc furnaces,’ tex.ids= Stewart1980, Ph.D. dissertation, University of Cape Town, 1980. [Online]. Available: <http://hdl.handle.net/11427/14048>.
- [7] R. Innvær, K. Fidje and T. Sira, ‘3-dimensional calculations on smelting electrodes,’ vol. 8, no. 2, pp. 103–115, 4th Jan. 1987. DOI: 10.4173/mic.1987.2.3. [Online]. Available: <https://www.mic-journal.no/ABS/MIC-1987-1987-2.asp> (visited on 27/03/2025).
- [8] A. Bermúdez, J. Bullón and F. Pena, ‘A finite element method for the thermoelectrical modelling of electrodes,’ *Communications in Numerical Methods in Engineering*, vol. 14, no. 6, pp. 581–593, 1998, _eprint: <https://onlinelibrary.wiley.com/doi/pdf/10.1002/%28SICI%291099-0887%28199806%2914%3A6%3C581CNM175%3E3.0.CO%3B2-S>, ISSN: 1099-0887. DOI: 10 . 1002 / (SICI) 1099 - 0887(199806)14:6<581 ::AID-CNM175>3.0.CO;2-S. [Online]. Available: <https://onlinelibrary.wiley.com/doi/abs/10.1002/%28SICI%291099-0887%28199806%2914 %3A6 %3C581 %3A %3AAID - CNM175 %3E3 . 0 . CO %3B2 - S> (visited on 27/03/2025).
- [9] I. M. Dougall, C. F. R. Smith, B. Olmstead and W. A. Gericke, ‘A FINITE ELEMENT MODEL OF a SØDERBERG ELECTRODE WITH AN APPLICATION IN CASING DESIGN,’ *Infacon X*, 2004.
- [10] H. T. Ingason, ‘A three dimensional simulation model for a soderberg electrode,’ *Infacon VIII*, 1998.

Bibliography

- [11] K. Fidje, R. Innvær and R. Ugland, ‘EFFECT OF CURRENT VARIATIONS ON MATERIAL PROPERTIES AND THERMAL STRESSES IN s0derberg ELECTRODES,’ *Infacon IV, Proceedings of the Fourth International Ferroalloys Congress*, 1986.
- [12] S. A. Halvorsen, H. A. H. Olsen and M. Fromreide, ‘An efficient simulation method for current and power distribution in 3-phase electrical smelting furnaces,’ *IFAC-PapersOnLine*, 17th IFAC Symposium on Control, Optimization and Automation in Mining, Mineral and Metal Processing MMM 2016, vol. 49, no. 20, pp. 167–172, 1st Jan. 2016, ISSN: 2405-8963. DOI: 10.1016/j.ifacol.2016.10.115. [Online]. Available: <https://www.sciencedirect.com/science/article/pii/S2405896316316780> (visited on 27/03/2025).
- [13] M. Dhainaut, ‘SIMULATION OF THE ELECTRIC FIELD IN a SUBMERGED ARC FURNACE,’ 2003. [Online]. Available: <https://www.semanticscholar.org/paper/SIMULATION - OF - THE - ELECTRIC - FIELD - IN - A - SUBMERGED - ARC - Dhainaut/a981c2ac13596cdcca045383e49297c7c7f6a5ec> (visited on 27/03/2025).
- [14] Y. A. Tesfahunegn, T. Magnusson, M. Tangstad and G. Saevarsdottir, ‘Dynamic current distribution in the electrodes of submerged arc furnace using scalar and vector potentials,’ in *Computational Science – ICCS 2018*, Y. Shi, H. Fu, Y. Tian *et al.*, Cham: Springer International Publishing, 2018, pp. 518–527, ISBN: 978-3-319-93701-4. DOI: 10.1007/978-3-319-93701-4_40.
- [15] A. Bermúdez, ‘Finite element methods for 3 d eddy current problems in bounded domains subject to realistic boundary conditions . an application to metallurgical electrodes.’ [Online]. Available: <https://www.semanticscholar.org/paper/Finite - element - methods - for - 3 - D - eddy - current - in - to - . - Berm % C3 % BAdez / 32f5a4b7f41286c296306e7e3984da3bbd70929b> (visited on 27/03/2025).
- [16] I. Mc Dougall, ‘Finite element modelling of electric currents in AC submerged arc furnaces,’ 1st Jan. 2007.
- [17] B. Larsen and H. Feldborg, ‘MINIMIZING THERMAL STRESS DURING SHUTDOWN OFS0derbergelectrodes,’ *Infacon XIII*, 2013.
- [18] L. Gunnewiek, L. Oshinowo, T. Plikas and R. Haywood, ‘THE APPLICATION OF NUMERICAL MODELLING TO THE DESIGN OF ELECTRIC FURNACES,’ 1st Jan. 2004.
- [19] I. J. Barker, ‘An electrode controller for submerged arc furnaces,’ *IFAC Proceedings Volumes*, vol. 13, no. 7, pp. 611–621, 1st Jan. 1980, ISSN: 1474-6670. DOI: 10.1016/s1474-6670(17)64768-2. (visited on 15/03/2022).
- [20] M. A. Reuter, M. Oosthuizen, I. J. Barker, M. S. Rennie and A. de Waal, ‘The dynamic response of submerged-arc furnaces to electrode movement,’ *IFAC Proceedings Volumes*, vol. 28, no. 17, pp. 121–127, 1st Aug. 1995, ISSN: 1474-6670. DOI: 10.1016/s1474-6670(17)46753-x. (visited on 02/03/2022).
- [21] N. Storey, *Electronics: A Systems Approach*, 6th Edition. Harlow: Pearson, 2017, ISBN: 978-1-292-11406-4 978-1-292-11411-8.
- [22] W. G. Hurley and W. H. Wölfle, *Transformers and inductors for power electronics: Theory, design and applications*. Chichester: Wiley, 2014, 348 pp., ISBN: 978-1-119-95057-8.
- [23] A. R. Daniels, *Introduction to electrical machines*, Reprinted. London: Macmillan, 1979, 187 pp., ISBN: 978-0-333-19627-4 978-0-333-19626-7.

- [24] A. v. Meier, *Electric power systems: a conceptual introduction* (Wiley survival guides in engineering and science). Hoboken, N.J: IEEE Press : Wiley-Interscience, 2006, 309 pp., OCLC: ocm62616191, ISBN: 978-0-471-17859-0.
- [25] P. M. Anderson, ‘Symmetrical components,’ in *Analysis of Faulted Power Systems*, Wiley-IEEE Press, 1995, pp. 19–35, ISBN: 978-0-470-54412-9. [Online]. Available: <http://ieeexplore.ieee.org/document/5265524> (visited on 12/03/2025).
- [26] *Electromagnetic compatibility (EMC) - part 2-2: Environment - compatibility levels for low-frequency conducted disturbances and signalling in public low-voltage power supply systems*, version 2.0, 28th Mar. 2002. [Online]. Available: <https://webstore.iec.ch/en/publication/4133> (visited on 12/03/2025).
- [27] J. Meintjes, ‘A comparison of power-factor correction on submerged-arc furnaces by capacitors in shunt and series,’ in *Infacon I: International Ferro-Alloy Congress*, Johannesburg, South Africa: South African Institute of Mining and Metallurgy, Apr. 1974, pp. 149–155. [Online]. Available: <https://www.pyrometallurgy.co.za/Infacon/>.
- [28] A. Bermúdez, D. Gómez and P. Salgado, *Mathematical Models and Numerical Simulation in Electromagnetism* (UNITEXT). Cham: Springer International Publishing, 2014, vol. 74, ISBN: 978-3-319-02948-1 978-3-319-02949-8. DOI: 10.1007/978-3-319-02949-8. [Online]. Available: <http://link.springer.com/10.1007/978-3-319-02949-8> (visited on 25/10/2024).
- [29] S. K. Yadav, *Discrete Mathematics with Graph Theory*. Cham: Springer International Publishing, 2023, ISBN: 978-3-031-21320-5 978-3-031-21321-2. DOI: 10.1007/978-3-031-21321-2. [Online]. Available: <https://link.springer.com/10.1007/978-3-031-21321-2> (visited on 26/10/2024).
- [30] I. J. Barker and A. B. Stewart, ‘Inductive reactance, and the operation of large submerged-arc furnaces,’ *Journal of The South African Institute of Mining and Metallurgy*, vol. 80, no. 3, pp. 123–128, 1980, ISSN: 0038-223X. [Online]. Available: <http://www.saimm.org.za/Journal/v080n03p123.pdf>.
- [31] Z. Li, S. Chu, X. Tao, T. Li, J. Zhang and X. Bao, ‘Compensation of submerged arc furnace by capacitors connected in shunt on low voltage side,’ in *Proceedings of the 15th International Ferro-Alloys Congress (INFACON XV)*, Cape Town, South Africa, 2018.
- [32] G. A. Sævars Þóttir, P. Manolescu, P. Magnússon and K. Sigurjonsson, ‘Circulating currents in the delta connection, feasibility of skew tapping in the operation of submerged-arc furnaces,’ in *Proceedings of the 13th International Ferro-Alloys Congress (INFACON XIII)*, Almaty, Kazakhstan, Jun. 2013, pp. 443–452.
- [33] M. Sparta, D. Varagnolo, K. Stråbø, S. A. Halvorsen, E. V. Herland and H. Martens, ‘Metamodeling of the electrical conditions in submerged arc furnaces,’ *Metallurgical and Materials Transactions B*, vol. 52, no. 3, pp. 1267–1278, 1st Jun. 2021, ISSN: 1543-1916. DOI: 10.1007/s11663-021-02089-7. [Online]. Available: <https://doi.org/10.1007/s11663-021-02089-7> (visited on 21/10/2024).
- [34] ‘SAFECI.’ (), [Online]. Available: <https://safeci.web.norce.cloud/> (visited on 10/03/2025).

Bibliography

- [35] M. Sparta, M. Fromreide, V. K. Risinggård and S. A. Halvorsen, *Electrical conditions in submerged arc furnaces: A web-based simulator*, Rochester, NY, 3rd Apr. 2022. DOI: 10.2139/ssrn.4118651. [Online]. Available: <https://papers.ssrn.com/abstract=4118651> (visited on 10/03/2025).
- [36] I. J. Barker, A. De Waal, M. S. Rennie and J. Klopper, ‘The interaction effect in submerged-arc furnaces,’ in *Proceedings of the 49th Electric Furnace Conference*, vol. 49, Toronto, Canada: Iron & Steel Society, 1991, pp. 305–310.
- [37] M. Sparta, V. K. Risinggård and U. Thisted, ‘Bøckman method for measuring furnace core voltages: A modeling review,’ in *Proceedings of the Silicon for the Chemical and Solar Industry XVII*, Trondheim, Norway: SSRN Journals, 3rd Sep. 2024, ISBN: 978-82-692919-3-3. DOI: 10.2139/ssrn.4942623. [Online]. Available: <https://www.ssrn.com/abstract=4942623>.
- [38] M. H. Samimi, A. Mahari, M. A. Farahnakian and H. Mohseni, ‘The rogowski coil principles and applications: A review,’ *IEEE Sensors Journal*, vol. 15, no. 2, pp. 651–658, Feb. 2015, Conference Name: IEEE Sensors Journal, ISSN: 1558-1748. DOI: 10.1109/JSEN.2014.2362940. [Online]. Available: <https://ieeexplore.ieee.org/document/6922615/?arnumber=6922615> (visited on 12/03/2025).
- [39] L. alfredo, *English: Schematic drawing of a rogowski coil used as an AC current sensor, and connected to an integrator circuit to obtain an output voltage proportional to the instantaneous value of the current i(t)*, 28th Feb. 2011. [Online]. Available: https://commons.wikimedia.org/w/index.php?title=File:Rogowski_coil.png&oldid=554386218 (visited on 24/03/2025).
- [40] O. C. Bøckman, ‘Anordning for måling av kraterspenningene i en trefase smelteovn med elektrodene i trekant,’ pat. NO126288B, 15th Jan. 1973. [Online]. Available: <https://patents.google.com/patent/NO126288B/en> (visited on 05/12/2023).
- [41] O. Bøckman, ‘Arrangement for measuring the crater voltages in a three-phase electric furnace with electrodes arranged in a delta,’ U.S. Patent 3757021A, 4th Sep. 1973. [Online]. Available: <https://patents.google.com/patent/US3757021A/en> (visited on 05/12/2023).
- [42] A. Meurer, C. P. Smith, M. Paprocki *et al.*, ‘SymPy: Symbolic computing in python,’ *PeerJ Computer Science*, vol. 3, e103, 2nd Jan. 2017, Publisher: PeerJ Inc., ISSN: 2376-5992. DOI: 10.7717/peerj-cs.103. [Online]. Available: <https://peerj.com/articles/cs-103> (visited on 08/04/2025).
- [43] C. R. Harris, K. J. Millman, S. J. van der Walt *et al.*, ‘Array programming with NumPy,’ *Nature*, vol. 585, no. 7825, pp. 357–362, Sep. 2020, Publisher: Nature Publishing Group, ISSN: 1476-4687. DOI: 10.1038/s41586-020-2649-2. [Online]. Available: <https://www.nature.com/articles/s41586-020-2649-2> (visited on 16/04/2025).
- [44] J. D. Hunter, ‘Matplotlib: A 2d graphics environment,’ *Computing in Science & Engineering*, vol. 9, no. 3, pp. 90–95, May 2007, ISSN: 1558-366X. DOI: 10.1109/MCSE.2007.55. [Online]. Available: <https://ieeexplore.ieee.org/document/4160265> (visited on 16/04/2025).
- [45] M. L. Waskom, ‘Seaborn: Statistical data visualization,’ *Journal of Open Source Software*, vol. 6, no. 60, p. 3021, 6th Apr. 2021, ISSN: 2475-9066. DOI: 10.21105/joss.03021. [Online]. Available: <https://joss.theoj.org/papers/10.21105/joss.03021> (visited on 16/04/2025).

- [46] T. p. d. team, *Pandas-dev/pandas: Pandas*, version v2.1.4, 8th Dec. 2023. DOI: 10.5281/zenodo.10304236. [Online]. Available: <https://zenodo.org/records/10304236> (visited on 16/04/2025).
- [47] W. McKinney, ‘Data structures for statistical computing in python,’ presented at the Python in Science Conference, Austin, Texas, 2010, pp. 56–61. DOI: 10.25080/Majora-92bf1922-00a. [Online]. Available: <https://doi.curvenote.com/10.25080/Majora-92bf1922-00a> (visited on 16/04/2025).
- [48] P. Virtanen, R. Gommers, T. E. Oliphant *et al.*, ‘SciPy 1.0: Fundamental algorithms for scientific computing in python,’ *Nature Methods*, vol. 17, no. 3, pp. 261–272, Mar. 2020, Publisher: Nature Publishing Group, ISSN: 1548-7105. DOI: 10.1038/s41592-019-0686-2. [Online]. Available: <https://www.nature.com/articles/s41592-019-0686-2> (visited on 16/04/2025).